

# **Graphene-Diamond Heterostructures**



**Fang Zhao**

This thesis is submitted for the degree Doctor of Philosophy.  
Department of Electronic and Electrical Engineering  
University College London  
November 2014

**Declaration**

The work in this thesis is the result of research carried out at University College London, London Centre for Nanotechnology, Diamond Electronics Group. I declare it to be my own work unless referenced to the contrary in the text.

Copyright © 2014 by Fang Zhao

“The copyright of this thesis rests with the author. No quotations from it should be published without the author’s prior written consent and information derived from it should be acknowledged”.

# **Acknowledgements**

First and foremost I want to thank my advisor Professor Richard Jackman. It has been an honor to be his PhD student. I appreciate all his contributions of time and ideas to make my PhD experience productive and stimulating. The joy and enthusiasm he has for life and work were contagious me.

The members of the Diamond group have contributed immensely to my personal and research time at UCL. I am especially grateful for the fun and friendly group of original Diamond group members when I started my PhD: Aysha Chaudhary, Niall Tumilty, Mose Bevilacqua, Joseph Welch, Ana Carolina Parada, and Robert Edgington. I am very appreciated their enthusiasm, patience, willingness to help me learn all the instruments and give good advice and collaboration. I also want to thank you for the current Diamond group members for enjoyable moments: Mohammad Golsharifi, Alice Taylor, Suguru Amakubo, Alex Pakpour-Tabrizi, Thuong Thuong Nguyen, Adbulkareem Afandi, and Ralph Moors.

In regards to the AFM and UV-Vis work, I thank Stephen Hudziak's help. I also feel grateful for help from Suguo Huo for FET fabrication. I would like to acknowledge Qi Jiang who worked with me for graphene-nanodiamond paper to give helpful suggestion. I am also grateful for Professor Zhengxiao Guo and Xiaoyu Han for the simulation work and discussion for graphene-singly crystal diamond works. In regards to the low temperature measurement for graphene-single crystal diamond samples, I thank Dr. Ling Hao's group from National Physical Laboratory.

My time at UCL was made enjoyable in large part due to many friends and group members that became an important part of my life.

Lastly, I would like to thank my family for all their love, supporting and encouragement. Words cannot express how grateful I am. My parents raised me with a love and supported me in all my pursuits. I cannot finish my PhD with their supporting and love. And I fell so appreciated for my loving, supportive, encouraging, and patient husband Andrei Vrajitoarea whose support during the final stages of my PhD. Thank you for all the people for everything,

Fang Zhao

UCL

November 2014

# **Abstract**

Graphene obtained by mechanical exfoliation of graphite displays unique electronic properties with high mobility and saturation velocity. However, this is not a scalable technique, the film being limited to small area. Large area synthesis of good quality graphene has been achieved by CVD. The choice of substrate apparently influences the electronic properties of graphene. Most of reports have used SiO<sub>2</sub>-Si due to the widespread availability, but it is a poor choice of the material to degrade the graphene performance. In this thesis, more ideal platforms are introduced, including single crystal diamond (SCD), nanodiamond (ND), and diamond-like-carbon (DLC). It was found that different terminations for substrates caused strong effects for graphene properties. For H-terminated diamond, it was found that a p-type layer with good mobility and a small band gap, whilst when N/F-terminations are introduced it was found that a layer with more metallic-like characters arises. Furthermore, different orientations of H-terminated SCD(100)/(111) were found to induce different band-gap of graphene. Simulation analysis proves the difference. However, the mobility results of graphene-H-terminated ND heterostructure are better than graphene supported by SCD, which offers the prospect of low cost sp<sup>2</sup> on sp<sup>3</sup> technology. Raman and XPS results reveal the influence from the C-H band of ND surface. Impedance measurements show two conductive paths in the graphene-HND heterostructure. Graphene FET was built on this heterostructure, which exhibited n-type and high mobility. The family of amorphous carbon films, DLC, appeal to a preferable choice of graphene supporting substrate since IBM built the high-frequency graphene FET on DLC. For N-termination it was found that the optical band gap of DLC shrunk, whilst for F-terminated DLC it was found that fluorine groups reduce the DLC's surface energy. Owing to different phonon

energies and surface trap densities, graphene-DLC heterostructures give different electronic properties and offer the prospect for 2D lateral control applications.

# Table of Contents

## Contents

Acknowledgements.....	2
Abstract.....	4
Chapter 1.....	8
Introduction.....	8
Reference.....	10
Chapter 2.....	11
Background.....	11
2.1 Carbon.....	11
2.2 Graphene.....	12
2.2.1 Graphene crystal structure.....	12
2.2.2 Graphene band structure.....	14
2.2.3 Graphene properties and applications.....	18
2.3 Diamond.....	21
2.3.1 Microwave-plasma CVD growth of diamond.....	22
2.3.2 Properties and Application of diamond.....	24
2.3.3 Nanodiamond particles: synthesis and applications.....	25
2.4 Diamond-like carbon (DLC).....	27
2.4.1 Growth of DLC.....	28
2.4.2 Properties and applications of DLC.....	29
Reference.....	35
Chapter 3.....	38
Experimental Methods.....	38
3.1 Introduction.....	38
3.2 Atomic force microscopy (AFM).....	38
3.3 Raman spectroscopy.....	40
3.3.1 Raman scattering.....	40
3.3.2 Raman spectra for graphene.....	41
3.4 X-ray photoelectron spectroscopy.....	43
3.5 Impedance spectroscopy.....	44
3.6 Hall effect measurement.....	45
3.6.1 Hall effect.....	45
3.6.2 Van der Pauw technique.....	46
3.7 Ultraviolet-visible spectroscopy.....	47
3.8 Reactive-ion etcher (RIE).....	48
3.9 Focused ion beam.....	50
3.10 Device processing.....	51
3.10.1 Overview.....	51
3.10.2 Preparation of diamond samples.....	51
3.10.3 CVD graphene.....	54
Reference.....	56
Chapter 4.....	58
Electronic Properties of Graphene-Single Crystal Diamond Heterostructures.....	58
4.1 Introduction.....	58

4.2 Experimental methods.....	58
4.3 Results .....	59
4.4 Discussion .....	63
4.5 Concluding remarks.....	67
Reference.....	68
Chapter 5.....	69
Properties of graphene-diamond-like carbon Heterostructures .....	69
5.1 Introduction .....	69
5.2 Experimental methods.....	70
5.3 Results and Discussion.....	71
5.4 Conclusions.....	77
Reference.....	78
Chapter 6.....	80
Graphene-Nanodiamond Heterostructure and their applicant of Field Effect transistors	
.....	80
6.1. Introduction .....	80
6.2. Experimental Section.....	81
6.3. Results and Discussion.....	83
6.3.1 Characterisation of Graphene-H-ND heterostructures .....	83
6.2.2 Electronic transport in graphene-nanodiamond heterostructures .....	89
6.3.3 Graphene Field Effect Transistor on Hydrogen terminated nanodiamond	
.....	95
6.4. Conclusion.....	97
References.....	99
Chapter 7.....	102
Graphene-Single Crystal Diamond (100)/(111) Hybrid Structure .....	102
7.1 Introduction .....	102
7.2 Experiment section.....	102
7.3 Results and Discussion.....	104
7.4 Conclusion.....	112
Reference.....	113
Chapter 8.....	115
Conclusion .....	115
Reference.....	118
List of Figures and Tables.....	119
Appendix: List of Abbreviations.....	123

# Chapter 1

## Introduction

Graphene is attracting huge worldwide interest in its potential as an electronic material, since two-dimensional carrier transport with extremely high mobility values can be observed<sup>1</sup>. As a monolayer of  $sp^2$  carbon, most applications of graphene will only be realised by supporting this material on a non-graphene substrate. Chemical vapour deposition (CVD) of graphene on metal foils, most commonly copper<sup>2,3</sup>, enables large area graphene monolayers to be produced, which can then be detached from the Cu, and deposited onto a suitable insulator through a polymer-mediated transfer process<sup>4</sup>. Once monolayer graphene is supported on such a substrate, substrate-induced structural distortion<sup>5</sup>, the presence of adsorbates<sup>6</sup>, local charge disorder<sup>7</sup>, atomic structure at the edges<sup>8</sup> and atomic scale defects and impurities<sup>9</sup> strongly influence the transport properties of the graphene. The majority of reports concerning the electronic properties of CVD graphene that has been transferred in this manner concern the use of  $SiO_2$ -Si, due to the widespread availability of this material system. However, graphene devices fabricated on  $SiO_2$  have been found to suffer from additional scattering associated with the low surface phonon energy and large trap density in  $SiO_2$ , resulting in deterioration of the electronic properties of the graphene<sup>10</sup>. Both of these problems could be addressed by replacing the  $SiO_2$  with diamond to produce an all-carbon heterostructure system. Moreover, the high thermal conductivity of diamond could avoid the problems associated with Joule heating and subsequent saturation velocity saturation in the graphene associated with  $SiO_2$ <sup>11,12</sup>.

Wu and co-workers produced field-effect transistors (FETs) by transferring CVD grown graphene onto diamond-like carbon (DLC) coated Si substrates<sup>13</sup>. Extremely high frequency

device operation was achieved, indicating good substrate-limited mobilities. DLC is an amorphous mixture of  $sp^2$  and  $sp^3$  clusters, with some hydrogen content. Yu *et al*<sup>14</sup> used a fine grain crystalline diamond material, known as ultra-nanocrystalline diamond (UNCD) to fabricate graphene-UNCD FETs. The UNCD allowed for considerably higher current carrying capacity than similarly fabricated graphene-SiO<sub>2</sub> structures. This positive result was attributed to the improved thermal properties of the UNCD-containing heterostructures. Indeed, similar devices fabricated from graphene-single crystal diamond (SCD) layers performed better but is limited by high cost of SCD. This thesis investigates the use of diamond and DLC with different terminations to support graphene.

Chapter 2 reports the background theory of carbon, graphene and diamond. The experimental methods and techniques used in this thesis are explained in chapter 3. The aims of the projects are to investigate how graphene properties are affected by different supporting substrate and to show another carbon material “Diamond” improves graphene mobility and opens a bandgap. Chapter 4 presents an investigation into the electronic properties of graphene influenced by different terminated SCD (H-, O-, N-, F-). In Chapter 5, CVD graphene was transferred to different terminated DLC. It was found that different terminated DLC change electronic properties: nitrogen terminations enable to lead to optical band gap shrink; fluorine bonding groups have been presented to reduce DLC’s surface energy and friction coefficients, which affect graphene’s properties. Chapter 6 presents an investigation into cheap nanodiamond to support graphene. It was found that graphene on H-terminated nanodiamond has improved the mobility by 60% compared with traditional SiO<sub>2</sub> substrate and even has comparable results with single crystal diamond (SCD) at room temperature. A top-gate FET was fabricated on graphene-ND heterostructure. Chapter 7 investigates a small

band gap of graphene opened on different orientation SCD with experimental and simulative analysis.

## Reference

1. K. S. Novoselov, A. K. Geim, S. V. Morozov, D. Jiang, M. I. Katsnelson, I. V. Grigorieva, S. V. Dubonos and A. A. Firsov, *Nature*, 438 (2005), 197
2. X. Li, W. Cai, J. An, S. Kim, J. Nah, D. Yang, R. Piner, A. Valemakanni, I. Jung, E. Tutuc, S. K. Banerjee, L. Colombo and R. S. Ruoff, *Science*, 324 (2009), 1312
3. M. Losurdo, M. M. Giangregorio, P. Capezzuto and G. Bruno, *Phys. Chem. Chem. Phys.*, 13 (2011), 20836
4. S. Kumar, N. McEvoy, H. Y. Kim, K. Lee, N. Peltekis, E. Rezvani, H. Nolan, A. Weidlich, R. Daly and G. S. Duesberg, *Phys. Status Solidi B* 248 (2011), 2604
5. S. V. Morozov, K. S. Novoselov, M. I. Katsnelson, F. Schedin, L. A. Ponomarenko, D. Jiang and A. K. Geim, *Phys. Rev. Letts.*, 97 (2006), 016801
6. Y. Yang, K. Brenner, R. Murali, *Carbon*, 50 (2012) 1727
7. Y. Zhang, V. W. Brar, C. Girit, A. Zettl and M. F. Crommie, *Nat. Phys.*, 5 (2009), 722
8. Y. Niimi, T. Matsui, H. Kambara, K. Tagami, M. Tsukada and H. Fukuyama, *Phys. Rev. B* 73 (2006), 085421
9. T. O. Wehling, A. V. Balatsky, M. I. Katsnelson, A. I. Lichtenstein, K. Scharnberg, and R. Wiesendanger, *Phys. Rev. B* 75 (2007), 125425
10. M. Ishigami, J. H. Chen, W. G. Cullen, M. S. Fuhrer and E. D. Williams, *Nano Letts.*, 7 (2007), 1643
11. X. Li, B. D. Kong, J. M. Zavada, and K. W. Kim, *Appl. Phys. Letts.*, 99 (2011), 233114
12. G.C. Loh, E.H.T. Teo, B.K. Tay, *Diam. & Relat. Mater.*, 20 (2011), 1137
13. Y. Wu, Y. Lin, A. A. Bol, K. A. Jenkins, F. Xia, D. B. Farmer, Y. Zhu and P. Avouris *Nature*, 472 (2011), 74
14. J. Yu, G. Liu, A. V. Sumant, V. Goyal and A. A. Balandin, *Nano Letts.*, 12 (2012), 1603

# Chapter 2

## Background

### 2.1 Carbon

The carbon atom bears six electrons—two tightly bound, close to the nucleus, and the remaining four as valence electrons. The electronic configuration is  $1s^2, 2s^2, 2p^2$ , accordingly (Fig 2.1).

This implies a bivalence, which in fact does only exist in a few structures (carbenes). In the vast majority of its compounds, carbon is tetravalent. The preferred tetravalence may be explained with the hybridization model: the energetic difference between 2s- and 2p-orbitals is rather low compared to the energy released in chemical bonding. It is possible for the wave functions of these orbitals to mix and form four equivalent hybridized orbitals<sup>1</sup>. Fig 1.1b displays the hybrid orbitals and their spatial arrangement. A carbon atom forms bonds with one to four partners. Depending on the degree of hybridization, the compounds show different structural features: sp-hybridized C-atoms form linear chains, whereas  $sp^2$ - and  $sp^3$  hybridizations give rise to planar structures and 3D tetrahedral networks<sup>1</sup>. In sp- or  $sp^2$ -hybridized C-atoms there are two or one p-orbitals not taking part in hybridization, which can form additional  $\pi$ -bonds.

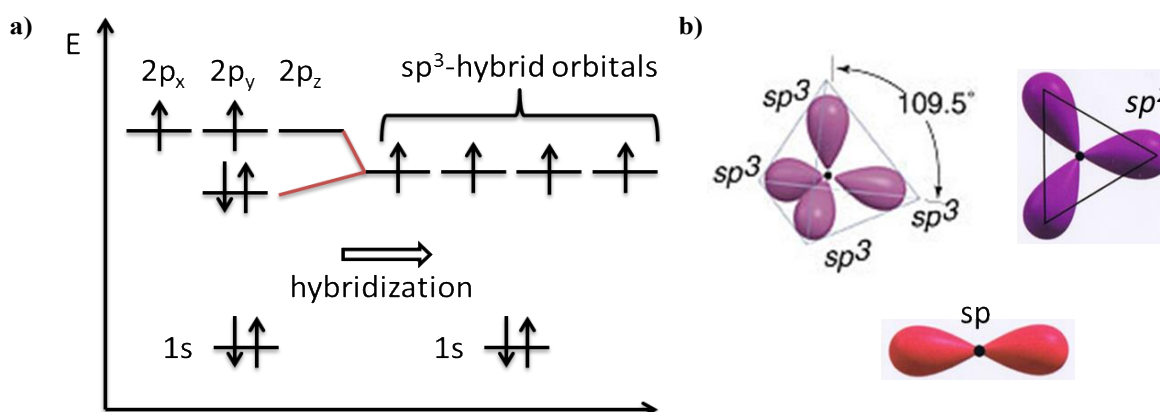
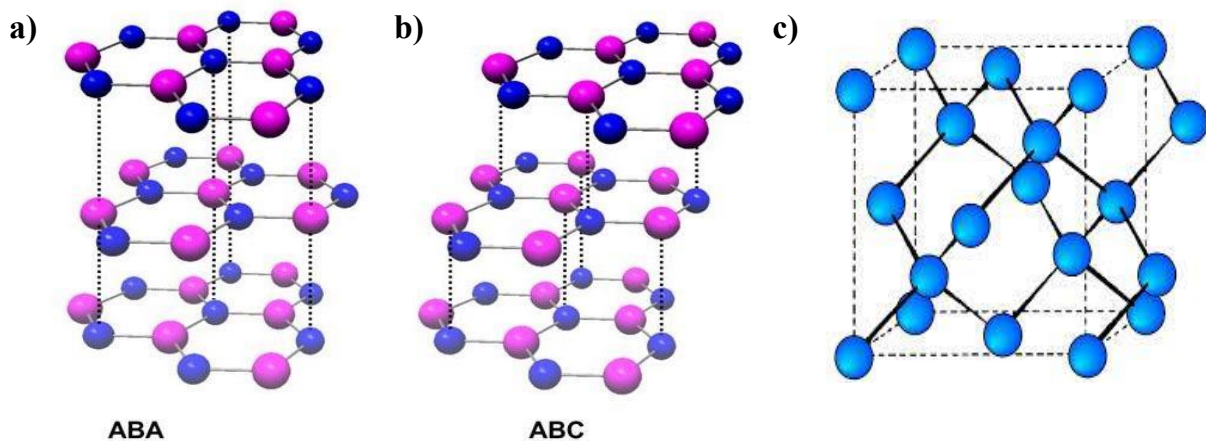


Figure 2.1 (a) Diagram of atomic orbitals and  $sp^3$ -hybridization. (b) Hybrid orbitals of carbon<sup>1</sup>.

Carbon takes the form of several allotropes, with graphite and diamond being two of the most well known. Graphite is characterized by a succession of distinct so-called graphene layers spreading over an  $xy$ -plane while stacked in a  $z$ -direction with weak van der Waals interactions among graphene layers. There are two different modifications, the hexagonal and the rhombohedral  $\beta$ -graphite<sup>2</sup>. The individual graphene layers in the hexagonal structure are stacked according to a sequence ABAB with the atoms of a layer B being situated above the centres of the hexagons in a layer A (Fig 2.2 a). In rhombohedral graphite, the layers are stacked in an ABCABC order (Fig 2.2 b), giving a rise to a bigger unit cell that also contains four carbon atoms. In diamond, each carbon atom has four immediate neighbors situated at the corners of a tetrahedron. All carbon atoms are  $sp^3$ -hybridized, and the bond length uniformly in 154.45 pm (Fig 2.2 c)<sup>2</sup>.



**Figure 2.2 (a) hexagonal graphite. (b) rhombohedral graphite. (c) diamond elementary cell<sup>1</sup>.**

## 2.2 Graphene

### 2.2.1 Graphene crystal structure

Graphene is a single sheet of carbon atoms arranged in a honeycomb structure, as shown in Fig 2.3(a). The carbon atom itself has the  $1s^2 2s^2 2p^2$  electron configuration, where the two  $1s$

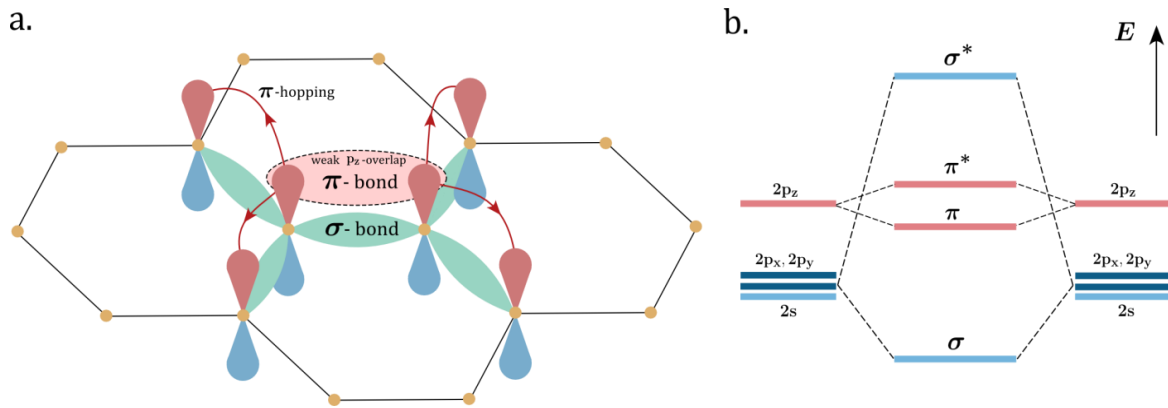


**Figure 2.3 (a) Graphene structure with  $\sigma$ - and  $\pi$ - bonds; (b) orbital energy diagram displaying the  $\sigma$  and  $\pi$  orbitals owing to hybridisation.**

orbital electrons form a closed shell while the other four electrons in the  $2s$  and  $2p$  orbitals are valence electrons that participate in the formation of chemical bonds. The unique electronic and mechanical properties of graphene arise from its crystal structure. From quantum mechanics we know that when atoms are in close proximity to each other, their respective orbital wavefunctions overlap to give us two new hybridized states owing to superposition. In the case of graphene and similarly other carbon materials, the hybridization is responsible for two types of chemical bands.

The  $sp^2$  hybridisation between the  $2s$  and the two  $2p_{x,y}$  valence orbitals gives rise to the so called  $\sigma$  bond orbitals

$$\sigma = \frac{1}{\sqrt{2}} [\varphi_{sp^2}^1(\mathbf{r}) + \varphi_{sp^2}^2(\mathbf{r})] \quad (2.2.1)$$

$$\sigma^* = \frac{1}{\sqrt{2}} [\varphi_{sp^2}^1(\mathbf{r}) - \varphi_{sp^2}^2(\mathbf{r})] \quad (2.2.2)$$

Where the  $\sigma^*$  state lies higher in energy and can be ignored as the electrons do not have enough energy to be excited into this orbital. Thus in graphene each carbon  $sp^2$  orbital can pairwise form a  $\sigma$  bond with the three closest neighbouring atoms. Due to Pauli principle each bond is fully occupied with two electrons of opposite spin and are therefore in bands well below the Fermi energy. These fully occupied bonds responsible for graphene's robust

crystal structure are electrically inert owing to the large energy gap between  $\sigma$  and  $\sigma^*$ . The question remains: why is graphene such a good conductor?

The answer lies with the fourth valence orbital  $2p_z$ . The hybridized orbitals, called  $\pi$  bonds, are define in a similar form

$$\pi = \frac{1}{\sqrt{2}}[\varphi_{p_z}^1(\mathbf{r}) + \varphi_{p_z}^2(\mathbf{r})] \quad (2.2.3)$$

$$\pi^* = \frac{1}{\sqrt{2}}[\varphi_{p_z}^1(\mathbf{r}) - \varphi_{p_z}^2(\mathbf{r})] \quad (2.2.4)$$

Since the  $2p_z$  orbitals are parallel to each other, their special overlap is significantly less compared to the  $sp^2$  orbitals and we can expect the  $\pi$  and  $\pi^*$  states to be much closer in energy, as shown in the orbital diagram described in Fig 2.3(b). It is this small energy difference that stimulates fast electron transfer between the two  $\pi$  states resulting in a large surface conductivity. We can picture this as a cloud of  $\pi$  electrons above and below the graphene surface.

The above statements have hopefully motivated the understanding of graphene's unique electronic properties in terms of the  $2p_z$  valence electrons. The next section will concentrate on how graphene's exceptional electronic properties are justified by its band structure.

## 2.2.2 Graphene band structure

### 2.2.2.1 Graphene and its reciprocal lattice

The graphene lattice structure can be described as a triangular Bravais lattice with a basis of two atoms per unit cell, atom A and B as show in Fig 2.4. The lattice vectors can be taken to be<sup>3</sup>

$$\mathbf{a}_1 = a\sqrt{3}(1,0) \quad \mathbf{a}_2 = a\sqrt{3}\left(-\frac{1}{2}, \frac{\sqrt{3}}{2}\right) \quad (2.2.5)$$

Where  $a=1.42 \text{ \AA}$  is the lattice spacing between nearest carbon atoms.

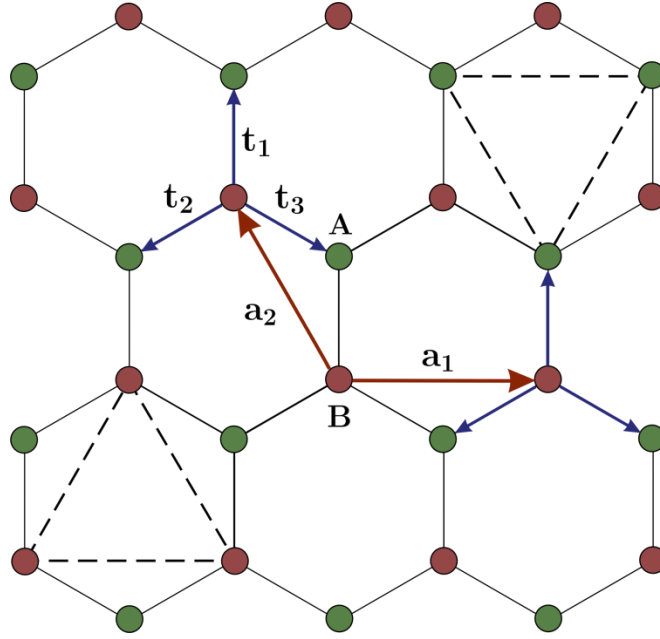


**Figure 2.4 Graphene direct lattice showing the lattice and translation vectors**

From the definition of a Bravais lattice, B atoms will be placed at sites  $\mathbf{R} = n_1 \mathbf{a}_1 + n_2 \mathbf{a}_2$ , for any  $n_1, n_2$  integer numbers, while A atoms will be placed at  $\mathbf{R} = n_1 \mathbf{a}_1 + n_2 \mathbf{a}_2 + \mathbf{t}$ , with the nearest neighbour translation vectors given by<sup>3</sup>

$$\mathbf{t}_1 = a\sqrt{3} \left( 0, -\frac{1}{\sqrt{3}} \right) \quad \mathbf{t}_2 = a\sqrt{3} \left( -\frac{1}{2}, -\frac{1}{2\sqrt{3}} \right) \quad \mathbf{t}_3 = a\sqrt{3} \left( \frac{1}{2}, -\frac{1}{2\sqrt{3}} \right) \quad (2.2.6)$$

For calculating the band structure of any crystal structure, we need to project the lattice in momentum space, which would give the reciprocal lattice<sup>4</sup>. In our case the reciprocal lattice for graphene is shown in Fig 2.5, where the lattice vectors are calculated from

$$\mathbf{b}_1 = 2\pi \frac{\mathbf{z} \times \mathbf{a}_2}{|\mathbf{a}_1 \times \mathbf{a}_2|} = \frac{2\pi}{a} \left( \frac{\sqrt{3}}{3}, 1 \right) \quad (2.2.7)$$

$$\mathbf{b}_2 = 2\pi \frac{\mathbf{z} \times \mathbf{a}_1}{|\mathbf{a}_1 \times \mathbf{a}_2|} = \frac{2\pi}{a} \left( 0, \frac{2}{3} \right) \quad (2.2.8)$$

As shown in Fig. 2.5, the unit cell in the reciprocal lattice, i.e. the first Brillouin zone contains points of high symmetry:  $\Gamma$ ,  $\mathbf{K}$  and  $\mathbf{K}'$ , and the  $\mathbf{M}$  points, where the  $\mathbf{K}$ ,  $\mathbf{K}'$  will be of particular interest in the following analysis for studying graphene's unique electronic properties<sup>5</sup>.

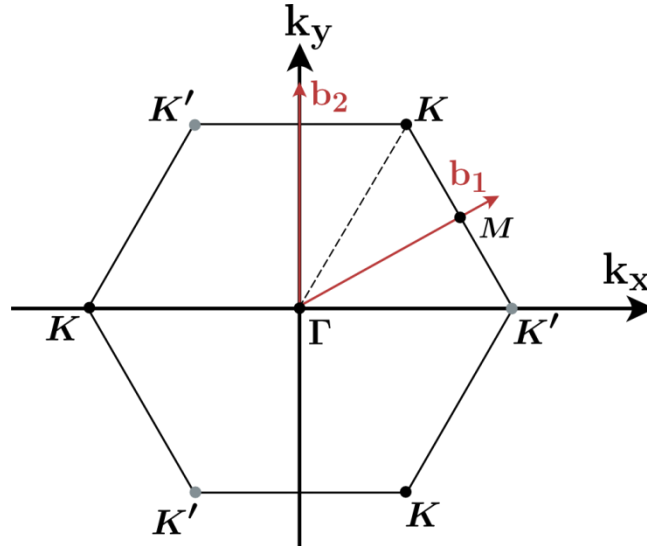


Figure 2.5 First Brillouin zone of graphene in reciprocal space

### 2.2.2.2 Graphene band structure

Early band structure calculations, using the free electron model and perturbation theory in a periodic lattice, were done by expanding the lattice wavefunction in terms of plane waves<sup>4</sup>. In some cases, using a fundamentally different approach can be useful. For the case of electrons interacting weakly with the lattice, which perfectly describes  $\pi$  electrons in graphene, the tight-binding approximation is employed<sup>3</sup>. Using this method, the electron wavefunction for the particular band is a linear combination of atomic orbitals (LCAO) well localised at the positions of the atoms. Since we have two carbon atoms per unit cell we can write the electron wavefunction<sup>3</sup>

$$\phi_c(\mathbf{r}) = A\phi(\mathbf{r} - \mathbf{t}_1) + B\phi(\mathbf{r}) \quad (2.2.9)$$

Where  $\phi(\mathbf{r})$  describes the  $p_z$  orbital of the  $sp^2$  carbon atom centred as  $\mathbf{r}$  and the A and B amplitudes describes the weights of two orbitals that need to be determined.

Electron dispersion is to a large extent linear, similar with that of light. This energy dispersion relation is shown in Fig. 2.6(b), describing the band structure along specific lines within the first Brillouin zone, while Fig. 2.6(a) displays the three dimensional version. The

band structure is composed of a valence band, i.e.  $\pi$ -states, and a conduction band, i.e.  $\pi^*$ -states. These states are orthogonal, and the valence and conduction bands touch at the six  $K, K'$  points, the so-called Dirac point.

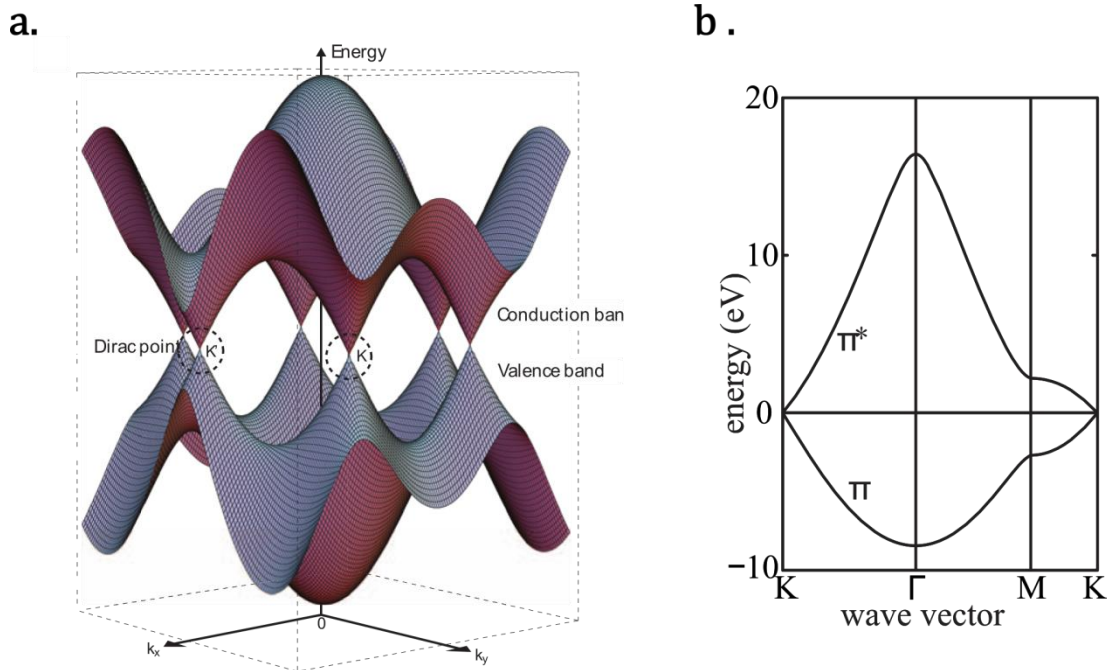


**Figure 2.6 (a) Energy dispersion for graphene band structure; (b) bandstructure along the points of interest in the First Brillouin zone.**

Interesting characteristics that can be noticed in this band picture are at the  $K$  and  $K'$  points, where the degeneracy is kept, while at  $M$  a gap is opened. Owing to spin degeneracy we have two electrons per  $k$  point and therefore the lower  $\pi$ -band is completely filled while the  $\pi^*$ -band is empty. This is the reason why graphene is referred to as the zero-gap semiconductor as the Fermi energy at zero temperature lies at the  $K$  and  $K'$  points.

The spinor character of the graphene wavefunction does not directly result from spin, but from the two atoms in the unit cell, which are defined as a pseudo-spin<sup>5</sup>. However, the allowed scattering process for the pseudo-spin is an interband transition where the direction of spin does not change, hence this scattering does not introduce electrical resistance. This

leads to the absence of backscattering processes<sup>6-8</sup>. Backscattering through long range interactions, arising from impurity and phonon scattering are forbidden and as a result experiments have shown graphene to have large values in electron mobility and elastic mean-free paths of the order of hundreds of nanometers<sup>9</sup>.

Finally, it should be mentioned that the wavefunction near the  $K, K'$  points obeys the two dimensional Dirac equation<sup>5</sup>, which would suggest the  $\pi$ - electrons behave as relativistic particles with general energies given by  $E = \sqrt{m^2c^4 + p^2c^2}$ . However, given the linear dispersion at the Dirac points  $E(k) = \pm v_F \hbar k$ , as shown in Fig 2.7, it can be stated that these  $\pi$ - electrons behave in fact as zero rest-mass relativistic Dirac Fermions. This has been proven experimentally almost 10 years ago<sup>10</sup>.

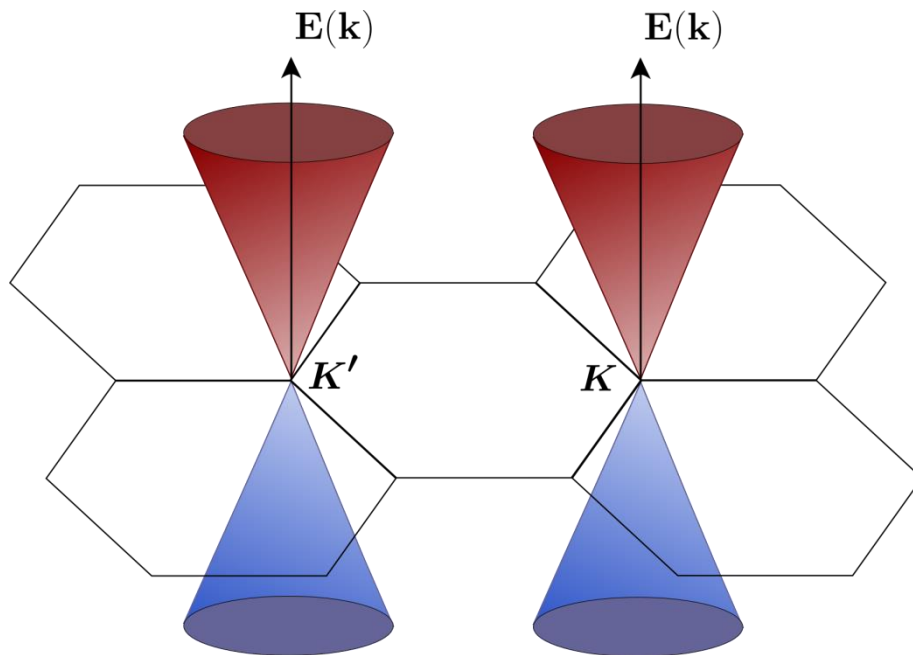


**Figure 2.7 Graphene linear energy dispersion at Dirac point**

### 2.2.3 Graphene properties and applications

Graphene has some outstanding physical properties that make it extremely appealing for applications in electronic and photonic.

- **Electronic properties**

One most useful properties of graphene is that it is a zero band gap semimetal with very high electrical conductivity. At the Dirac point in graphene, electron and hole are zero effective mass. Due to those physical properties, mobilities in excess of  $100,000 \text{ cm}^2/\text{Vs}^{11}$ , and saturation velocities of about  $5 \times 10^7 \text{ cm/s}^{12}$  have been reported. Graphene electrons act very much like photons in their mobility due to their lack of mass. However, the quality of graphene is limited the supporting substrate which leads to disorders of graphene<sup>13</sup>. For example, mobility is limited to  $40,000 \text{ cm}^2/\text{Vs}$  with  $\text{SiO}_2$  as substrate.

- **Mechanical and Thermal properties**

Due to the strength of graphene's  $0.142 \text{ Nm}$ -long carbon bonds, graphene is the strongest material as the monolayer, with an ultimate tensile strength of  $130 \text{ GPa}^{14}$ . In addition, owing to the thinness, mechanical strength, and flexibility, graphene has a very high current carrying capacity and high thermal conductivity (up to  $5000 \text{ W/mK}^{15}$ ).

- **Optical properties**

Graphene has the ability to absorb a rather large  $2.3\%$  of white light, which means  $97.7\%$  constant transparency<sup>16</sup>. The transmittance linearly decreases with the number of layers of graphene. Owing to the low density of states near the Dirac point in graphene, a shift of the Fermi level due to the gate causes a significant variation of charge density, leading to a remarkable change in transmission<sup>17</sup>. Due to the picoseconds timescale of graphene's relaxation and recombination of photo-generated electron-hole pairs, an ultrafast (up to  $40\text{GHz}$ ) and efficient photoresponse has been observed for graphene field effect transistor, which achieve graphene-based high speed optoelectronic devices<sup>18</sup>.

- **Applications**

Graphene-based FET is one of the most extensively explored applications. The first graphene FET was reported in 2004, which show a strong ambipolar electric field effect, but could not be used for the fabrication of effective FET due to the zero band gap<sup>19</sup>. Later top-gate graphene FET on different substrates were fabricated to show high RF frequency and high carrier carrying<sup>20-22</sup>. In order to improve the on-off ratio for effective transistors, graphene nanoribbons fabricated by chemical and lithographic methods have been studied theoretically and experimentally<sup>23,24</sup>.

Graphene is expected to be one of the most potential materials for future optoelectronic devices, including transparent electrodes for solar cells and liquid crystal displays to replace ITO due to its high cost, limited supply and brittle nature of indium<sup>25</sup>. Graphene has extraordinary thermal, chemical and mechanical stability with high transparency and atomic layer thickness, which become the ideal candidate for transparent electrode applications. Due to the unique 2D structure and high mobility, graphene has been used as an electron acceptor in photovoltaic devices, such as a layered graphene-quantum dot hybrid<sup>26</sup>. The tunable bandgap and large optical absorptivity of graphene are appealing for the efficient light absorbers.

Chemical and biological sensors based on graphene FET are keeping continuous interest because of its low noise, high sensitive, chemical stability and biocompatible nature<sup>27,28</sup>. The operational principle is based on the change of graphene electronic conductivity due to absorption of molecules on graphene surface. Several reports have demonstrated graphene sensor to NO<sub>2</sub>, NH<sub>3</sub>, DNA and dinitrotoulene<sup>28,29</sup>.

### 2.3 Diamond

In diamond, all carbon atoms are  $sp^3$ -hybridized. There are two modifications of diamond, the cubic and the hexagonal type, with the first one being the more abundant one<sup>29</sup>. The crystal lattice of normal diamond is face-centred cubic with eight atoms contained in the unit cell (Fig 2.8a)<sup>30</sup>. Hexagonal diamond is rare in nature, which was first discovered in a meteorite from Arizona in 1967. The hexagonal lattice like its cubic relative is built from tetrahedrons of carbon, but in a different way (Fig 2.8b)<sup>1</sup>. The unit cell contains four atoms. Another distinction of diamonds is made by their contents of nitrogen, shown in Table 2.1<sup>29</sup>.

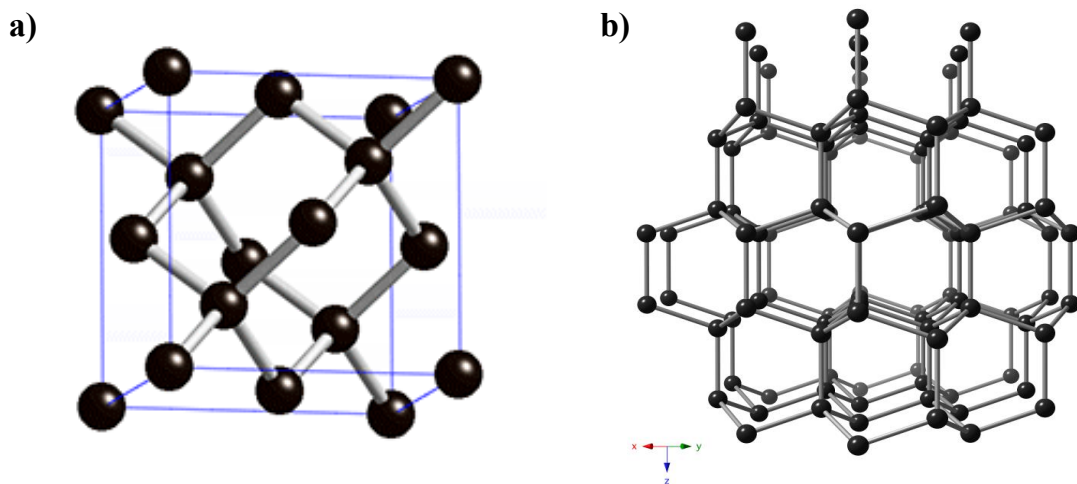


**Figure 2.8 (a) cubic diamond. (b) hexagonal diamond.**

Bulk diamond in nature cannot be effectively engineered into research because of the high cost. The development of synthesis of diamond, particularly chemical vapour deposition (CVD), has induced to the ability to grow diamond in thin films or coatings on different of shapes, which leads to specific applications for diamonds particular properties.

Single crystal diamond films are distinguished by a well-defined orientation of the crystal lattice throughout the film. In many case the (100)-plane is observed, whilst the (111)- and especially the (110)-face are uncommon. Polycrystalline diamond films do not consist of a coherent

**Table 2.1 Classification of natural diamond types (From Ref. 29)**

Type	Description
<b>Ia</b>	Nitrogen is the dominant impurity. It contains nitrogen as platelets with an approximate composition of $C_3N$ . It has a yellow or brown appearance. 98% of diamonds are into this category.
<b>Ib</b>	Nitrogen is distributed throughout the crystal and present as single substitutional atoms. These diamonds can appear deep yellow, orange, brown or greenish depending on the concentration and distribution for nitrogen atoms, which account for 0.1% of diamonds.
<b>IIa</b>	These diamonds have a miniscule amount of impurities present. They are colourless, which would be yellow, brown, pink or red. 1-2% of diamonds are this type.
<b>IIb</b>	This type of diamond contains boron as an impurity and appears blue, grey or near-colourless and occupy around 0.1% of diamonds.

layer with homogeneous orientation, but of numerous small grains. Compared with single crystal diamond films, the polycrystalline layers contain a much larger portion of  $sp^2$ -hybridized carbon, which is attributed to the large number of grain boundaries and has considerable effect on the electronic properties of these films<sup>31</sup>. The average size of the crystal defines the polycrystalline diamond, which the grain sizes range from nanometres to hundreds of micrometres usually are referred to as nanocrystalline and microcrystalline diamond, respectively<sup>32</sup>. Diamond in the form discrete nano-sized grains is nanodiamond.

### **2.3.1 Microwave-plasma CVD growth of diamond**

CVD had developed into the leading method for the preparation of thin diamond films. It is mainly characterized by a precipitation of carbon from the gas phase onto a substrate.

Applicable sources of carbon include methane, acetylene, or ethylene, which are normally admixed with a current of hydrogen. Plasma is generated by various forms of electrical discharges or induction heating. Microwave-plasma CVD has been used more extensively than others for the growth of diamond films and is the reactor type used in Diamond group of UCL.

The hydrogen required for the deposition of a diamond film can be applied in the plasma arising from microwave irradiation at a frequency of 2.45GHz. Fig 2.9 shows a schematic diagram of a modern microwave-plasma CVD system. The substrate is placed towards to the end of a tube, where the plasma is generated. The 2.45GHz microwave is coupled from the rectangular waveguide into the cavity via an axial antenna. The gases are introduced at the top of the reactor. A blue plasma ball is generated above the substrate, whose shape, size, colour and stability are dependent on the plasma power, the pressure and the gas composition.

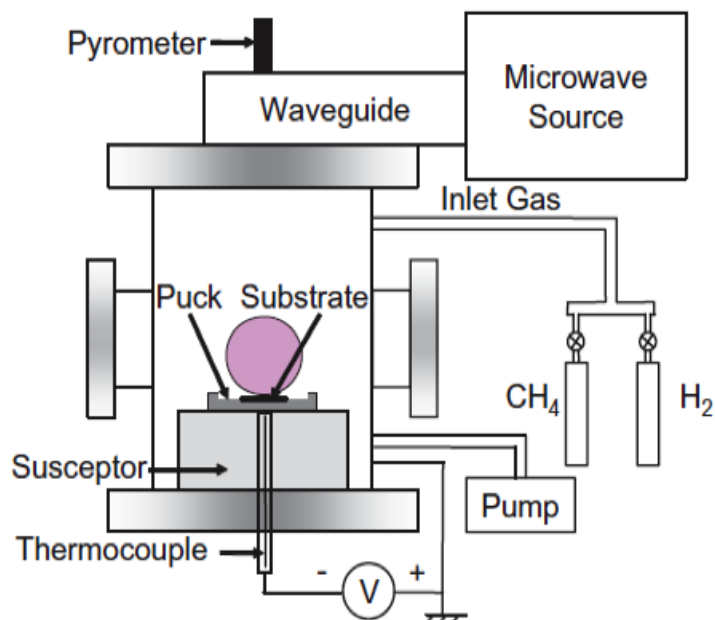


**Figure 2.9 MWPCVD Schematic Diagram (From Ref. 33)**

The MWPCVD has its pros and cons. An electrode-less process avoids contamination of the films. The plasma discharge at 2.45GHz is a higher frequency process than the radio

frequency (RF) discharges (13.5MHz), which produces high plasma energy to get higher concentration of atomic hydrogen and hydrocarbon radicals. Last, the method has spread widely because of commercially available in a variety of MWPCVD instrument yielding good results<sup>1</sup>. However, the inhomogeneity of the plasma has adverse effect to cause an uneven deposition of the diamond film on the substrates. Review of the various different CVD methods mentioned can be found in the book “Carbon Nanowalls”<sup>34</sup>.

### **2.3.2 Properties and Application of diamond**

Diamond has extreme mechanical and excellent electronic properties. Diamond is the greatest hardness and highest thermal conductivity among all the natural materials; has big band gap as electrical insulator, and as semiconductor achieved by doping; is chemically extremely inert, which is only attacked by aggressive reagents like chromosulfuric acid<sup>2,29</sup>. Diamond surface has negative electron affinity properties where the vacuum level is positioned below the conduction band, which minimum eliminates the surface emission barrier<sup>2</sup>.

- **Optical and electronic properties and applications**

The optical properties of diamond films is not showing any absorption in the spectral range from about 220 to 1000nm, which make diamond be an attractive material for spectroscopic application like as windows or lens systems. Diamond is an ideal material for the field emission owing on its great hardness, favourable chemical behaviour, high breakdown field strength, the good heat conductivity, and the large band gap.

- **Mechanical properties and applications**

Diamond has been well-known for long for its outstanding mechanical properties such as great hardness and low frictional coefficient. CVD diamond coatings are used on tools for industrial drilling tools and tips for measuring material surface.

- **Thermal properties and applications**

Diamond has the largest thermal conductivity even better than heat conductors such as silver or copper, which is applied in chapter 6. Current applications for diamond heat spreaders include mounting for laser diodes, laser diode arrays, and high power transistors.

- **Electrochemistry properties and applications**

Diamond is attractive to be used as material for electrodes. The reasons for this application are: firstly it is a very stable material both mechanics and chemistry, so it can be applied in highly aggressive media; secondly, it features favorable electrochemical properties like a very wide potential window and a low background current<sup>1</sup>. The low  $sp^2$ -content causes an inert behaviour in many media.

### **2.3.3 Nanodiamond particles: synthesis and applications**

Nanodiamond has become an important class of materials due to its excellent mechanical and optical properties, high surface area and the ability to functionalise the surface structure. The lattice structure of nanodiamond has been examined with various spectroscopic and crystallographic methods. Both cubic and hexagonal phases have been observed but the large portion of functional surface groups are on the surface<sup>35</sup>. Nanodiamond can be synthesised using a wide array of methods, such as the detonation technique, laser ablation<sup>36</sup>, high-energy ball milling of high-pressure high temperature diamond microcrystals<sup>37</sup>, and others<sup>38</sup>.

- **Detonation synthesis**

The generation of high pressure by means of a detonation in a confined container has been known for long. Two methods of producing nanodiamond processes exist. The first is based on a mixture of carbon containing material with explosives. The product consists of primary particles than sinter during the growth period. Different particles are obtained depending on the ambient conditions. The second method is solely based on an explosive or mixture of different blasting agents. A variety of explosives with a negative oxygen balance is available on an industrial scale, including TNT (2,4,6-trinitrotoluene), hexogen ( cyclo-1,3,5-trimethylene-2,4,6-trinitrotoluene), HMX (cyclo-1,3,5,7-tetramethylene-2,4,6,8-tetranitramine) and TATB (traminonitrobenzene)<sup>1,25</sup>. The surface chemistry of nanodiamond has been studied in considerable details by XPS and FTIR for different functional groups including –COOH, -O-C=O, -OH and –C-O-C, which open up the possibilities for selective attachment of other functional groups<sup>39</sup>.

- **Applications of nanodiamond**

Nanodiamond inherits most properties of bulk diamond and delivers them at the nanoscale. They can be used to provide a homogenous seeding layer applied in chapter 6. The superior mechanical and thermal properties of nanodiamond make it as an excellent filler material for composites. Moreover, the biocompatibility and chemical stability of nanodiamond is suited for bio medical applications with different functional groups. Nanodiamond has also shown to have applications in the field of drug delivery to carry a board range of therapeutics, dispersability in water due to big surface area<sup>35</sup>.

## 2.4 Diamond-like carbon (DLC)

Diamond and graphite are stable forms of carbon with well-defined crystallographic structures. Crystalline diamond is composed entirely of tetrahedral coordinated  $sp^3$ -bonded carbon. Diamond and diamond films are thus constituted of a well-defined material with fixed properties. In contrast, DLC films lack any long-range order and contain a mixture of  $sp^3$ ,  $sp^2$ , and sometimes even  $sp^1$ -coordinated carbon atoms in a disordered network. DLC is a metastable form of amorphous carbon or hydrogenated amorphous carbon (a-C:H) with a significant fraction of  $sp^3$  bonding<sup>40-42</sup>. The composition of a DLC is best shown on the ternary phase diagram, as shown in Fig. 2.10. The ta-C refers to tetrahedral amorphous carbon, a highly  $sp^3$  bonded a-C with up to 80 – 90%  $sp^3$  bonding, while ta-C:H refers to its hydrogenated analogue.

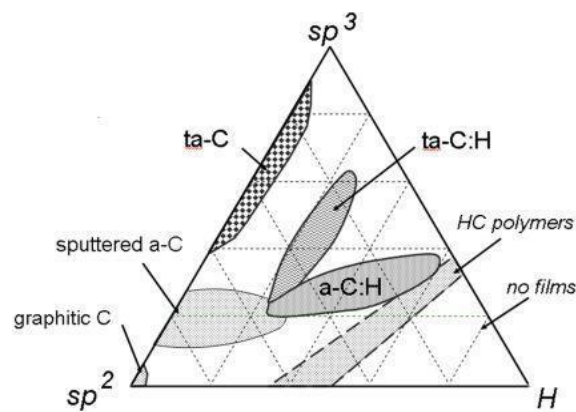


**Figure 2.10 Ternary phase diagram of C: H system (From Ref.40).**

The optical band-gap of DLCs varies in the range 1 to 4 eV. It is controlled by the configuration of the  $sp^2$  sites and the size and distortion of the clusters<sup>42</sup>. In practice, it varies quite closely with the ratio of  $sp^2$  bonding. The widest gap is found for polymeric a-C:H. Recently it has been found that ta-C prepared in a properly filtered deposition system has a gap of 3.6 eV, larger than previously known<sup>43</sup>. A simple model is that the band gap varies because the width of these distributions increases in proportion to the  $sp^2$  fraction<sup>44</sup>.

### 2.4.1 Growth of DLC

Since diamond-like carbon is a metastable material, DLC must be deposited while its surfaces are continuously bombarded with energetic ions in order to obtain diamond-like properties. This prevents the formation of either fully amorphous or fully crystalline material<sup>45</sup>. The metastable structure of DLC films most likely originates from the thermal and pressure spikes produced by the impinging energetic species on the growth surface<sup>46</sup>. A variety of techniques based on beam and plasma techniques have evolved for the preparation of DLC. Such methods include single low-energy beams of carbon ions, dual ion beams of carbon and argon, ion plating, rf sputtering or ion-beam sputtering from the carbon/graphite target, vacuum-arc discharges, or laser ablation. Details of the different deposition methods and of specific references can be found elsewhere<sup>47</sup>. While some of the mentioned methods are being extensively used in investigations of non-hydrogenated carbon (taC = tetrahedral carbon), the main techniques for depositing diamond-like carbon films are, however, based on plasma-enhanced chemical vapor deposition (PECVD) reactors and magnetron sputtering.

PECVD deposition of DLC is generally performed in plasmas sustained by rf excitation, but dc discharge systems, microwave plasmas, and electron cyclotron resonance (ECR) systems have also been used. Of the various possible geometries, parallel-plate reactors are preferred because they allow the deposition of uniform films over large areas and can be scaled up relatively easily for coating large areas. In the rf PECVD reactors, the substrates are placed on the rf-powered electrode, thus attaining a negative dc self bias, which is dependent on the precursor gases used, deposition parameters (e.g. power, pressure), and relative area of electrodes<sup>48</sup>. In dc PECVD the plasma is sustained by applying the negative dc voltage to the substrate electrode. Any hydrocarbon can be used as a precursor for DLC deposition by the PECVD method, provided it has sufficient vapor pressure to be transported into the reactor.

Details on the use of specific precursors can be found elsewhere<sup>49</sup>. Hydrogen or argon is sometimes added to the hydrocarbon precursor used in the PECVD reactors; however, the effect of such additions to the properties of DLC is not obvious. The growth rates of the films may decrease with dilution of the precursor with hydrogen, and in some cases the addition of hydrogen can have a detrimental effect on the film properties. In other cases it was found that under certain plasma conditions, the addition of argon to the hydrocarbon precursor can improve DLC properties.

The total hydrogen content critically determines film structure at the atomic level (the ratio between  $sp^3$ - and  $sp^2$ -coordinated carbon atoms), and therefore the physical properties of the films. Hydrogen content is also the key to obtaining a wide optical gap and high electrical resistivity, because it passivates the dangling bonds in the amorphous structure<sup>50</sup>. DLC films deposited from hydrocarbons must include hydrogen in concentrations from 17% to 61% in order to obtain diamond-like properties. The loss of hydrogen through annealing at high temperatures generally causes a collapse of the structure to a graphite-like phase dominated by  $sp^2$  bonds.

#### **2.4. 2 Properties and applications of DLC**

- **Optical properties**

DLC films are typically transparent in the infrared, with the exception of the CH absorbing bands mentioned earlier, are weakly absorbing in the visible spectrum, and are increasingly absorbing with decreasing wavelength in the UV. Their hydrogen content is critical in controlling their optical properties, and removal of hydrogen from hydrogenated DLC films causes the loss of IR transparency. A wide range of optical band-gap values ( $E_{opt}$ ), spanning the range from 0.38 to 2.7, have been reported for DLC films prepared under similar

conditions, indicating the dependence of the property on the deposition system actually being used<sup>51</sup>. For otherwise similar deposition conditions,  $E_{opt}$  was found to decrease strongly for DLC films deposited above 250°C. This behaviour reflects the role of hydrogen in stabilizing the structure of DLC layers<sup>51</sup>. Films deposited at lower temperatures (in the range 25-250°C) contain significant concentrations of hydrogen; most of the  $sp^3$ -coordinated carbon atoms, as well as a substantial fraction of the  $sp^2$ -coordinated carbons, are bound to at least one hydrogen atom. When the release of hydrogen is induced in these materials, they revert to the configuration of lowest energy, i.e. graphite.

- **Electrical properties**

Owing to the range of properties of the naturally occurring forms of carbon, i.e. graphite and diamond, the electrical properties of diamond-like carbon films can vary from that of a semimetal to that of a wide-bandgap insulator. Electronic transport itself is quite complex in DLC as a result of its disordered structure. Diamond is characterized by high electron mobilities and, since it is a wide-bandgap semiconductor, diamond-based devices such as diodes can continue to function properly at temperatures in excess of 500°C; a wide variety of applications for such high-temperature electronics are being considered. In contrast, DLC has neither the wide energy gap nor the thermal stability to operate in such an environment. The electronic and optical properties of hydrogenated DLC behave to a certain extent in a fashion similar to those of hydrogenated amorphous silicon.

Diamond-like carbon films are generally characterized by high electrical resistivities spanning a large range of values, from  $10^2$  to  $10^{16}$  Ωcm, depending on the deposition conditions<sup>52</sup>. Their electrical resistivity has been found to be strongly reduced by up to seven

orders of magnitude by incorporation of metals. Nitrogen incorporation also reduces the electrical resistivity of the films.

Hydrogen, which stabilizes the  $sp^3$  bonds and determines the carbon hybridization ratio, is required for obtaining a high electrical resistivity. However, electrical resistivity differences of several orders of magnitude have been found between films having small or no differences in total hydrogen content. Because the electrical properties of DLC films depend on the carbon hybridization, which in turn is affected by C-H bonding, the electrical conductivity is determined by the bound and not by the total hydrogen concentration in the films and, for films deposited under similar conditions, the conductivity decreases with increasing concentration of bound hydrogen in the films.

- **Chemical properties**

At room temperature, DLC films are chemically inert to practically any solvent and are not attacked by acids, alkalis, or organic solvents. The films are inert even to strong acid mixtures, such as the "acid etch" ( $HNO_3:HF = 7:2$ ) and to exposure to alkali solutions at  $85^\circ C$  for several hours. As a result of their chemical resistance, DLC films can be used as corrosion-resistant coatings<sup>48</sup>. The films and their modifications can be removed from a substrate by exposure to atomic oxygen or fluorine species generated in a plasma, which react with the carbonaceous films to produce volatile  $CO_x$  and  $CF_y$  species which are pumped out of the system<sup>53</sup>. Reactive ion etching in oxygen- or fluorine-containing plasmas can be used to pattern DLC films.

- **Mechanical properties**

DLC films are characterized by high hardness, spanning the range from 10 to 30 GPa, associated with high intrinsic compressive stresses in the range from 0.5 to 7 GPa. The high internal stresses limit the thickness of films that can be used for various applications, often to less than 1  $\mu\text{m}$ . Adhesive forces must overcome the high stresses in order to prevent delamination of the film from the substrate. The stresses in DLC films are generally directly correlated to the fraction of  $\text{sp}^3$  carbon<sup>54</sup>. For rf PECVD films, the intrinsic stresses therefore depend on the combination of deposition parameters which affect the  $\text{sp}^3$  C hybridization. Because of the interdependence of the plasma parameters, stress dependency reported with regard to one specific parameter is valid for only a specific plasma system. Stresses have been found to decrease with increasing deposition pressure and to have a bias relation which depends on other deposition parameters. The intrinsic stresses in DLC films are also correlated with changes in hydrogen content obtained by changing deposition parameters. It was observed that films containing smaller amounts of hydrogen had higher stresses than DLC films containing higher amounts of hydrogen<sup>54</sup>.

- **Tribological properties**

Wear protection is needed for surfaces in kinetic contact, in situations which generally also require low friction between the moving surfaces. As a result of their high hardness, DLC films are utilized as wear-resistant protective coatings for metals and for optical or electronic components<sup>48</sup>. The use of DLC is especially attractive in applications where the thickness of the protective film is limited to less than 50 nm, as for example in the case of magnetic recording media, where the trend toward higher-density data storage has led to the requirement of very low flying heights between a disk and a recording head. The coating must be able to protect the magnetic media against wear and corrosion but must also be thin enough not to impede the achievement of high recording density.

- **Applications**

The unique properties of DLC films together with the possibility of adjusting the properties by choosing appropriate deposition parameters, make them suitable for a variety of applications. The exploited properties include high wear resistance and low friction coefficient, chemical inertness, infrared transparency, high electrical resistivity, and, potentially, low dielectric constant. Owing to their IR transparency, DLC films can be used as antireflective and scratch-resistant wear-protective coatings for IR windows or lenses made of Ge, ZnS, or ZnSe, where they also act as an antireflective coating at the used wavelength of 8-13  $\mu\text{m}$ <sup>51</sup>. Aluminum mirrors used in optical imaging deteriorate with time as a result of exposure to atmosphere. This deterioration can be prevented by coating the surface of the mirrors with DLC films. Because of their absorbance in visible light, DLC coatings can be applied as scratch-resistant coatings on sunglasses. The low deposition temperatures of DLC films allow their use as a wear-protective layer on products made of plastic. Currently, DLC films are used for protection against abrasion of sunglass lenses made of polycarbonate.

The most widespread use of DLC films is in wear and corrosion protection of magnetic storage media. The protective coating must be resistant to wear and corrosion, but also thin enough so as not to impede the achievement of high recording density; DLC coatings are ideal for such applications. DLC is used as a corrosion- and wear-protective coating for both magnetic disks and magnetic heads, and is also used for corrosion protection of metal films during the manufacturing of magnetic heads<sup>55</sup>. Tapes for video recording or magnetic data storage, using ferromagnetic metal as a recording medium, as well as the metallic capstans in

contact with the tapes, are also protected with DLC coatings to reduce wear and friction, thus extending the life of the tapes.

Diamond-like carbon films appear to be biocompatible, and applications are being developed for their use in biological environments<sup>56</sup>. One major reason for the failure of metallic implants in the body is their corrosion by body fluids. In vitro tests have shown that DLC coatings allow cells to grow without inflammatory response. Because of their chemical inertness and impermeability to liquids, DLC coatings could protect the implants against corrosion and serve as diffusion barriers. DLC films are being considered for use as coatings of metallic as well as polymeric (e.g. polyurethane, polycarbonate, and polyethylene) biocomponents in order to improve their compatibility with body tissues<sup>56</sup>. Their wear resistance is another useful property for bioapplications. Diamondlike carbon films, deposited on stainless steel and titanium alloys used for components of artificial heart valves, have been found to satisfy both mechanical and biological requirements and to be capable of improving the performance of these components. The same properties may make DLC films useful as protective coatings for joint implants.

## Reference

1. Krueger, A. Carbon Materials and Nanotechnology. (Wiley-VCH Verlag GmbH & Co. KGaA, 2010).
2. Group, F. Carbon nanomaterials © 2006. (2006).
3. Ihn, Thomas, *Semiconductor Nanostructures: Quantum States and Electronic Transport*, Oxford University Press(2010)
4. N.W. Ashcroft and N.D. Mermin, *Solid State Physics*, Saunders College, Philadelphia(1976)
5. Castro Neto, A. H. and Guinea, F. and Peres, N. M. R. and Novoselov, K. S. and Geim, A. K., The electronic properties of graphene, *Rev. Mod. Phys.*, 81(1) 109-162, American Physical Society (2009)
6. T. Ando, The electronic properties of graphene and carbon nanotubes, *NPG Asia Matter*, 1(1)17-21(2009)
7. T. Ando, T. Nakanishi, Impurity Scattering in Carbon Nanotubes – Absence of Back Scattering, *J. Phys. Soc. Jpn* 67, 1704 (1998)
8. T. Ando, T. Nakanishi and R. Saito, Berry's Phase and Absence of Back Scattering in Carbon Nanotubes *J. Phys. Soc. Jpn* 67(8), 2857-2862 (1998)
9. P. Avouris, Graphene: Electronic and Photonic Properties and Devices, *Nano Lett*, 10, 4285-4294, (2010)
10. K.S. Novoselov, A.K. Geim et. al, Two-dimensional gas of massless Dirac fermions in graphene, *Nat. Lett* 438, 197-200 (2005)
11. Bolotin, K. I. et al. Ultrahigh electron mobility in suspended graphene. *Solid State Commun.* 146, 351–355 (2008).
12. Schwierz, F. Graphene transistors. *Nat. Nanotechnol.* 5, 487–96 (2010).
13. Ju, L. et al. Photoinduced doping in heterostructures of graphene and boron nitride. *Nat.Nanotechnol.* 9, 348–52 (2014).
14. Engineering, I. Multifaceted Graphene : Novelty in. 11807–11811 (2014).
15. Balandin, A. a et al. Superior thermal conductivity of single-layer graphene. *Nano Lett.* 8, 902–7 (2008).
16. Nair, R. R. et al. Fine structure constant defines visual transparency of graphene. *Science* 320, 1308 (2008).
17. Mak, K. F. et al. Measurement of the Optical Conductivity of Graphene. *Phys. Rev. Lett.* 101, 196405 (2008).
18. Xia, F., Mueller, T., Lin, Y.-M., Valdes-Garcia, A. & Avouris, P. Ultrafast graphene photodetector. *Nat. Nanotechnol.* 4, 839–43 (2009).
19. Novoselov, K. S. et al. Electric field effect in atomically thin carbon films. *Science* 306, 666–9 (2004).

20. Wu, Y. et al. High-frequency, scaled graphene transistors on diamond-like carbon. *Nature* 472, 74–8 (2011).
21. Yu, J., Liu, G., Sumant, A. V, Goyal, V. & Balandin, A. a. Graphene-on-diamond devices with increased current-carrying capacity: carbon sp<sup>2</sup>-on-sp<sup>3</sup> technology. *Nano Lett.* 12, 1603–8 (2012).
22. Meric, I., Baklitskaya, N., Kim, P. & Shepard, K. L. RF performance of top-gated, zero-bandgap graphene field-effect transistors. 2008 IEEE Int. Electron Devices Meet. 1–4 (2008). doi:10.1109/IEDM.2008.4796738
23. Fiori, G. & Iannaccone, G. Simulation of Graphene Nanoribbon Field-Effect Transistors. *IEEE Electron Device Lett.* 28, 760–762 (2007).
24. Choi, W., Lahiri, I., Seelaboyina, R. & Kang, Y. S. Synthesis of Graphene and Its Applications: A Review. *Crit. Rev. Solid State Mater. Sci.* 35, 52–71 (2010).
25. Guo, C. X. et al. Layered graphene/quantum dots for photovoltaic devices. *Angew. Chem. Int. Ed. Engl.* 49, 3014–7 (2010).
26. Yin, Z. et al. Real-time DNA detection using Pt nanoparticle-decorated reduced graphene oxide field-effect transistors. *Nanoscale* 4, 293–7 (2012).
27. Schedin, F. et al. Detection of individual gas molecules adsorbed on graphene. *Nat. Mater.* 6, 652–5 (2007).
28. Fowler, J. D. et al. Practical chemical sensors from chemically derived graphene. *ACS Nano* 3, 301–6 (2009).
29. Poerson. H.O, Handbook of Carbon, Graphite, Diamond and Fullerenes, Noyes, Park Ridge, NJ (1993)
30. Element Six (2001-2012), Diamond Crystallography. Available at :<http://pages.townson.edu/ladon/carbon.html>.
31. Bundy. F. P, Strong H. M., and Wentorf R. H., Jr., Chemistry and Physics of carbon, Vol. 10, Marcel Dekker Inc. (1973).
32. Zoski C. G., Handbook of Electrochemistry, Elsevier B.V., 1st edition (2007).
33. Angus, J. C., Development of Low-Pressure Diamond Growth in the United States, In Synthetic Diamond: Emerging CVD Science and Technology, Spear, K.E. and Dismukes, J. P. (Eds.), JohnWiley & Sons, New York, 21-39, (1994).
34. Hiramatsu, M. and Hori M., carbon Nanowalls: Synthesis and Emerging Applications, Springer, (2010).
35. Mochalin, V. N., Shenderova, O., Ho, D., & Gogotsi, Y. The properties and applications of nanodiamonds. *Nature Nanotechnology*, 7(1), 11–23.(2012).
36. Yang, G. W., Wang, J. B. and Liu, Q.X. *Journal of Physics: Condensed Matter*, 10, 7923-7927, (1998).
37. Boudou, J. P., *Nanotechnology* 20, 235602, (2009).

38. Mochalin, V. N., Shenderova, O., Ho, D., and Gogotsi, Y. The properties and application of diamonds, (2012).
39. Baidakova, M. and Vul, A., *Journal of Physics D: Applied Physics*, 40, 6300-6311, (2007).
40. J. Robertson, *Adv. Phys.* 35, 317 (1986).
41. J. Robertson and E. P. O'Reilly, *Phys. Rev. B* 35, 2946 (1987).
42. J. Robertson, *Prog. Solid State Chem.* 21, 199 (1991).
43. J. Robertson, *Phys. Rev. B* 53, 16302 (1996).
44. K. Teo, A. C. Ferrari, J. Tsai, J. Robertson, W. I. Milne, *J. Appl. Phys.* 89, 3706 (2001).
45. C. Weissmantel, in *Thin Films from Free Atoms and Molecules*, K. J. Klabunde, Ed., Academic Press, Inc., New York, 153, (1985).
46. A. Grill and B. Meyerson, in *Synthetic Diamond: Emerging CVD Science and Technology*, K. E. Spear and J. P. Dismukes, Eds., John Wiley & Sons, Inc., New York, 91, (1994).
47. A. Grill, *Cold Plasma in Materials Fabrication; From Fundamentals to Applications*, IEEE Press, New York, (1994).
48. B. Meyerson and F. Smith, *J. Non-Cryst. Solids* 35/36, 435 (1980)
49. H.-C. Tsai and D. B. Bogy, *J. Vac. Sci. Technol. A* 5, 3287 (1987)
50. M. A. Tamor, W. C. Vassell, and K. R. Carduner, *Appl. Phys. Lett.* 58, 592 (1991)
51. K. Honglertkongsakul, P.w.May, and B. Paosawatyanong. *Diamond & Related Materials*, 19,999, (2010).
52. A.Grill. *Thin Solid films*, 355-356, 189, (1999).
53. S. Bai, T. Onodera, R. Nagumo. *J. Phys. Chem*, 116, 12559 (2012).
54. M. A. Tamor, W. C. Vassell, and K. R. Carduner, *Appl. Phys. Lett.* 58, 592 (1991)
55. H.C. Tsai and D.B. Bogy. *J. Vac. Sci. Technol. A*5, 6 (1987).
56. L. Lu, M. W. Jones, and R. L. Wu. *Bio-Medical Materials and engineering.* 3, 223(1993)

# Chapter 3

## Experimental Methods

### 3.1 Introduction

This chapter describes some of the characterization techniques employed throughout this report. It begins with an account of some widely utilized techniques such as atomic force microscopy (AFM), Raman spectroscopy, X-ray photoelectron spectroscopy (XPS), Hall effect measure instrument, Impedance spectroscopy, Ultraviolet-visible spectroscopy, Reactive-ion etching (RIE), and Focused ion beam (FIB). Then the chapter briefly goes through the processing steps required for fabricating the graphene-diamond, graphene-DLC heterostructures.

### 3.2 Atomic force microscopy (AFM)

AFM is a powerful technique to image any kind of surface. AFM has provided information on the topography of diamond layers, the roughness of diamond, nanodiamond, DLC surface and the thickness of nanodiamond. AFM can be used in different modes, contact mode where the tip is constantly adjusted to maintain a constant deflection and consequently constant height above the surface and non-contact mode (tapping) where the cantilever is vibrated at its resonant frequency and changes in this frequency due to interaction with the surface are measured to determine the topology<sup>1</sup>.

Surface texture is important to understand material surfaces, which are crucial to the functional performance of certain engineering elements. One component of surface texture is

roughness, which is important for graphene supporting materials. It is quantified by vertical spacing of real surface with the larger the spacing, the rougher the surface. The roughness average, Ra, is a commonly used method to define the roughness due to its simplicity and is defined as,

$$R_a = \frac{1}{L} \int_0^L |Z(x)| dx \quad (3.2.1)$$

Where Z(x) is the function that describes the surface profile analysed in terms of height (Z) and position (x) of the sample over the evaluation length “L”<sup>2</sup>. Ra is the arithmetic mean of the absolute values of the height of the surface profile Z(x). Also the root mean square roughness, Rq, is utilized to calculate the roughness and is similar to Ra, but takes into account the distinction between peaks and valleys by determining the mean squared absolute values roughness profile<sup>2</sup>, defines as,

$$R_q = \sqrt{\frac{1}{L} \int_0^L |Z^2(x)| dx} \quad (3.2.2)$$

For example, different termination nanodiamond samples were measured with AFM to check the coverage of nanodiamond, the roughness and the thickness of nanodiamond in Fig 3.1.

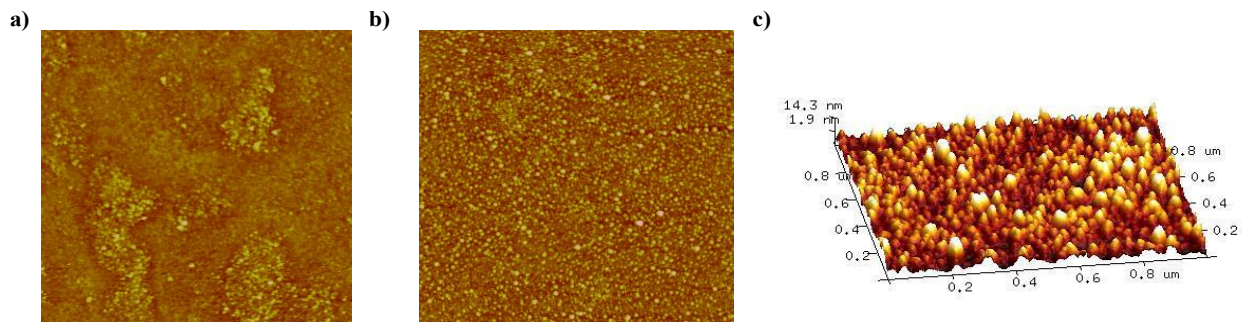


**Figure 3.1 (a) H-terminated nanodiamond 10µm AFM scan image with height range 15.8nm. (b) O-terminated nanodiamond 10µm AFM scan image with height range 10.2nm. (c) 3D AFM scan image H-terminated nanodiamond shows the thickness which proves nanodiamond is monolayer.**

### 3.3 Raman spectroscopy

#### 3.3.1 Raman scattering

Raman spectroscopy is a spectroscopic technique based on the Raman effect, i.e. inelastic scattering of monochromatic light from a laser source. This spectroscopic technique is a reflective measurement, in the sense that the photons that are absorbed by the sample are re-emitted. The Raman effect is based on molecular deformation by inducing an electric dipole moment. Due to these periodical deformations, molecules start vibrating with a characteristic frequency. If we consider a monochromatic laser light source with frequency, that excites the molecules into oscillating dipoles, these dipoles will emit light at three different frequencies<sup>3</sup>, as shown in Fig 3.2, corresponding to the following cases:

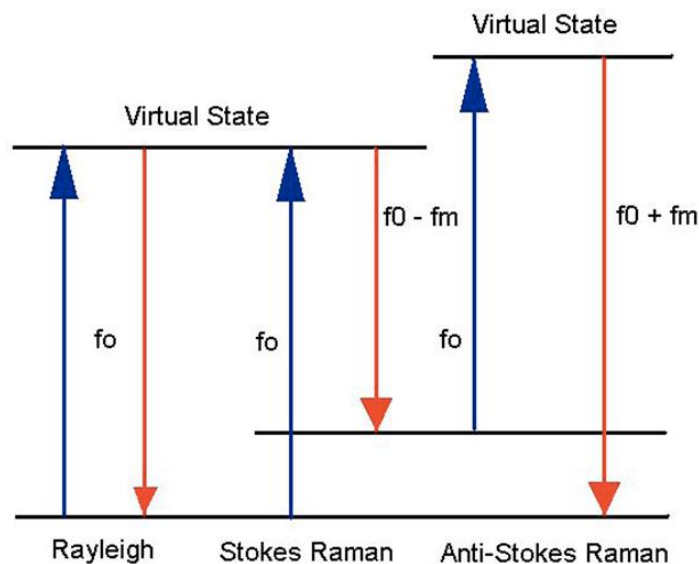


**Figure 3.2: Elastic Rayleigh and inelastic Raman scattering**

- A molecule absorbs a photon with frequency  $\nu_0$  is excited to a virtual state and relaxes to its original vibrational state where it re-emits a photon with the same frequency  $\nu_0$ . This leads to elastic scattering known as Rayleigh scattering, where there is no change in energy between the incoming and scattered photons<sup>3</sup>.

- A molecule absorbs a photon of frequency  $\nu_0$  in their basic vibrational state. Part of the photon's energy is transferred to the Raman-active mode with frequency  $\nu_m$ , and the frequency of the re-emitted light is  $\nu_0 - \nu_m$ . This is the case where the scattered photon has a lower energy than the absorbed photon, known as Stokes Raman scattering<sup>3</sup>.
- A molecule already in the excited vibrational state absorbs a photon of frequency  $\nu_0$ . Excessive energy is released while the molecule returns to its original vibrational state and the re-emitted photon has a frequency of  $\nu_0 + \nu_m$ . This is the case where the scattered photon has a higher energy than the absorbed photon, known as anti-Stokes Raman scattering<sup>3</sup>.

The spectrum of the emitted photons is termed the Raman spectrum that is typically displayed according to the energy difference with the absorbed incident photons.

### 3.3.2 Raman spectra for graphene

From a molecular perspective all carbon materials are entirely composed of C-C bonds. The orientation of these bonds differs for every carbon allotrope and to characterise their molecular structure there is need of a technique that is highly sensitive to slight changes in the geometry of C-C bonds<sup>4</sup>. Raman spectroscopy is most sensitive to highly symmetric covalent bonds with little or no dipole moment, which is convenient for C-C bonds that fit this description perfectly.

The Raman spectrum of graphene and graphene layers has been studied experimentally by Ferrari *et al*<sup>5</sup> and results indicate that the graphene electronic structure is captured in its Raman spectrum that is shown to evolve with the number of layers. Fig. 3.3(a) compares the 514 nm Raman spectra of graphene and bulk graphite. The two most significant features of

the spectra are the G band at  $1580\text{cm}^{-1}$  and the G' or 2D band at  $2700\text{ cm}^{-1}$ . The G band, known as the graphite or tangential band, arises from the vibrational frequency of the  $\text{sp}^2$  bond energy. The 2D band is a result of two phonons double resonance scattering. The D band, situated at  $1350\text{ cm}^{-1}$ , is a defect activated double resonance Raman process<sup>5</sup>. If the D peak is not observed in the graphene layers this confirms the absence of a significant number of defects. One obvious difference between the two spectra in Fig 3.3 (a) is that the peak in the 2D band is much more intense than the one in the G band in graphene compared to bulk graphite. Taking a closer look at the 2D band for different number of layers, both 512nm and 633nm excitations (see Fig 3.3 (b,c)) it can be seen how both the shape of the band and the peak positions change with the number of layers<sup>5</sup>. The peak shift is a result of the interactions between the stacked graphene layers, while the change in the shape of the band is a result of the different inter layer interactions that occur at different sites within the layer (suggested by the curve fitting in Fig 3.3(c))<sup>5</sup>.

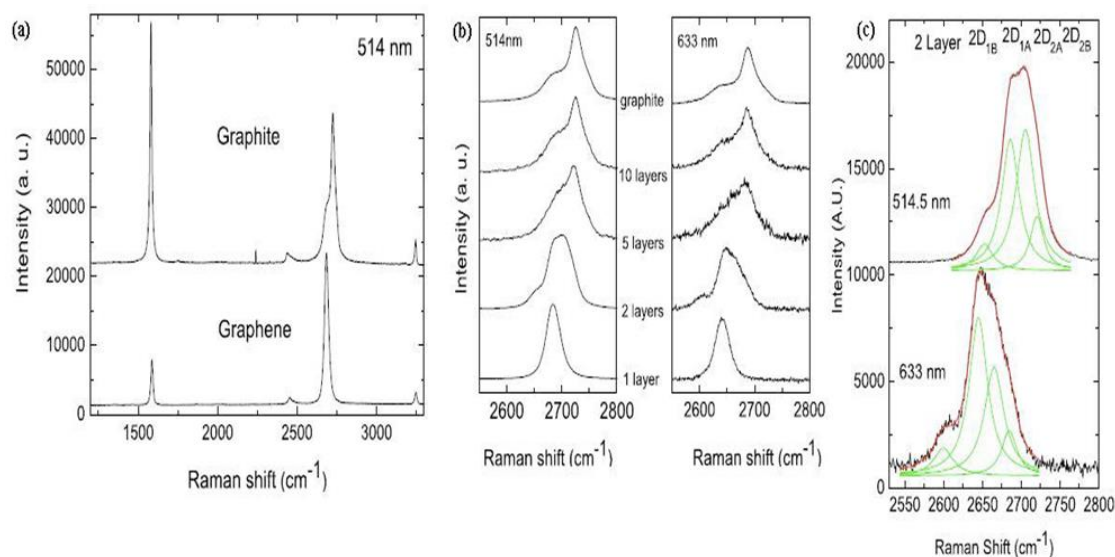


**Figure 3.3 (a) Raman spectra (514 nm) for bulk graphite and single layer graphene, (b) Evolution of graphene Raman spectra, 514 nm (left) and 633 nm (right), with the number of layers.(From Ref.5)**

### 3.4 X-ray photoelectron spectroscopy

X-ray photoelectron spectroscopy is an established surface analysis technique used to examine the properties of atoms or molecules. Its quantification stems from Einstein's documentation of the photoelectric effect in 1905, and since its early development in the 1960s, has become one of the most effective tools for studying the composition and electronic structure of matter, with Kai Siegbahn awarded the Nobel prize in 1981 for the development of high resolution XPS<sup>6</sup>.

The underlying principle of XPS is the photoelectric effect, which arises when monochromatic photons from an X-ray source bombards a surface, producing photoelectrons of discrete energy which distinguish the chemical to make up of the surface. The identifier of interest is the absorption of a photon with quantum energy  $h\nu$  and the ejection of an electron with a specific kinetic energy related to the binding energy of an electron in the target atom (shown in Fig 3.4) The binding energy is the energy acquired from the photon (dependent on the frequency of the photon) that is greater than the work function of the material. It is unique for varying elements and can be used to identify relative composition of constituents in the surface region of samples<sup>7,8</sup>.

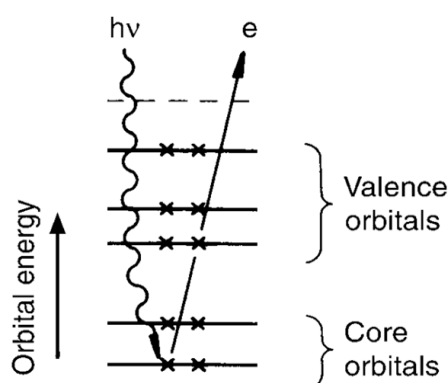


Figure 3.3: XPS basic phenomenon<sup>7</sup>

In XPS only electrons situated near the top of the surface of the matter can escape without loss of kinetic energy due to high probability of inelastic scattering inside the solid<sup>9</sup>. Thus is ideal for studying interfaces and exclusive surface coverage necessary in the research work.

### 3.5 Impedance spectroscopy

Electrochemical Impedance spectroscopy (EIS) is an important technique used for investigating the electric and dielectric properties of ionic, electronic or mixed conductor ceramic materials<sup>10</sup>. This method involves measuring the impedance as a function of frequency by applying a sinusoidal input voltage and measuring the output current. The impedance  $Z$  as a function of angular frequency  $\omega$  can be written in the following complex form:

$$Z(\omega) = Z'(\omega) + jZ''(\omega) \quad (3.5.1)$$

$$Z'(\omega) = \sum_{i=1}^n \frac{R_i}{1 + \omega^2 R_i^2 C_i^2} \quad (3.5.2)$$

$$Z''(\omega) = \sum_{i=1}^n \frac{\omega R_i C_i}{1 + \omega^2 R_i^2 C_i^2} \quad (3.5.3)$$

Where  $Z'(\omega)$  is the real part of the impedance, associated to the resistive contribution of the measured sample, whereas  $Z''(\omega)$  is the imaginary part of the impedance associated to the capacitive contribution. The variable  $n$  used in the summation can take integer values between 1 and 3, corresponding to the different types of conduction path: low resistance continuous paths; discontinuous conductive paths separated by insulating barriers and high resistive paths<sup>10</sup>.

By plotting the real part against the imaginary part of the impedance as a function of frequency we get the so-called Cole-Cole plot. The Cole-Cole plot is a very useful tool for determining the conduction mechanism in the material by fitting an equivalent circuit. The

most dielectric simple model consists of a resistor in series with a RC time constant which is associated to a semicircle in the Cole-Cole plot.

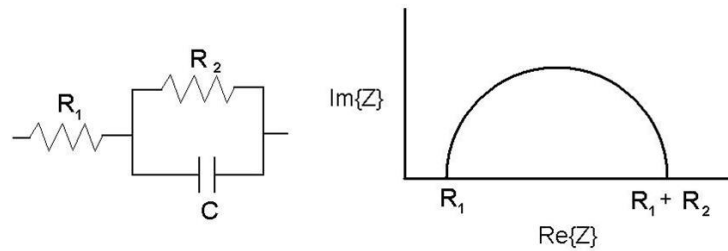


**Figure 3.5 Basic dielectric circuit model with semicircle Cole-Cole plot (From Ref.10)**

### 3.6 Hall effect measurement

#### 3.6.1 Hall effect

One of the most commonly used methods to determine the carrier concentration and carrier type in a semiconductor is the Hall effect<sup>11</sup>. The basic setup is illustrated in Fig 3.6. An electric field is applied along the x-axis and a magnetic field is applied along the z-axis. For simplicity we consider the semiconductor to be p-type. As a consequence of the magnetic field, the Lorentz force  $F_L = q(\mathbf{v} \times \mathbf{B})$  will exert an average upward force on the carriers drifting along the x direction. This will result in an accumulation of holes at the top of the sample, giving rise to a built in electric field  $E_y$  that must balance the Lorentz force as there is no net current along the y-axis in the steady state.

The establishment of the electric field is known as the Hall effect. This field can be related in our measurements in terms of the terminal voltage, or Hall voltage:  $V_H = E_y \omega$ . The Hall field  $E_y$  is proportional to the current density and applied magnetic field  $E_y = R_H J B_z$ . The proportionality constant  $R_H$  is known as the Hall coefficient:  $R_H = 1/qp$  and  $R_H = -1/qn$  for a p- and n-type semiconductor. Therefore from the sign and magnitude of the Hall coefficient the carrier type and carrier concentration can be calculated using the equation<sup>11</sup>

$$p = \frac{1}{qR_H} = \frac{IB_z W}{qV_H A} \quad (3.6.1)$$

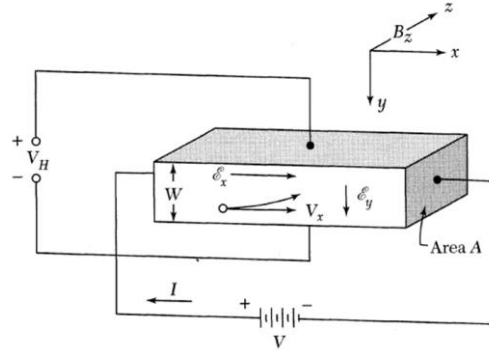


**Figure 3.6 Basic set up to measure carrier concentration using the Hall effect (From Ref.11)**

Having calculated the carrier density we can further determine the carrier mobility using the relationship

$$S = q(nm_n + pm_p) \quad (3.6.2)$$

where  $\sigma$  is conductivity and  $n/p$  is the carrier concentration. For a dominant type of carrier transport we can approximate it to  $S = qnm$ , to calculate the Hall mobility

$$\mu = \frac{\sigma}{qn} = R_H \sigma. \quad (3.6.3)$$

### 3.6.2 Van der Pauw technique

As previously shown, to calculate the Hall mobility we need to calculate the resistivity of our sample. One commonly used method to calculate the resistivity is the four probes van der Pauw technique developed by L.J.van der Pauw<sup>12</sup>. This is an advantageous method that allows to avoid problems due to incorrect knowledge of sample geometry. This technique was specially developed to measure the resistivity of thin flat semiconducting samples, reason why this is appealing for our graphene devices.

This measurement proves to be reliable, with an uncertainty less than 5%, provided that the contacts are on the edge of the sample, have negligible dimensions (point-like); the sample is homogeneous in thickness and the surface is connected, i.e. the samples has no isolated holes.

An example for a four point van der Pauw measurement is shown schematically in Fig 3.7. If these requirements are fulfilled, the following relation has been shown to hold<sup>12</sup>:

$$\exp\left(-\pi \frac{R_{AB,CD}d}{\rho}\right) + \exp\left(-\pi \frac{R_{BC,DA}d}{\rho}\right) = 1 \quad (3.6.4)$$

where  $R_{AB,CD}=(V_D- V_C)/I_{AB}$  and we can write the sheet resistivity in the form

$$r = \frac{\rho d}{\ln 2} \frac{R_{AB,CD} + R_{BC,DA}}{2} \quad (3.6.5)$$

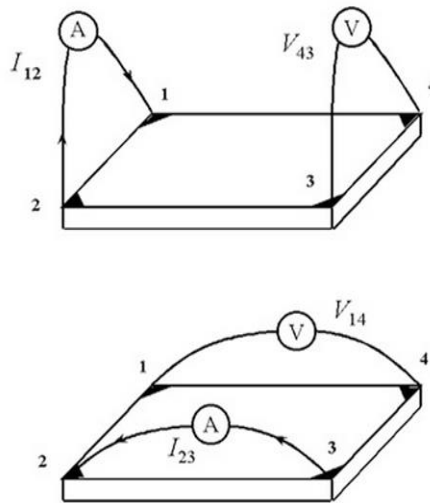


**Figure 3.7 Van der Pauw resistivity measurements**

### 3.7 Ultraviolet-visible spectroscopy

When radiation of a continuous nature interacts with matter a number of processes can occur from reflection, scattering to absorbance and fluorescence. If absorbance occurs the residual radiation, when subjected to a prism yields a spectrum with gaps in it, called an absorption spectrum<sup>13</sup>. The absorption causes atoms or molecules from a lower ground state to excite to a state of higher energy. In UV spectroscopy this transition is between electronic energy levels, usually from the highest occupied molecular orbital (HOMO) to the lowest unoccupied molecular orbital (LUMO)<sup>14</sup>.

From this absorption spectrum, the band gap, which is the energy difference between the top of the valence band and the bottom of the conduction band. To calculate the band gap from

the absorption, you take the cut-off measurement to find the wavelength and use the following formula,

$$E = \frac{hc}{\lambda} \quad (3.7.1)$$

where h is Planck's constant, c is the speed of light and  $\lambda$  is the wavelength.

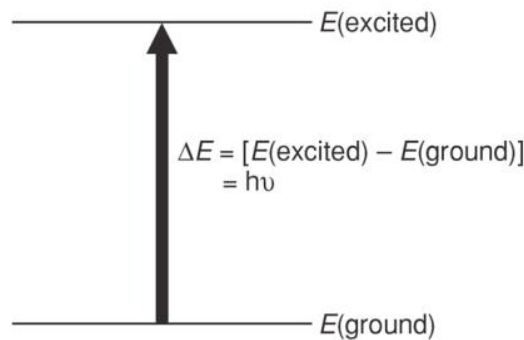


**Figure 3.8 Excitation process from ground to excited state**

### **3.8 Reactive-ion etcher (RIE)**

Reactive-ion etching is a dry etching technology using chemically reactive plasma to remove material deposited on wafer and deposit DLC. RIE includes a vacuum chamber, cooling substrate holder, RF generator of 13.56 MHz, power supplier, shown in Fig 3.9<sup>15</sup>. RIE is a chemical etching, not a physical etching, which means a chemical reaction takes place between the solid atom and gas atoms to etch surface and add gas atom chemical bond<sup>16</sup>.

The main steps in the etching process are:

- 1) Formation of the reactive particle
- 2) Arrival of the reactive particle at the surface to be etched
- 3) Adsorption of the reactive particle at the surface
- 4) Chemisorption of the reactive particle at the surface, i.e. a chemical bond is formed
- 5) Formation of the product molecule
- 6) Desorption of the product molecule

7) Removal of the product molecule from the reactor

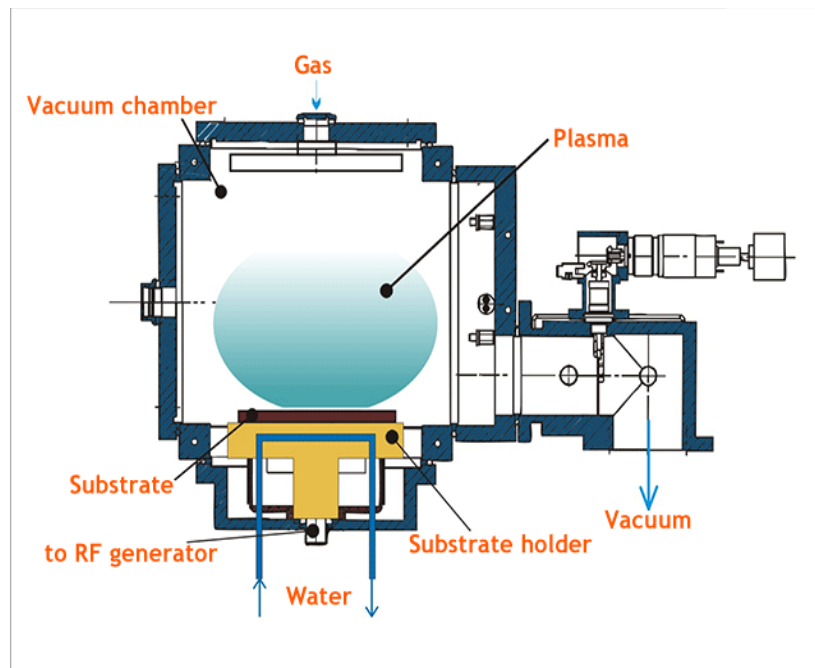


**Figure 3.9 Reactive-ion etcher scheme (From Ref.15)**

In order to terminate diamond surface by  $N_2$  and  $SF_6$ , STS RIE was applied with the following parameters: RF power 500W, 1mTorr, 40s, 20 sccm for  $N_2/SF_6$ . DLC deposition applied Oxford Pro NGP80 with the recipe in Table 3.1. The deposition rate is 49nm/min.

**Table 3.1 DLC deposition recipe**

Step 1	Step 2	Step 3	Step 4
Ar sputter	Cool down step	Gas stabilisation	DLC Deposition
Ar50sccm	Time:5 Minutes	$CH_4$ 100sccm	$CH_4$ 100sccm
RF Power 200W		Pressure 200mTorr	RF Power 350W
Pressure 15mTorr		Time: 30s	Pressure 200mTorr
DC Bias 554V			DC Bias 385V
Time: 10min			

### 3.9 Focused ion beam

The basic FIB instrument consists of a vacuum system and chamber, a liquid metal ion source, an ion column, a sample stage, detectors, gas delivery system, and a computer to run the complete instrument as shown in Fig 3.10. The most common FIB is a FIB/SEM dual platform instrument. A dual-beam system allows sample preparation, imaging, and analysis to be accomplished in one tool. The ion beam and the electron beam complement each other in charge reduction, protective deposition, and imaging, which the electron beam can be used to monitor the ion beam milling to endpoint on the feature of interest<sup>17</sup>. Gallium is currently the most used ion source for FIB because of its low melting point, low volatility, low vapour pressure, and excellent mechanical, electrical, vacuum properties<sup>17</sup>.

The electron beam can be used for imaging without concern of sputtering the sample surface. Electron beam deposition of materials can be applied to produce very low energy deposition. The ability to mill, image, and deposit material using a FIB instrument depends critically on the nature of the ion beam-solid interactions. The response of a given target material to the ion beam is strongly dependent on factors such as beam current, incident ion energy, feature geometry, and milling angle.

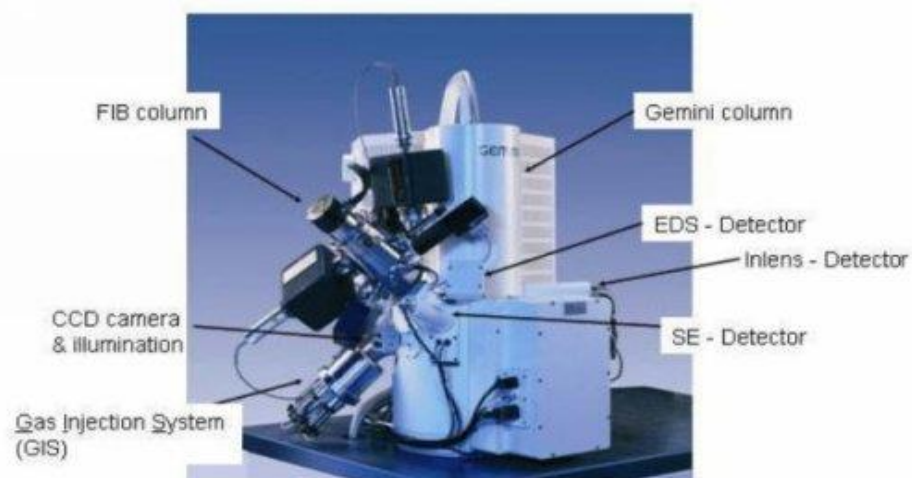


**Figure 3.10 Focused ion beam Microscopy**

## **3.10 Device processing**

### **3.10.1 Overview**

This section briefly goes through the processing steps required to prepare graphene-diamond and graphene-DLC heterostructures. The diamond platforms used were single crystal diamond and detonation nanodiamond thin films. The methods that were used in patterning surface functional groups on the as prepared diamond and DLC samples are described as well, with detailed treatment parameters such as temperature, pressure, gas flow, plasma power and so on. After preparation of substrate samples, graphene transfer process is described.

### **3.10.2 Preparation of diamond samples**

#### **3.10.2.1 Single crystal diamond**

Single crystal diamond (SCD) was provided from Element Six. Firstly, diamond samples are cleaned by acid-bath. The processes are:

1. The ETCHING solution must be prepared in the reaction flask according to the following procedure only: measure 30ml concentrated Sulphuric Acid ( $\text{H}_2\text{SO}_4$ ) into the reaction flask; add 6 teaspoons of Ammonium Persulphate ( $(\text{NH}_4)_2\text{S}_2\text{O}_8$ ) to create a saturated solution at room temperature; place the reaction flask on the heating plate and wait until the plate is at  $100^\circ\text{C}$
2. Once the heating plate has reached  $100^\circ\text{C}$ , drop the samples into the flask
3. Turn temperature of the heating plate to  $200^\circ\text{C}$  and begin a 20 minute countdown.
4. The RINSE solution must be prepared and used at room temperature according to the following procedure only: measure 10ml Hydrogen Peroxide ( $\text{H}_2\text{O}_2$ ) into a glass dish; add 10ml Ammonium Hydroxide ( $\text{NH}_4\text{OH}$ ).

5. Following a 20 minute etch allow the solution to cool to  $\sim 50^{\circ}\text{C}$  and then transfer the diamond samples to the RINSE solution using tweezers for 10 minutes.
6. Following a 10 minute exposure to the RINSE solution the diamond samples should be removed and washed with de-ionised water and blow dried with nitrogen.

After cleaning, the SCD surface was already oxygen terminated. Hydrogen termination was performed using a Seki plasma enhanced chemical vapour deposition (PECVD) system, where the setup is illustrated in Fig 3.11. The chamber was initially pumped down to vacuum level  $\sim 10^{-7}$  Torr. The plasma was ignited at a hydrogen flow of 200scm, pressure of 5 Torr and plasma power 400W. After ignition, the plasma power and chamber pressure were increased accordingly with the final parameters: plasma power 1100W, chamber pressure 50 Torr, hydrogen flow rate of 200 sccm, and temperature  $7\text{-}800^{\circ}\text{C}$ , with a processing time of 20 min. Nitrogen and Fluorine termination were processed by STS-RIE. Fluorination: (500W, 1 mTorr, 40s, source gas,  $\text{SF}_6$  20 sccm) and nitrogenation (500W, 1 mTorr, 40s, source gas,  $\text{N}_2$  20 sccm)



**Figure 3.11 Seki technotron PECVD setup**

### 3.10.2.2 Detonation nanodiamond

Detonation nanodiamond thin films were fabricated by depositing ND on SiO<sub>2</sub>/Si. SiO<sub>2</sub>/Si substrates were cleaned with acetone, Isopropyl alcohol and deionized (DI) water, then dried with nitrogen. The ND solution was prepared by mixing ND powder with DI water with a concentration ratio of 1:14. The substrates were placed in the ND solution for 15 min in an ultrasonic tank.

Hydrogen surface terminations were patterned on the ND films using a high temperature hydrogen thermal treatment process. The setup is illustrated in Fig 3.12. The chamber where the samples were kept was initially pumped down to vacuum level  $\sim 10^{-7}$  Torr before starting the annealing process. The hydrogen termination was done at 500°C, maintaining a pressure of 10 Torr with a H<sub>2</sub> flow rate of 200 sccm, for 5 hours. AFM was applied to determine the surface roughness and thickness which films would be a suitable substrate for graphene.



**Figure 3.12 High temperature nanodiamond hydrogen termination setup**

### **3.10.3 CVD graphene**

#### **3.10.3.1 Growth process**

When it was first experimentally discovered, graphene was produced by exfoliating graphite, producing the best quality graphene. However, this is not a scalable method, the films being limited to small areas, and would therefore not make it a viable solution for industry. Large area graphene synthesis has been developed a chemical vapour deposition (CVD) process on catalytic metal substrates<sup>18</sup>. Copper (Cu) is an excellent candidate for making large-area, uniform thickness (95%), single-layer graphene films due to the low solubility of C in Cu<sup>18</sup>.

Graphene films were primarily grown on 25µm thick Cu foils. A typical growth process flow is<sup>19</sup>:

- (1) Load the fused silica tube with the Cu foil, evacuate, back fill with hydrogen, heat to 1000°C and maintain a H<sub>2</sub> pressure of 40 mTorr under a 2 sccm flow.
- (2) Stabilize the Cu film at the desired temperatures, up to 1000°C, and introduce 35 sccm of CH<sub>4</sub> for a desired period of time at a total pressure of 500 mTorr.
- (3) After exposure to CH<sub>4</sub>, the chamber was cooled to room temperature. The cooling rate was varied from >300 °C/min to about 40 °C/min which resulted in films with no discernable differences.

As the purpose of my research is to manipulate and not grow CVD graphene, further detail is left for the reader to pursue.

#### **3.10.3.2 Graphene transfer**

As grown CVD graphene in Cu foil was spin coated (3000 RPM, 1 min) with polymethylmethacrylate (PMMA), which was then cured at 180°C for 90s. The Cu substrate was etched away using an aqueous solution of iron nitrate Fe(NO<sub>3</sub>)<sub>3</sub> overnight for a period of 12 hours.

The remaining PMMA/graphene layer was rinsed twice and transferred to the target substrates using a “fishing” method. However, this old method was found to cause cracks and tears in graphene layer. An improved method was developed by Li *et al*<sup>20</sup>, which was applied in my research work as well. The schematic diagram is shown in Fig 3.13. After placing graphene on target substrates, redeposit PMMA (3000 RPM, 1min), which would partially or fully dissolve the pre-coated PMMA. The redissolution of the PMMA was to shown mechanically relax the underlying graphene which improved the contact with the substrate<sup>20</sup>. The new PMMA coating cured in air without heater was dissolved by acetone, then rinsed by IPA and DI water.

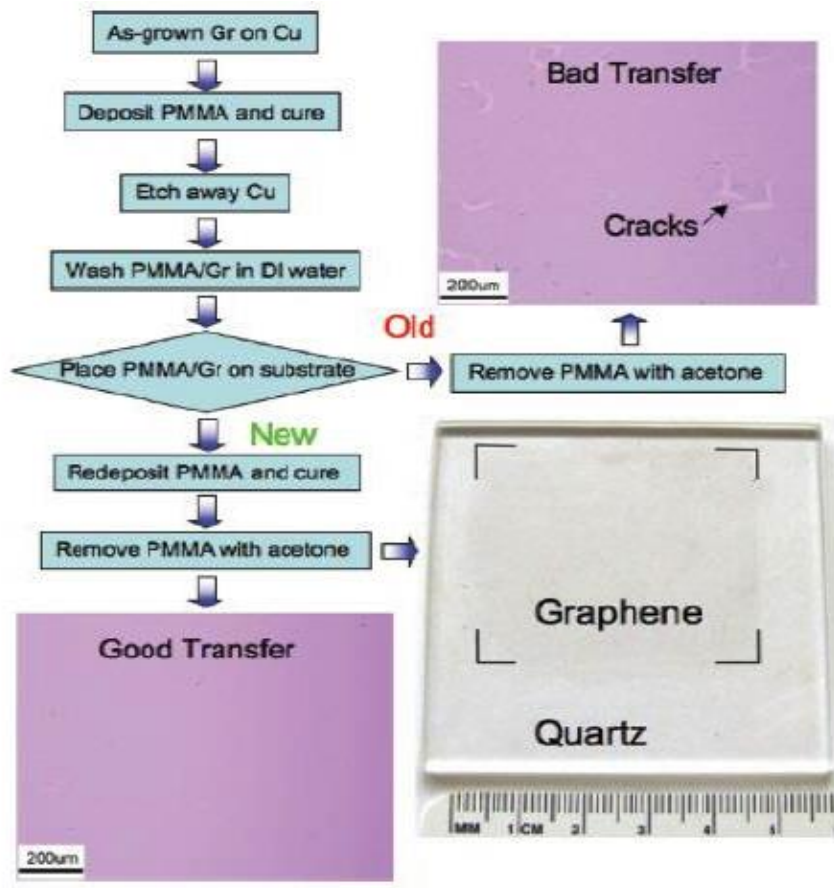


Figure 3.13 Process for transfer of graphene films (From Ref.20)

## Reference

1. Eaton, P. & West, P. Atomic Force Microscopy. (2010).
2. Victor Bellitto, editor. Atomic Force Microscopy - Imaging, Measuring and Manipulating Surfaces at the Atomic Scale. InTech, Janeza Trdine 9, 51000 Rijeka, Croatia, 1st edition, (2012)
3. Princeton Instruments: Raman Spectroscopy Basics; source: <http://content.piacton.com>
4. Hodkiewicz, J. , Characterizing Carbon Materials with Raman Spectroscopy, Thermo Fisher Scientific, Madison, WI, USA
5. A. C. Ferrari et al., Raman Spectrum of Graphene and Graphene Layers, Phys. Rev. Lett. 97, 187401 (2006).
6. C. S. Fadley. X-ray photoelectron spectroscopy: Progress and perspectives. JOURNAL OF ELECTRON SPECTROSCOPY AND RELATED PHENOMENA, 178
7. J. Michael Hollas. Modern Spectroscopy. Wiley, 2004.
8. Leonard C. Feldman Terry L. Alford and James W. Mayer. Fundamentals of Nanoscale Film Analysis. Springer, 2007.
9. Charles C. Chusuei and D. Wayne Goodman. Encyclopedia of Physical Science and Technology. Elsevier Science, 2001.
10. Impedance Spectroscopy Theory, Experiment, and Applications, edited by E. Barsoukov and J. R. Macdonald (Wiley-Interscience, 1992).
11. S.M. Sze Physics of Semiconductor Devices Wiley-Interscience 1969
12. L.J. van der Pauw, Philips Res. Repts 13, 1 (1958); L.J. van der Pauw, Philips Tech. Rev 20, 220 (1958).
13. Kriz Vyvyan Pavia, Lampman. Introduction to Spectroscopy. Brooks/Cole, 4<sup>th</sup> edition, 2009.
14. Mark A. Dubinskii Prabhakar Misra, editor. Ultraviolet Spectroscopy and UV lasers. Marcel Dekker, 2002.
15. RIE scheme. Retrieved from <http://www.made-in-zelengrad.com/product/>
16. Li, L. et al. Reactive ion etching: Optimized diamond membrane fabrication for transmission electron microscopy. J. Vac. Sci. Technol. B Microelectron. Nanom. Struct. 31, 06FF01 (2013)
17. Lucille A. Giannuzzi. Introduction to Focused Ion Beams: Instrumentation Theory, Techniques and Practice. 2006.
18. Muñoz, R. & Gómez-Aleixandre, C. Review of CVD Synthesis of Graphene. Chem. Vap. Depos. 19, 297–322 (2013).
19. Li, X. et al. Large-area synthesis of high-quality and uniform graphene films on copper foils. Science 324, 1312–4 (2009).

20. Li, X. et al. Transfer of large-area graphene films for high-performance transparent conductive electrodes. *Nano Lett.* 9, 4359–63 (2009).

# Chapter 4

## Electronic Properties of Graphene-Single Crystal Diamond Heterostructures

### 4.1 Introduction

In this chapter we describe the carrier transport properties, as judged by Hall effect measurements, of graphene-SCD heterostructures, where the surface termination of the SCD onto which the graphene is attached is varied (-H, -O, -N, -F). Significant variation is observed which is discussed in terms of the nature of the chemical doping of the graphene occurring.

### 4.2 Experimental methods

Single crystal substrates with (100) orientation, 4mm x 4mm x 0.5mm grown by CVD methods were used throughout (Element Six Ltd). Prior to use, substrates were cleaned in strongly oxidising solutions to remove any residual surface conductivity due to organic contaminants and/or adsorbate-hydrogenated surface complexes<sup>1,2</sup>. The acid bath for diamond was given in Chapter 3. All the samples after the acid bath were oxygen terminated. To produce hydrogenated surfaces, SCD samples were exposed to hydrogen microwave plasma (20 mbar, 800C, 10 mins, Seki Technotron AX5010). RF plasma processing of samples (STS PRO ICP RIE) was used (500W, 1 mTorr, 40s) for fluorination (source gas, SF<sub>6</sub> 20 sccm) and nitrogenation (source gas, N<sub>2</sub> 20 sccm). Thermally grown 200nm thick SiO<sub>2</sub> layers on Si were used for control experiments. Contact angle measurements (DSA 10 Mk2) were on the basis on that a drop of DI water meets the solid to get different contact

angles due to the wettability on different substrates. X-ray photoelectron spectroscopy (XPS) was performed to determine the surface coverage of the terminating groups (Loughborough Materials Characterisation Centre). CasaXPS software was utilized to analyse XPS results. Graphene samples (single layer, grown by CVD on Cu foil) supplied by Graphene Supermarket were used throughout and transferred onto the SCD substrate. The large-area graphene grown on Cu foils by chemical vapor deposition was coated by PMMA and an  $\text{FeCl}_3$  solution used to etch the copper. Graphene was then transferred onto substrates, with acetone being used to remove the PMMA. Raman measurements were performed using a Renishaw Invia Raman Microscope system at two different wavelengths (514 and 786nm).

Hall effect measurements were performed to determine carrier densities and mobilities within the heterostructures. A Lakeshore Cryogenics System (1T electromagnet) was used to determine sheet resistance and carrier densities using the ‘van der Pauw’ approach, where-by four ohmic-like metal contacts (10nm Ti - 200nm Au) were placed on the top side of the graphene layer, in the four corners of square samples. Measurements were performed in a He atmosphere for the cryogenic system. The sheet resistance and sheet carrier mobility determined at temperatures between 20K and 298K, using a cryostat controlled sample mount system, and between 298K and 500K using a sample mount system with an integral heater.

### **4.3 Results**

The C 1s region of XPS spectra measured for SCD samples exposed to the four different termination approaches are shown in Fig. 4.1, with the  $\text{sp}^3$  diamond C-C peak used for calibration at a binding energy  $285\text{eV}$ . Fig 4.1(a) shows the survey scans, which shows elements present in different terminated samples. These were taken for all the samples to

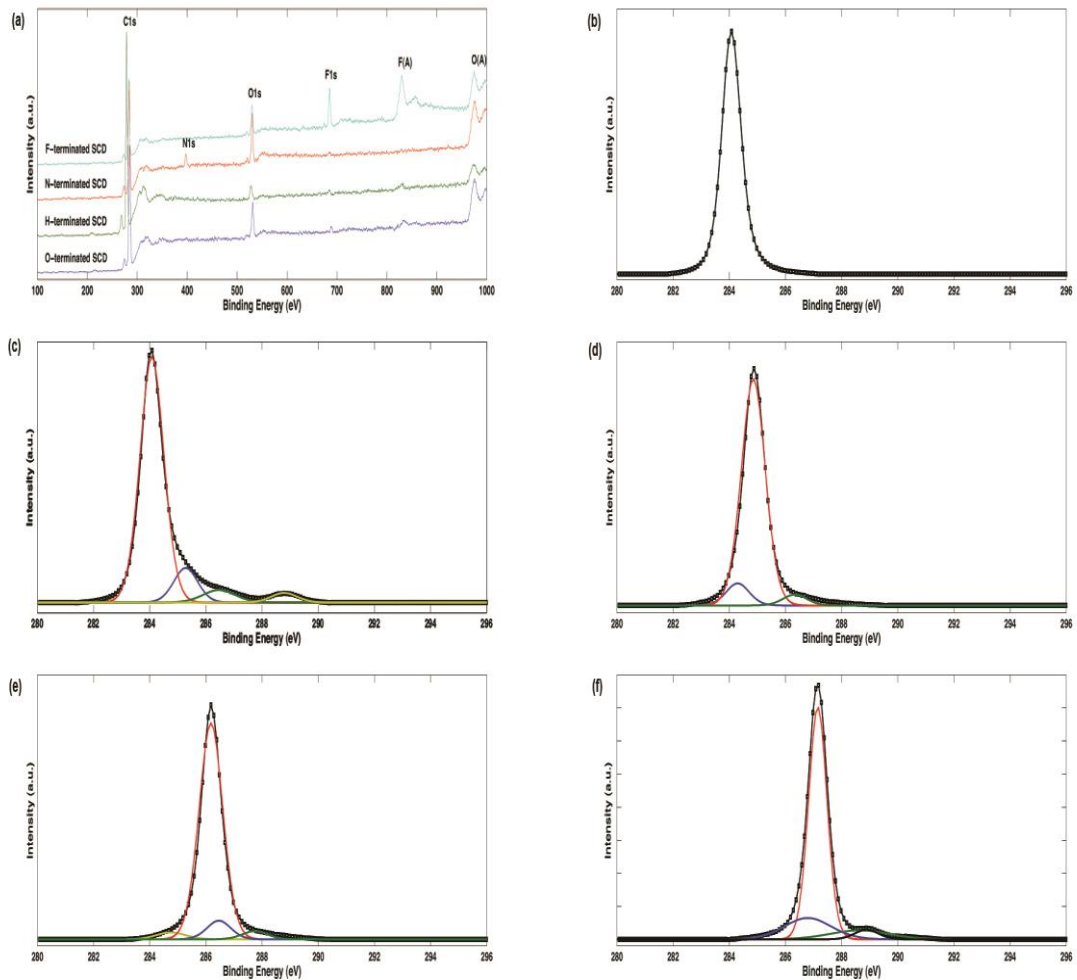


**Figure 4.1 XPS C1s spectra for different substrates (a) Survey scan of different terminated SCD; (b) Graphene on H-, O-, N- and F-terminated SCD (scans are overlap for different termination);(c) Hydrogen terminated SCD; (d) Oxygen terminated SCD; (e) Nitrogen terminated SCD; (f) Fluorine terminated SCD. (black line is fitted curve)**

individual elemental scans (C1s, O1s, N1s, F1s). The detected elements are labeled as shown.

Fig 4.1 (b)-(f) are C1s scan for different SCD (100) samples. Fig 4.1(b) is C1s scan for graphene on different terminated diamond samples, which are same for different diamond substrates because XPS machine is much sensitive for surface to check a 4nm layer. Only one peak was at a binding energy 284eV from graphene. Fig 4.1(c) shows hydrogenated surface at a binding energy 284eV for C-H, where peaks fitting reveal additional state at 285.2eV, 286.2eV, and 289.2eV. Whilst for surfaces expected to be oxygen terminated, main peak is at binding energy 285eV, the additional peaks are one at lower energies of ~284.2eV

and another one at 286.4eV. Due to nitrogen termination and fluorine termination, the main peaks are at different binding energy, 286eV for N-terminated SCD and 287eV for F-terminated SCD, with same C-N and C-F weak peaks. The use of wide-scan XPS spectra enables the primary elements present to be identified, and these are listed in Table 4.1. It is clear that some oxygen remains present on the various samples, although it is minimized in the case of the hydrogenated substrates. Contact-angle experiments were performed on each sample type to investigate the hydrophobicity of each; Table 4.2 shows the results achieved. With an angle of around 90°, the H-terminated and F-terminated samples appear strongly hydrophobic, whilst the other surfaces, at around 57°, rather hydrophilic.

Raman measurements recorded following the deposition of graphene onto these types of substrates are shown in Fig 4.2(a); it is apparent that the peak at 1332cm<sup>-1</sup>, which can be attributed to diamond<sup>4</sup> dominates the spectrum in each case. The data in Fig. 4.2(a) inset is presented the high resolution from 1400cm<sup>-1</sup> to 1800cm<sup>-1</sup>, omitting the diamond1332cm<sup>-1</sup> region, such that the so-called G peak of the non-diamond carbons present can be seen, which is same for graphene on the different diamond substrates.

**Table 4.1 Elemental compositions calculated from XPS spectra for the single crystal (100) diamond substrates, following exposure to different surface termination treatments.**

Sample	C	N	O	F
H-terminated SCD	97%		3%	
O-terminated SCD	90%		10%	
N-terminated SCD	82%	6%	12%	
F-terminated SCD	78%		12%	10%

**Table 4.2 Contact wetting angles for each of the sample types**

Substrate	Contact Angle
Hydrogen terminated SCD	89°
Oxygen terminated SCD	57°
Nitrogen terminated SCD	58°
Fluoride terminated SCD	93°

For comparison, Fig. 4.2(b) shows the Raman spectrum obtained for the same graphene material processed in a similar manner but deposited on a thermal SiO<sub>2</sub> layer. Graphene has a single and very sharp 2D peak, which means graphene is present as a monolayer<sup>4</sup>. A full range of peaks attributable to differing carbon vibrations can now be seen. The samples were next subjected to electrical evaluation using Hall effect measurements. Room temperature (298K) measurements for the sheet resistivity, sheet carrier concentration and the calculated carrier mobility values are shown in table 4.3. In each case the sign of the measured Hall voltage indicated samples to be p-type in character. Very different values can be seen for each sample type, with mobilities ranging from 1 to 221cm<sup>2</sup>/Vs and carrier concentrations in the range 6 x 10<sup>12</sup> cm<sup>-2</sup> to 5 x 10<sup>14</sup> cm<sup>-2</sup>. Fig 4.3(a) shows the mobility values for each sample type plotted against the corresponding sheet carrier concentration; the lack of a clear trend is quite apparent. In the case of the highest mobility sample type, graphene on H-terminated SCD, Hall measurements were performed over a wide temperature range. The mobility value peaked at ~250cm<sup>2</sup>/Vs at around 170K, the temperature at which the sheet carrier concentration minimized before increasing again at lower temperatures, with a decrease in mobility to around 150cm<sup>2</sup>/Vs. Fig 4.3, shows the sheet carrier concentration and mobility values at high temperatures, (a) and (b).

## 4.4 Discussion

Whilst the terminology H-, O-, F- and N-terminations for the SCD has been used, it is clear from the data contained in table I, that all samples support some surface O-groups to lesser or greater presumably because the initial strong acid bath cleaning step creates oxidised SCD, which is not entirely displaced by the subsequent treatments. Indeed, the F- and N- samples are in fact F/O- and N/O- terminated, which produced a concentration of about 5.4% N and 9.5% F, together with a small increase in oxygen content compared with O-termination sample. Only in the case of the H- terminated surfaces is the O content relatively low at 3%. In this case adsorbed Hydrogen can displace C-O-C and carbonyl groups to create dangling bonds<sup>5</sup>. A -1 eV shift of C1s peak from 285eV is assigned to carbon bonded to surface

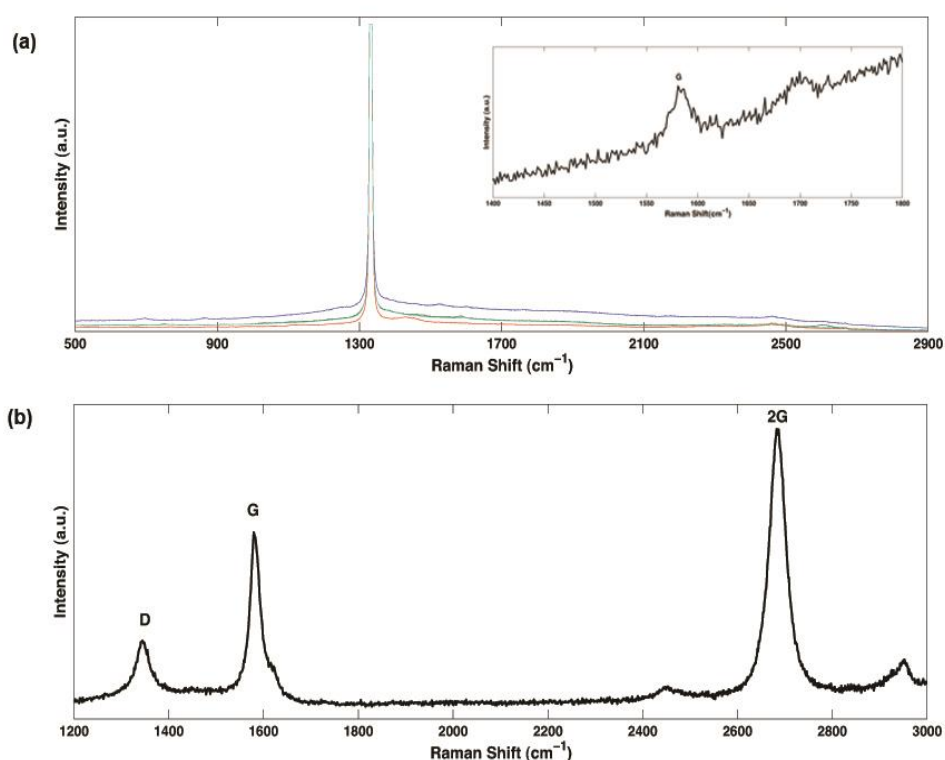


**Figure 4.2 (a) Raman spectra of graphene on diamond (100) subjected to the various treatments (blue line for GHSCD, green line for GOSCD, red line for GNSCD and GFSCD), ; inset (a) Raman spectra of graphene on diamond (100) subjected to the various treatments, revealing the G peak at 1580cm<sup>-1</sup>; (c) Raman spectrum of similar graphene on SiO<sub>2</sub>-Si.**

hydrogen. After transferring graphene onto SCD (cleaned by strong acid), the content of oxygen is higher than the content on O-terminated SCD. This can be explained by carbonyl bonding on the diamond and a bridge oxygen of C-O-C between graphene and diamond<sup>5,6</sup>. From Fig. 4.1 (c)–(f), peak positions are different for different termination due to the C-X functionalization. The following bonds are generally assigned:  $sp^2$  C-C (284.2-284.6eV),  $sp^3$  C-C (285.0-285.5eV), C-O (286.2-287.1eV), C=O (287.1-288.1eV), C-OOH (288.0-289.4eV), C-NH<sub>x</sub> (286-288.5eV), C-N (286.3-286.8eV), C-F (287.0-290.2eV), C-F<sub>2</sub> (291.6-292.4eV), and C-F<sub>3</sub>(292.4-293.4eV)<sup>8,9,10</sup>. On H-terminated SCD there is strong C-OOH peak about 289eV. For O-terminated SCD, C=O and C-O are shown in Fig. 4.1(d). For N-terminated SCD and F-terminated SCD, C-N and C-F functionalization affect different peak positions.

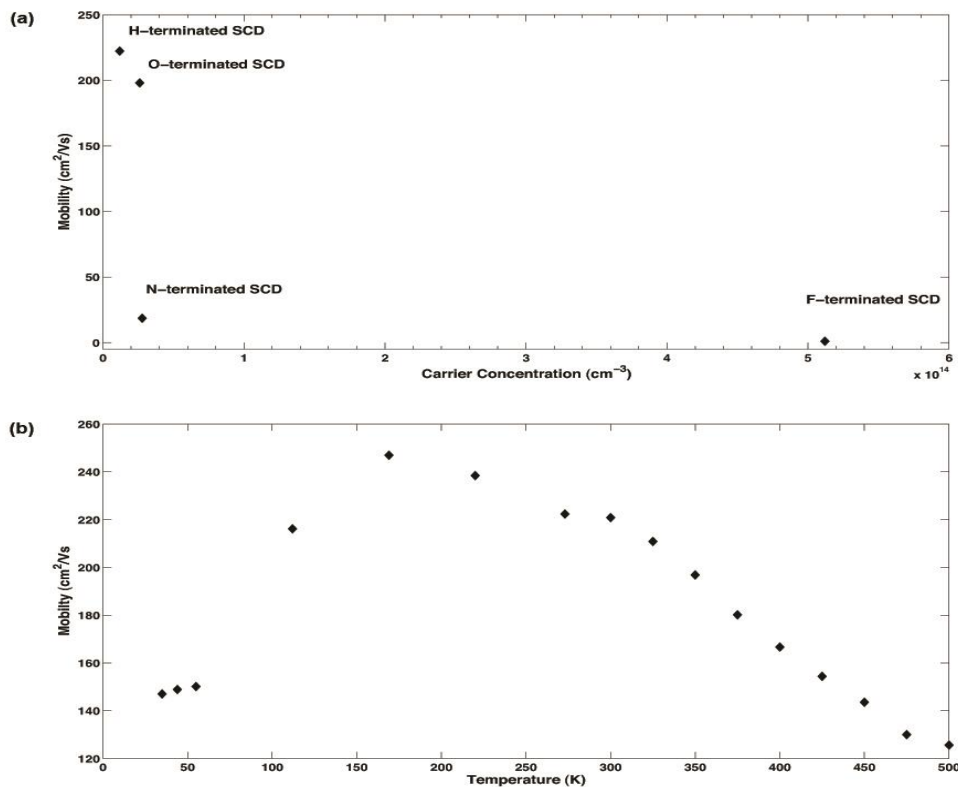


**Figure 4.3 (a) Mobility values for each sample type plotted against the corresponding sheet carrier concentration; (b) Mobility of H-terminated SCD for large temperature range from 35K to 500K**

**Table 4.3 Sheet resistivity, sheet carrier concentration and carrier mobility for the p-type conduction measured at 298K for each sample type, as judged by Hall effect measurements.**

Sample	Temperature (K)	Sheet resistivity (Ohm/sq)	Carrier concentration ( $\times 10^{12} \text{ cm}^{-3}$ )	Mobility ( $\text{cm}^2/\text{Vs}$ )
Graphene on H-SCD	298	4392	6.5	221
Graphene on O-SCD	298	1345	28	196
Graphene on N-SCD	298	12000	24	19
Graphene on F-SCD	298	11716	512	1

Electron mobilities of CVD graphene are an order of magnitude lower than those in exfoliated graphene<sup>10</sup>. Point defects and chemical impurities from substrates affect the mobility of graphene-diamond structure<sup>11</sup>. The mobility of H-terminated SCD at room temperature is the highest because of “surface conductivity” on H-terminated diamond surfaces. In this case, electron transfer from diamond to the  $\text{H}_3\text{O}^+ / (\text{H}_2\text{O} + \text{H}_2)$  redox couple accounts for hole accumulation layer<sup>12</sup>. This p-type layer can then enhance the conductivity that arises directly from the graphene layer. For N(O)- and F(O)- terminated SCD samples, the recorded mobilities are very low, which suggests the interaction between diamond substrates and graphene results in poor electrical properties. However, it should be noted that in the case of Graphene-F(O)-SCD heterostructures the sheet carrier density is extremely high, which, along with modest mobility, is metallic-like behaviour.

From Fig 4.3(b) it can be seen, the mobilities for graphene on H-terminated SCD increase as the temperature from 35K to 170K then drop down from 170K to 500K. With increasing temperature, electron-phonon scattering increases. For low temperature, acoustic phonons interaction dominates; for high temperature, both optical phonons and intervalley scattering increase<sup>13</sup>. Due to acoustic phonon interaction, the mobility is expected to be proportional to  $T^{-3/2}$ ; while the mobility leading by optical phonon scattering is expected to be proportional

to  $T^{-1/2}$ <sup>14</sup>. Ionized impurity scattering can affect mobility as well. The effect of impurity scattering decreases with increasing temperature<sup>15</sup>. From Fig 3, from 35K to 170K, the slope is about 9/20; from 170K to 475K, the slope is -9/10. So at low temperature, it can be suggested that ionized impurity scattering dominates, whilst at higher temperature, electron-phonon scattering dominates.

Conductivity,  $\sigma$ , is characteristically a function of temperature, which can be described by an exponential function<sup>16</sup>

$$S = S_0 \cdot \exp\left(-\frac{E_g}{2kT}\right) \quad (4.1)$$

Where  $E_g$  represents the materials band-gap,  $k$  is Boltzmann's constant and  $T$ , temperature.

The logarithm of the equation

$$\ln S = \ln S_0 - \frac{E_g}{2kT} \quad (4.2)$$

means that a plot of  $\ln \sigma$  against  $1/T$  will yield a line whose slope contains information on the band gap of the material. In the case of graphene-H-SCD heterostructures a value of  $E_g \sim 0.07\text{eV}$  is obtained; this is significant as it shows that a band-gap, essential for the formation of many types of electronic devices can be created locally by H-terminating SCD substrates. So energy gap can be worked out from the slope of the line. Recently, many approaches including defect generation<sup>17</sup>, molecular doping<sup>18</sup>, nano ribbon<sup>19</sup>, and gas adsorption<sup>20</sup> have showed to open the bandgap, such as bilayer graphene and boron doped graphene, whilst these reduce the good mobility of graphene<sup>21,22</sup>. In the current case a simple chemical functionalisation of the SCD substrate is sufficient to offer both p-type graphene with an  $E_g \sim 0.07\text{eV}$  and good mobility, or metallic-like behavior (in terms of free carrier density) with low mobility but very high carrier concentrations. Since it is relatively easy to pattern these functional groups on the diamond surface, these suggests that this approach may offer an

exciting route to 2D device structures on single layer graphene sheets.

#### **4.5 Concluding remarks**

In summary, monolayer CVD Graphene was covered on H-, O-, N(O)- and F(O)- terminated single crystal diamond leading to interesting electronic properties. Whilst the quality of the graphene used here is the likely cause for relatively modest mobility values being measured, Graphene on H-terminated SCD shows highest transport mobility. At  $250 \text{ cm}^2/\text{Vs}$  this is high enough for many device applications. Moreover, this heterostructure gave rise to p-type graphene with a band gap energy of around 0.07eV. In contrast, N(O)- terminated SCD substrates led to extremely high carrier densities and a more metallic-like characteristic. Since it is relatively easy to pattern these functional groups on the diamond surface, these suggests that this approach may offer an exciting route to 2D device structures on single layer graphene sheets.

## Reference

1. B. Baral, S. S. M. Chan, and R. B. Jackman, *J. Vac. Sci. Technol. A*14, 2303 (1996).
2. O. A. Williams and R. B. Jackman, *J. Appl. Phys.* 96, 3742J (2004).
3. J. Filik, P. W. May, S. R. J. Pearce, R. K. Wild, and K. R. Hallam, *Diamond Relat. Mater.* 12, 974 (2003).
4. A. C. Ferrari and J. Robertson, *Philos. Trans. R. Soc. London, Ser. A* 362, 2477 (2004).
5. A. C. Ferrari, *Solid State Commun.* 143, 47 (2007).
6. J. I. B. Wilson, J. S. Walton, and G. Beamson, *Electron Spectrosc. Relat. Phenom.* 121, 183 (2001).
7. T. Yamada, H. Seki, and T. J. Chuang, *Appl. Phys.* 39, 1830 (2000).
8. T. I. T. Okpalugo, P. Papakpstantinou, H. Murphy, and N. M. D. Brown, *Carbon* 43, 153 (2005).
9. E. P. Dillon, C. A. Crouse, and A. R. Barron, *ACS Nano* 2, 156 (2008).
10. See <http://cnx.org/content/m34549/latest/>
11. F. Bonaccorso, A. Lombardo, T. Hasan, Z. Sun, L. Colombo, and A. C. Ferrari, *Mater. Today* 15, 564 (2012).
12. W. C. Shin, S. Seo, and B. J. Cho, *Appl. Phys. Lett.* 98, 153505 (2011).
13. F. Maier, M. Riedel, B. Mantel, J. Ristein, and L. Ley, *Phys. Rev. Lett.* 85, 3472 (2000).
14. W. Gannett, W. Regan, K. Watanabe, T. Taniguchi, M. F. Crommie, and A. Zettl, *Appl. Phys. Lett.* 98, 242105 (2011).
15. E. H. Hwang and S. D. Sarma, *Phys. Rev. B* 77, 115449 (2008).
16. *Solid state Electronic Devices*, edited by B. G. Streetman, 4th ed. (Prentice Hall, New Jersey, 1995).
17. D. W. L. Solymar, *Electrical Properties of Materials* (Oxford University Press, New York, 1998).
18. X. Dong, Y. Shi, Y. Zhao, D. Chen, J. Ye, Y. Yao, F. Gao, Z. Ni, T. Yu, and L. J. Li, *Phys. Rev. Lett.* 102, 135501 (2009).
19. Y. B. Tang, L.-C. Yin, Y. Yang, X.-H. Bo, Y.-L. Cao, H.-E. Wang, and C. S. Lee, *ACS Nano* 6, 1970–1978 (2012).
20. M. Y. Han, B. Ozyilmaz, Y. Zhang, and P. Kim, *Phys. Rev. Lett.* 98, 206805 (2007).
21. S. Y. Zhou, D. A. Siegel, A. V. Fedorov, and A. Lanzara, *Phys. Rev. Lett.* 101, 086402 (2008).
22. Y. Zhang, T.-T. Tang, C. Girit, Z. Hao, M. C. Martin, A. Zettl, M. F. Crommie, and F. Wang, *Nature (London)* 459, 820–823 (2009).

# Chapter 5

## Properties of graphene-diamond-like carbon Heterostructures

### 5.1 Introduction

In this chapter, diamond-like carbon was applied to support the graphene. The family of amorphous carbon films, which exist with varying degrees of  $sp^2$  and  $sp^3$  content, and known as diamond-like carbons (DLCs) may be a preferable alternative, as they can be deposited at room temperature over large areas on a wide range of substrates, and are inexpensive to produce. Indeed, Wu and co-workers have already produced high performance radio-frequency graphene field-effect transistors (FETs) with the graphene being deposited on DLC films owing to higher phonon energy and lower surface trap density of DLC<sup>1</sup>.

DLC is an amorphous hydrogenated carbon (a-C:H) with 20-40% hydrogen content containing a significant fraction of  $sp^3$  bonds, which typically displays high mechanical hardness, optical transparency, low surface energy, wide band gap (2.5-3.5eV) and low friction coefficients<sup>2,3</sup>. DLC films have been widely utilized in recent years as hard coatings with useful optical, thermal and electrical properties. Various terminated DLC films have been developed to change and improve DLC's properties. The additions include nitrogen (NDLC) and fluorine (FDLC). Nitrogen termination enabled to cause the optical band gap to shrink<sup>4</sup>; fluorine banding groups have been presented to reduce DLC's surface energy and

friction coefficients<sup>5,6</sup>. In this chapter, we describe the physical-chemical properties of graphene-DLC/NDLC/FDLC heterostructures and relate them to the observed electronic properties. Significant differences are observed which are discussed in terms of the interaction of graphene with the various DLC coated substrates.

## 5.2 Experimental methods

DLC films were deposited using RF plasma system, normally configured as a reactive ion etching (RIE) instrument (Oxford Plasma Pro NGP80). P-type Si (100) substrates with a 300nm SiO<sub>2</sub> top layer were used as substrates throughout. DLC films were deposited (RF power 350W, CH<sub>4</sub> carbon source gas at a flow rate of 100sccm) for 10 minutes, resulting in around 500nm DLC film thickness. After cleaning DLC films by acetone and IPA, different surface terminations were introduced onto the DLC films using a different RF plasma tool (STS Pro-ICP RIE), (500W, 1mTorr, 1 min) for fluorination (SF<sub>6</sub>, 20sccm) and nitrogenation (N<sub>2</sub>, 20sccm). CVD monolayer graphene on copper foil, supplied by Graphene Supermarket, was used throughout and transferred onto DLC films by a PMMA supported transfer process described in detail elsewhere<sup>7</sup>. The surface morphology of the various films was measured over 2 mm × 2 mm regions by scanning atomic force microscopy (AFM, Veeco Dimension) in tapping mode. The chemical composition and bonding states of the films were characterized using X-ray photoelectron spectroscopy (XPS, Thermo Scientific) with the Al K $\alpha$  line as the exciting source. A micro Raman spectroscopy (Renishaw Invia system) operating at 514.5 nm was used to study the film microstructure, where the laser output power used was 1mW. Hall Effect measurements (1T electromagnet, Lakeshore Cryogenics System) were performed to determine graphene carrier mobilities using “van der Pauw” method, which by four ohmic metal contacts (10nm Ti-200nm Au) were placed on the topside of the graphene layers at room temperature.

### 5.3 Results and Discussion

As judged by AFM, the DLC films deposited were all uniform and smooth. Comparing the as-deposited DLC films ( $R_a \sim 0.45\text{nm}$ , average height  $0.4\text{nm}$ ) to the surface functionalized ones, indicated that the processing had introducing some roughening; the NDLC and FDLC films displaying  $R_a$  values of  $0.46\text{ nm}$  and  $1.48\text{nm}$  respectively (Fig. 5.1), which N-termination does not affect roughness. The roughness increase can be considered to result from localized etching effects, as the films are not expected to be ideally isotropic<sup>8,9</sup>. It is seen from Fig. 5.1 that the fluorine termination leads to clear difference (average height  $1.1\text{nm}$ ) in the morphology which may add more addition atoms to affect cluster structure; whilst the nitrogen atoms do not much affect the surface and the number of dangling bonds<sup>4</sup>. More structure studies would be presented in Raman and XPS analysis.

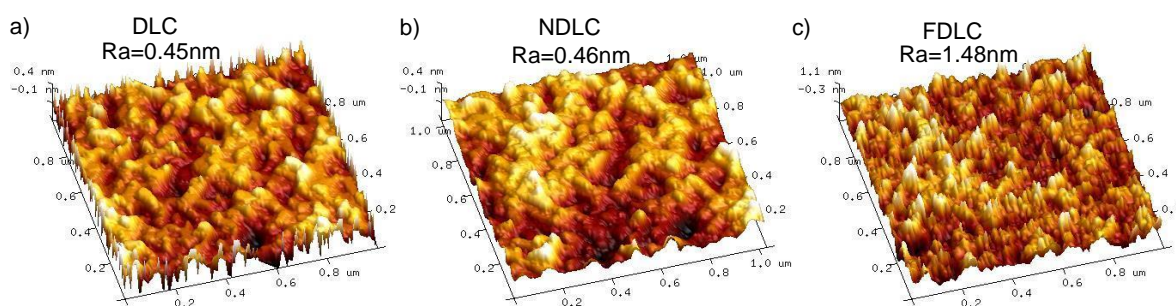


**Figure 5.1. AFM images of different termination DLC film.  $R_a$  is the average surface roughness in nm. (a) DLC. (b) NDLC. (c) FDLC.**

Raman spectroscopy shows many differing features in the  $800\text{-}3000\text{cm}^{-1}$  region, which can be used to consider the nature of the bonding present between the carbons present. In particular, the so-called D, G and 2D peaks, which lie at around  $1360$ ,  $1560$ , and  $2700\text{cm}^{-1}$  have been widely studied. The G peak is due to bond stretching of pairs of  $\text{sp}^2$  atoms in both rings and chains, known as the graphite or tangential band<sup>10</sup>. The D peak is due to the

breathing modes of  $sp^2$  atoms in rings and induced by local basal plane derivatization with  $sp^3$  distortion<sup>10,11</sup>. The 2D peak is the second order of D peak and used as a fingerprint for the presence and quality of graphene layers<sup>12</sup>. The visible Raman spectra of carbon films are dominated by  $sp^2$  sites, because visible excitation always resonated with the  $\rho$  states<sup>12</sup>, even for the highly  $sp^3$  DLC films. The  $sp^3$  component of diamond or samples containing a significant of diamond phase would be expected to give rise to a peak at  $1332\text{cm}^{-1}$ , whose peak width can be taken as an indication of disorder within the  $sp^3$  bonding matrix<sup>22</sup>. Fig. 5.2, plotted by Origin Pro 8.5 with a Voigt function, compares the Raman spectra of DLC films grown here to the films following surface functionalization, and also for DLC with a graphene overlayer. In Fig. 5.2(a) the D and G peaks are clear to be observed, while the  $sp^3$  stretching modes are not clearly evident under visible Raman laser. A typical signature for hydrogenation level in samples measured in the visible region is that photoluminescence background (PL) increases with increasing H content<sup>12</sup>. The ratio between the slope ( $m$ ) of the fitted linear background and the intensity of the G peak ( $I_G$ ) can be used as a measure of the C-bonded H content<sup>10</sup>. In Fig. 5.2 (a), the PL has been measured between  $1000$  and  $1800\text{cm}^{-1}$ . Following the method described by Casiraghi<sup>3</sup>, leads to an estimate for the H content in these films to be  $\sim 25\%$ . Such DLC films are often referred to as a-C:H films. In Fig. 5.2 (a-c), the G and D peaks positions are shifted when compared to typical peak positions of  $1560$  and  $1360\text{cm}^{-1}$ <sup>11</sup>. Such peak shifting or peak dispersion increase with increasing disorder; for visible Raman excitation, increasing  $sp^3$  content in the film and general disordering lead to a reduction in G peak Raman shift<sup>10</sup>. For all of the DLC films studied here, the G and D peaks have such blue-shift, hence increasing levels of disorders. In addition to investigating the peak positions of the G and D peaks, their intensity ratio is also of interest. An increase of  $I_D/I_G$  ratio being ascribed to an increase the size of  $sp^2$  clusters, defects for DLC and the  $sp^3$

hybridization changes due to new C-N or C-F bonds<sup>12</sup>. For the films studied here, DLC, NDLC, and FDLC, the ratios of  $I_D/I_G$  are 0.35, 0.38 and 0.41, respectively, an increase in

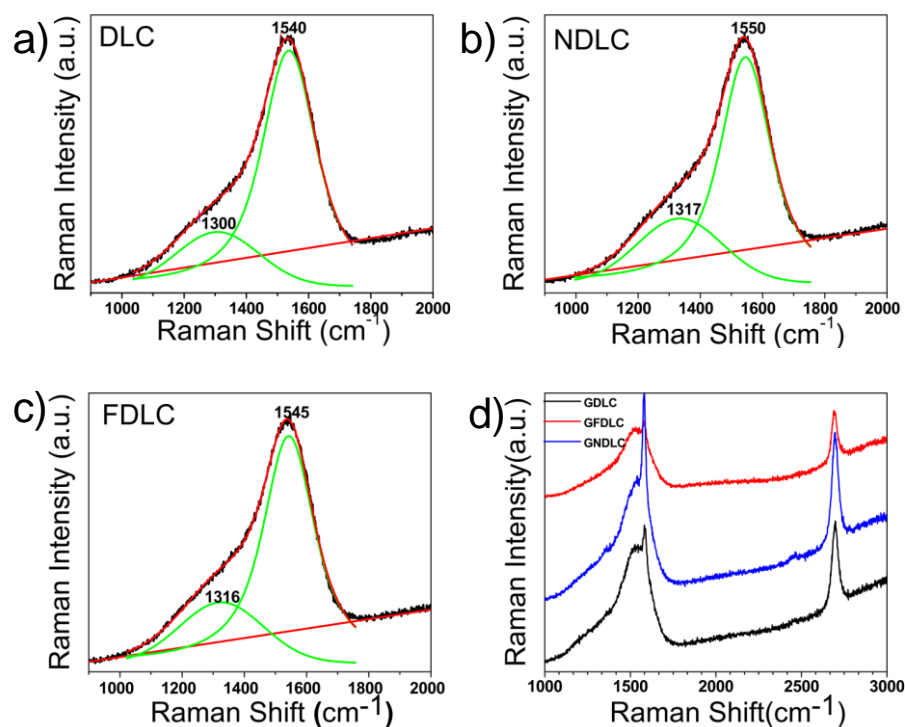


**Figure 5.2 Raman Spectrum of DLC films and graphene-DLC heterostructure films. (a) DLC (Error: D peak 0.5, G peak 0.2). (b) NDLC(Error: D peak 0.5, G peak 0.4). (c) FDLC. (d) graphene on different terminated DLC.**

disorders that correlates to the different AFM roughness values previously measured. After the transfer of CVD graphene, a sharp G peak emerges on top of the broad peak from the DLC, and a sharp 2D peak can also be seen (Fig. 5.2 (d)). The Raman spectrometer laser interacts not just with the graphene surface, but with all the molecular bonds in graphene and DLC films. For graphene, the two most intense features are the G peak at  $1560\text{ cm}^{-1}$  and the 2D peak at  $2700\text{ cm}^{-1}$ <sup>12</sup>. From Fig. 5.2(d), nitrogen additions look like “not” affecting graphene much because Raman results shows clear and strong G and 2D peaks, whilst for F-terminated substrate G and 2D peaks are weaker than no-treated DLC substrate. However, apparent changes of the ratios of  $I_D/I_G$  can be calculated in the case of a graphene-DLC

heterostructures, 0.41, 0.31 and 0.37, respectively for GDLC, GNDLC, and GF DLC. The lower  $I_D/I_G$  ratio accounts to the bigger domain size in graphene<sup>8</sup>. This suggests that defects are possibly induced from the addition bonds between the graphene and DLC films, where we might get a similar transition from C=C  $sp^2$  to a C-C and C-H/N/F  $sp^3$  network<sup>10,13</sup>. A significant evidence of monolayer graphene is shown from the sharp shape of 2D peaks<sup>13</sup>. From Raman results, it has been shown that there are interactions between graphene and C-H/N/F bonds, which enable to change graphene properties.

X-ray photoelectron spectroscopy is a valuable tool to evaluate the changes in the surface composition and bonding that occurred during surface termination<sup>14</sup>. Fig. 5.3 shows the C 1s spectral region XPS for the different DLC film and DLC with graphene overlayers. The C 1s core-level spectra of our samples were fitted by CasaXPS software with the following peaks: 284.5eV binding energy (BE) assigned to  $sp^2$  hybridized C atoms (blue line in Fig. 5.3) in DLC (graphite structure) and graphene; 285.4eV BE assigned to  $sp^3$  hybridized C atoms (red line) due to the formation of C-H and C-C of DLC by different termination; other components with higher BE which originate from C-N/F groups, interface states or contamination<sup>14,15</sup>. Without any additional surface functionalisation, the spectrum (Fig. 5.3(a)) is typical of pure DLC films characterized by BE of carbon in  $sp^2$  and  $sp^3$  bonding configurations, and carbon in a COOH bonding environment at 288.6eV, which accords with the H content (only 25%) of the DLC film from Raman results (much more  $sp^2$  graphite C bonds)<sup>22</sup>. After nitrogen termination, around 7% N was found on the NDLC surface, creating new carbon bonding environments of C-NH and C=O (286.4 and 287.7eV), whilst  $sp^2$  C=C transitioned to  $sp^3$  C-C owing to the band terminations, so the ratio of  $sp^2/sp^3$  decreased compared with no-treatment DLC<sup>14,15</sup>. Fluorine termination leads to a stronger reaction with the DLC films, with FDLC samples having ~24% F on their surfaces. The spectrum in

Fig.5.3 (c) shows six peaks were observed with binding energies of 284.3, 285, 286, 283,290

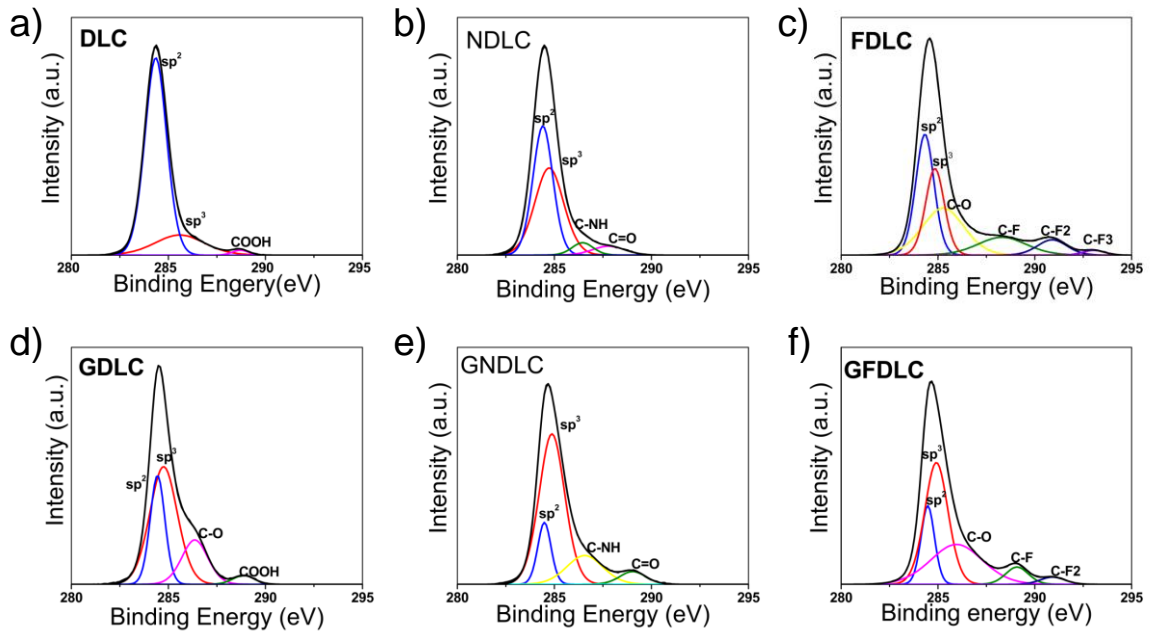


**Figure 5.3 XPS spectrum of DLC films and graphene-different termination DLC heterostructures' films. Blue line for  $sp^2$  and red line for  $sp^3$ . (a) DLC. (b) NDLC. (c) FDLC. (d) graphene on DLC. (e) graphene on NDLC. (f) graphene on FDLC.**

and 293eV, which can be assigned to  $sp^2$ ,  $sp^3$ , C-O, C-F, C-F<sub>2</sub>, and C-F<sub>3</sub> bonds, respectively<sup>6,8,16</sup>. Thus, the apparent presence of C-F<sub>x</sub> groups leads to higher film roughness (AFM observation Fig. 5.1) and the content of  $sp^3$  bonds increase. Bendavid<sup>6</sup> shows more C-F<sub>x</sub> groups accords to the surface energy decrease, so FDLC has lower surface trap density which may become a better support substrate than pure DLC. Furthermore, the content of  $sp^3$  bands is higher than  $sp^2$  bands for graphene with different terminated DLC heterostructures surface. Since the effective sampling depth of XPS is about 2-5nm, here the primary states of  $sp^3$  peaks are assigned by C-H bands of DLC and hybridized C-C formed by C-N/F functional groups, whilst the secondary states of  $sp^2$  peak are influenced by graphene and C=C bands of DLC<sup>6,15</sup>. Stronger  $sp^3$  peaks may be described as those originate from interface states or C-H/N/F groups which reduce a transition from a  $sp^2$  to a  $sp^3$  network<sup>6,15,17</sup>. From Fig. 5.3(d.e.f), water adsorption may occur on graphene due to the increase presence of C-O,

C=O, or COOH peaks<sup>17</sup>. Relevant to Raman results, XPS analysis has revealed that the C-N/F groups obviously influence graphene-DLC heterostructure electronic states.

Using Hall Effect measurement, electrical measurements (sheet resistivity and sheet carrier density) were measured at room temperature and used to calculate the Hall mobility for the various heterostructures. The values found are recorded in Table 5.1. Pristine graphene transferred on different terminated DLC gets a p-type system, which acts as donors that graphene  $\pi$  electrons transfer from surface to the DLC or interface<sup>6</sup>. The maximum mobility is associated to the GFDLC heterostructure (twice of GDLC's mobility), corresponding to the lowest carrier density. As explained by Avouris, an important factor affecting the graphene mobility is the carrier density, where the increase of density induces the decrease of mobility depending on the dominant scatters<sup>18,19</sup>. Therefore, the lowest mobility from GNDLC samples depends on the highest carrier density. As reported in the Raman and XPS analysis, C-N/F groups enable to affect the graphene-DLC heterostructure properties. The large presence of  $CF_x$  groups reduces the substrate's surface energy, which causes a lower surface trap density but still keeps big optical energy gap<sup>8</sup>. However, nitrogen addition is able to increase graphitization, which induces the decrease of the optical energy gap<sup>14</sup>. Owing to the decrease of optical energy gap, a smaller phonon energy of NDLC films weakens the  $\rho$  bands scattering, which leads to low electronic mobility<sup>4,18</sup>. From the Hall Effect results, fluorine terminated DLC supporting substrates give better electronic properties, while GNDLC heterostructure shows more metallic-like character.

**Table 5.1 Hall Effect results for different graphene-DLC heterostructure**

Sample	Sheet resistivity (Ohm/sq)	Carrier density( $cm^{-2}$ )	Mobility ( $cm^2/Vs$ )
<b>GDLC</b>	1799	$1.9 \times 10^{13}$	173.7
<b>GFDLC</b>	1702	$1.1 \times 10^{13}$	313.7
<b>GNDLC</b>	1801	$4.3 \times 10^{13}$	84.3

## 5.4 Conclusions

In summary, the graphene-DLC/NDLC/FDLC heterostructure were investigated in terms of the surface morphology, chemical composition, and microstructure by means of AFM, Raman spectroscopy, XPS and Hall Effect system. Different terminations changed the roughness of DLC films, which induced the Raman D and G peak shifting with the increase of disorders and  $sp^2$  C=C transiting to  $sp^3$  C-C shown from XPS results owing to C-N/F groups. Raman and XPS analysis for graphene-DLC heterostructure suggests graphene properties changed by interaction between two layers and different addition groups. GFDLC show better electronic mobility, while GNDLC reveals metallic-like characters. Based on this research and IBM high frequency FET results, better graphene transistors will be achieved. Different DLC support substrates may offer better 2D device applications.

## Reference:

1. Balandin, A. a, Ghosh, S., Bao, W., Calizo, I., Teweldebrhan, D., Miao, F., & Lau, C. N. (2008). Superior thermal conductivity of single-layer graphene. *Nano Letters*, 8(3), 902–7.
2. Robertson, J. (2002). Diamond-like amorphous carbon. *Materials Science and Engineering: R: Reports*, 37(4-6), 129–281.
3. Casiraghi, C., Piazza, F., Ferrari, a. C., Grambole, D., & Robertson, J. (2005). Bonding in hydrogenated diamond-like carbon by Raman spectroscopy. *Diamond and Related Materials*, 14(3-7), 1098–1102.
4. Amir, O., & Kalish, R. (1991). Properties of nitrogen-doped amorphous hydrogenated carbon films. *Journal of Applied Physics*, 70(9), 4958.
5. Grill, A. (1999). Diamond-like carbon : state of the art, 8(July 1998), 428–434.
6. Bendavid, a., Martin, P. J., Randeniya, L., Amin, M. S., & Rohanizadeh, R. (2010). The properties of fluorine-containing diamond-like carbon films prepared by pulsed DC plasma-activated chemical vapour deposition. *Diamond and Related Materials*, 19(12), 1466–1471.
7. Li, X., Zhu, Y., Cai, W., Borysiak, M., Han, B., Chen, D., ... Ruoff, R. S. (2009). Transfer of large-area graphene films for high-performance transparent conductive electrodes. *Nano Letters*, 9(12),
8. Yu, G. Q., Tay, B. K., Sun, Z., & Pan, L. K. (2003). Properties of fluorinated amorphous diamond like carbon films by PECVD. *Applied Surface Science*, 219(3-4), 228–237.
9. Nanda, K. ., Sarangi, S. ., & Sahu, S. . (1998). Measurement of surface roughness by atomic force microscopy and Rutherford backscattering spectrometry of CdS nanocrystalline films. *Applied Surface Science*, 133(4), 293–297.
10. Ferrari, A. C., & Robertson, J. (2004). Raman spectroscopy of amorphous, nanostructured, diamond-like carbon, and nanodiamond. *Philosophical Transactions. Series A, Mathematical, Physical, and Engineering Sciences*, 362(1824), 2477–512.
11. Lithography, N., Graphene, M., & Hydrogenation, U. (2011). Nanoscale Lithography on Monolayer Graphene Using Hydrogenation and, (8), 6417–6424.
12. Ferrari, A. C. (2007). Raman spectroscopy of graphene and graphite: Disorder, electron–phonon coupling, doping and nonadiabatic effects. *Solid State Communications*, 143(1-2), 47–57.
13. Ferrari, A. C., & Basko, D. M. (2013). Raman spectroscopy as a versatile tool for studying the properties of graphene. *Nature Nanotechnology*, 8(4), 235–46.
14. Ech-chamikh, E., Essafti, a., Ijdiyaou, Y., & Azizan, M. (2006). XPS study of amorphous carbon nitride (a-C:N) thin films deposited by reactive RF sputtering. *Solar Energy Materials and Solar Cells*, 90(10), 1420–1423.

15. Vander Wal, R. L., Bryg, V. M., & Hays, M. D. (2011). XPS analysis of combustion aerosols for chemical composition, surface chemistry, and carbon chemical state. *Analytical Chemistry*, 83(6), 1924–30.
16. Sciences, A. (n.d.). Effect of fluorinated diamond surface on charge state of nitrogen-vacancy centers Shanying Cui and Evelyn L. Hu, 1–11.
17. Wu, Y., Wang, B., Ma, Y., Huang, Y., Li, N., Zhang, F., & Chen, Y. (2010). Efficient and large-scale synthesis of few-layered graphene using an arc-discharge method and conductivity studies of the resulting films. *Nano Research*, 3(9), 661–669.
18. Avouris, P. (2010). Graphene: Electronic and Photonic Properties and Devices. *Nano Letters*, 4285–4294.
19. Chen, J.-H., Jang, C., Xiao, S., Ishigami, M., & Fuhrer, M. S. (2008). Intrinsic and extrinsic performance limits of graphene devices on SiO<sub>2</sub>. *Nature Nanotechnology*, 3(4), 206–9.

# Chapter 6

## Graphene-Nanodiamond Heterostructure and their Applicant of Field Effect Transistors

### 6.1. Introduction

Current studies have typically employed readily available Si/SiO<sub>2</sub> wafers as the substrate, which creates a thermal capacity problem reducing the current capacity of graphene due to the highly thermally resistive SiO<sub>2</sub> layer<sup>1,2</sup>. In an attempt to overcome this problem, diamond and diamond-like-carbon (DLC) have been explored as they offer insulating properties whilst being superior in terms of thermal conductivity, with a large optical phonon energy and potentially a lower surface trap density<sup>1,3</sup>. Graphene devices on ultrananocrystalline diamond (UNCD) and single crystal diamond (SCD) have been shown to increase the amount of current that graphene devices are capable of handling<sup>3</sup>. For commercial electronics, substrates that can be produced using large volume production and at low cost are essential for any new technology. Here, the potential advantages of the use of low-cost, large area compatible nanodiamond (ND) thin films, rather than UNCD and SCD for fabricating graphene-nanodiamond heterostructure devices are explored. ND inherits most of the outstanding properties of bulk diamond, but delivers them at the nanoscale, including hardness, high thermal conductivity, chemical stability, electrical resistivity and a large bandgap<sup>4-6</sup>. NDs fabricated by a detonation process (~5nm) are readily available at low cost and can be readily attached to any 2D or 3D materials through simple sonication from solution<sup>4</sup>. To control the surface performance of the NDs, hydrogen termination of the ND surface leads to an increase of the surface optical phonon energy and stabilization of

nanostructures<sup>7-9</sup>. Compared with high cost SCD, with the highest thermal conductivity of bulk materials, the low cost and easily deposited ND films have been found to have high thermal conductivity around 5-50 W/mK<sup>10</sup>, which is higher than the thermal conductivity of UNCD (8.6-16.6 W/mK) and diamond-like-carbon (0.2-3.5 W/mK)<sup>11,12</sup>.

In this chapter, a cost effective and mass producible method to create a monolayer ND capable of tuning the properties of graphene for the fabrication of Field-Effect Transistors (FETs) is demonstrated. Compared to the pristine graphene transferred onto SiO<sub>2</sub>/Si substrates, the mobility increased by 60% on graphene on hydrogen terminated nanodiamond (GrHND). The detailed material properties of graphene on ND surface with and without hydrogen termination treatment have been investigated using Fourier transform infrared spectroscopy (FTIR), and Raman spectroscopy. It shows that the hydrogen termination treatment not only removed surface contamination from monolayer ND, but also provided a suitable linkage between ND and graphene to form a conductive path, as demonstrated in electrochemical impedance spectroscopy (EIS) measurements. The carrier mobility of GrHND is no less than that of graphene on hydrogen terminated SCD (GrHSCD). In addition, GrHND demonstrated a stable Hall mobility with temperature. High-k dielectric top-gate graphene transistors with gate length of 200 nm and 500 nm were fabricated using focused ion beam (FIB) using Tungsten carbide (WC) contacts to improve the energy transfer between diamond and metal<sup>6</sup>. This research offers a new approach for commercial graphene transistor applications.

## **6.2. Experimental Section**

As shown in Fig. 6.1(a), the monolayer nanodiamond films were first deposited on the SiO<sub>2</sub>/Si substrate with 300nm thickness of SiO<sub>2</sub>. Nanodiamonds were supplied prepared in

solution from ultra-dispersed detonation nanodiamonds (New metals & Chemicals Corporation, Japan). Depositions were made by immersing the substrate material in the ND solution (0.05g/L of NDs) followed by sonication (10 min). Hydrogen termination for NDs was performed using a Seki AsteX AX6550 reactor and keeping following parameters for 5 hours: microwave power, 600W; H<sub>2</sub> 200 sccm; pressure 10 Torr; temperature 500°C. CVD grown monolayer graphene on a copper foil (Graphene Supermarket) was coated with PMMA. The PMMA-coated graphene was treated with Iron nitrate solution to etch away the Cu foil. The floating PMMA coated graphene was scooped out of the bath and cleaned in DI water to transfer onto H-terminated NDs samples. PMMA was removed by acetone.

The surface morphology of the various films was measured over 10 $\mu$ m $\times$ 10 $\mu$ m and 1 $\mu$ m $\times$ 1 $\mu$ m regions by scanning atomic force microscopy (AFM, Veeco Dimension V) in tapping mode for H-terminated NDs. The chemical composition and bonding states of the films were characterized using Fourier transfer infrared spectrometry (FTIR, Perkin Elmer Spectrum One) in transmission mode and X-ray photoelectron spectroscopy (XPS, Thermo Scientific) with the Al K  $\alpha$  line as the exciting source. A micro Raman spectroscopy system (Renishaw Invia) operating at 514.5 nm was used to study the film microstructure, where the laser output power used was 1mW. Impedance spectroscopy was applied in the range of 0.1 Hz to 10MHz in vacuum at elevated temperature from room temperature to 500C using an Autolab electrochemical system. Hall Effect measurements (1T electromagnet, Lakeshore Cryogenics System) were performed to determine graphene carrier mobilities using the “van der Pauw” method, by which four ohmic metal contacts (10nm Ti-300nm Au) were placed on the topside of the graphene layers at room temperature.

Graphene field-effect transistors were fabricated by Carl Zeiss Focused Ion Beam Microscope and Atomic Layer Deposition. A dual-beam instrument (Carl Zeiss XB1540 cross-beam Focussed-Ion-beam microscope) has been used to pattern samples without using masks, giving a feature size as small as 10 nm. The instrument combines a FIB and a SEM column in the same chamber and is fitted with a gas-injection system to allow local material depositions (Tungsten carbides WC, SiO<sub>2</sub>, and Platinum Pt) and material-specific preferential milling to be performed by introducing reactive gases in the vicinity of the electron or ion probe. The electron column delivers the imaging abilities of the SEM which is less destructive than FIB imaging. SEM imaging of the graphene sample before milling identifies a clean area suitable for FET fabrication. Keep one clean graphene area 5 $\mu$ m $\times$ 10 $\mu$ m then other surrounding area around 100 $\mu$ m $\times$ 110 $\mu$ m were milled by using a 30kV Ga<sup>+</sup> beam with a current of 2nA to remove the graphene and nanodiamond layers. Before depositing S/D/G contact patterns, insulator material (SiO<sub>2</sub>) were deposited on surrounding area to 50nm thickness. Three contacts patterns 40 $\mu$ m $\times$ 40 $\mu$ m were coated by Tungsten Carbide with thickness of 200nm using a 30kV/2nA beam. A final gentle polish with Ga<sup>+</sup> ions (30kV/ 5pA) was used to clean the graphene area edge and remove side damage. Finally connect big contact pattern with graphene area edge by WC using a 30kV/50pA beam. After deposition of 10nm Al<sub>2</sub>O<sub>3</sub> layer by Atomic layer deposition (ALD), one narrow gate channel was built on the top. In this paper, the gate sizes are 500nm $\times$ 5 $\mu$ m and 200nm $\times$ 5 $\mu$ m.

### **6.3. Results and Discussion**

#### **6.3.1 Characterisation of Graphene-H-ND heterostructures**

A schematic view of the GrHND heterostructures used here, supported on a SiO<sub>2</sub>/Si substrate (300 nm SiO<sub>2</sub>) is shown in Fig. 6.1(a). The ND monolayer was obtained by first coating the

SiO<sub>2</sub>/Si substrate with an ND solution, followed by thermal hydrogenation (more details in experimental section). The surface coverage and roughness of the ND layer were identified by atomic force microscopy (AFM), shown in Fig. 6.1(b) both as a top-view (1μm×0.5μm) and a 3D-view (1μm×1μm). It shows the ND nanoparticles (10-20 nm) form a homogenous layer on the substrate surface. The mean surface roughness is around 2.7 nm and the height of ND layer suggests it has a monolayer characteristic. The uniformity of the deposited ND films is important as the electronic properties of graphene can be easily modified by surface morphology of supporting materials such as big defects, local strain *etc.*<sup>13</sup>. The hydrogen termination treatment used here aims to reduce the density of surface states<sup>4</sup>. A comparison of Fourier transform infrared spectroscopy (FTIR) spectrums of untreated ND and H-ND are shown in Fig. 6.1(c). The peak observed at 1726 cm<sup>-1</sup> is characteristic of the C=O stretching band involved in carboxylic acid groups and anhydride functionalities<sup>14</sup>. The wide peak in the 3000-3600 cm<sup>-1</sup> range is attributed to the OH of adsorbed water. Complex mixed peaks of ND surface groups (C-OH, COO<sup>-</sup>, C-O-C, C-H) are observed in the 1000-1500 cm<sup>-1</sup> range<sup>15</sup>. These indicate dangling bonds on the surface of the ND films have highly reactive with air at room temperature. After hydrogen treatment, the intensities of all of the complex mixed peaks from 1000 to 1500 cm<sup>-1</sup> have been reduced. The free and adsorbed -OH peaks have disappeared in the region of 3000-3600 cm<sup>-1</sup>, while the peak at 2923 cm<sup>-1</sup> has become much stronger, being assigned to the C-H stretching of the hydrogenated ND surface coupled with the CH<sub>x</sub> bands at 1461 cm<sup>-1</sup> (CH<sub>2</sub>) and 1377 cm<sup>-1</sup> (CH<sub>3</sub>)<sup>16</sup>.

Raman spectroscopy was applied to characterise the graphene-ND heterostructure as Raman spectra provides common feature mapping for all carbon materials<sup>17,18</sup>. The incident power was kept to <1mW to avoid sample damage or laser-induced heating<sup>19</sup>. Fig. 6.1(d) shows the Raman spectra for ND, H-ND films and the two types of graphene-ND heterostructures. The

three main peaks identifying the vibrational modes of graphene are the D, G and 2D peaks, as labelled in Fig. 6.1(d). The G peak assigns to the  $E_{2g}$  phonon at the Brillouin zone

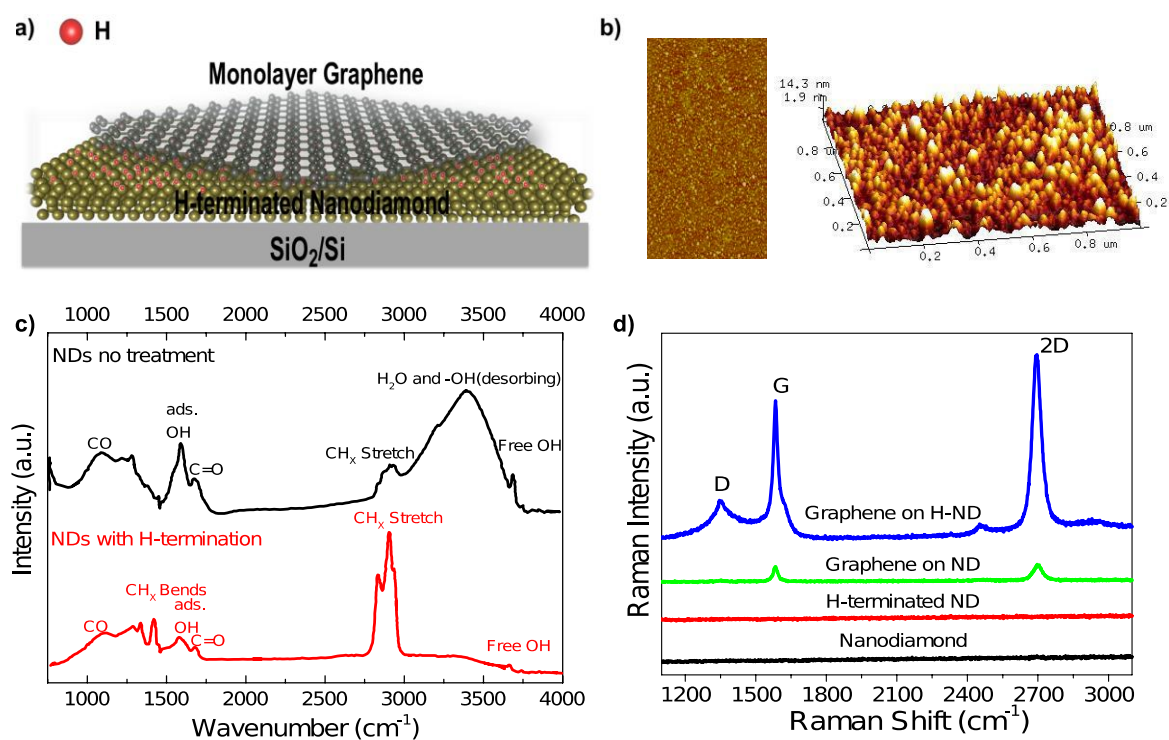


**Figure 6.1 (a) Schematic view of a graphene-HND heterostructure, Nanodiamond with hydrogen termination. (b) AFM images of top-view and 3D-view of hydrogen terminated ND surface. (c) Comparison of FTIR spectra of untreated ND and hydrogen-terminated ND surfaces. (d) Raman spectra of untreated ND, H-ND, graphene-ND, and graphene-HND.**

centre and the D peak is due to the breathing modes of  $sp^2$  phase and defects for those activations<sup>20</sup>. The most prominent feature in graphene is the 2D peak whose shape distinguishes single and multilayer graphene<sup>21</sup>. As expected, no Raman peaks can be identified from monolayer dispersed ND and H-ND surfaces given the low incident power and strong fluorescence generated by the green laser source (514 nm)<sup>22</sup>. The positions of D, G and 2D peaks are listed in the Table 6.1. Unavoidable impurity charge doping and mixed  $sp^3/sp^2$  bonded phase induced by the transfer of graphene onto ND and H-ND, the dangling

bonds from ND and H-ND surfaces shown in FTIR results lead to the observed shift in the Raman peaks<sup>23,24</sup>. The G peak position strongly depends on the interaction between graphene and its environment<sup>25</sup>. Compared with previous studies of graphene on SiO<sub>2</sub>, G peak positions for the graphene-ND heterostructures have an upshift from 1581cm<sup>-1</sup> to 1586.2cm<sup>-1</sup> and 1585.7cm<sup>-1</sup> for untreated ND and H-ND substrates respectively<sup>18</sup>. These G peak shifts are due to the electron-phonon coupling which results in a shift in the Fermi level, thus doping the graphene<sup>25,26</sup>. Compared to monolayer graphene on SiO<sub>2</sub> where the 2D peak is at 2700cm<sup>-1</sup><sup>26</sup>, the 2D peak positions are also slightly different on the two different substrates and have downshifts by 2 and 10 cm<sup>-1</sup> for ND (2698 cm<sup>-1</sup>) and H-ND (2690cm<sup>-1</sup>) substrates, respectively. This is due to hole doping<sup>27</sup>. The 2D peak widths for both heterostructures are within 25-28 cm<sup>-1</sup>, suggesting the graphene is a monolayer<sup>19</sup>. Additionally, since the 2D peak responds to all electron scattering processes while the G peak is not affected by such processes, the integrated intensity ratio of I<sub>2D</sub>/I<sub>G</sub> provides additional information<sup>21</sup>. The impurity charges and electron transfer induce an increase of scattering with increased carrier concentration, decreasing the ratio of I<sub>2D</sub>/I<sub>G</sub><sup>18</sup>. The ratios of I<sub>2D</sub>/I<sub>G</sub> for both heterostructures are 1.06 and 1.17 respectively, proving electrons transfer between the interface of graphene and ND and high doping for graphene has occurred; for low doping the 2D peak is expected to be 3-5 times stronger than the G peak<sup>18</sup>. The first order D peak can only be observed from Gr-HND, suggesting the C-H stretching leads to the appearance of D peak. The emergence of the D peak is associated with disorder and the sp<sup>3</sup>/sp<sup>2</sup> ratio<sup>21</sup>, in line with previous studies conducted on hydrogenated graphene layers<sup>2</sup>. As observed previously from the FTIR results, the strong C-H stretching for H-terminated sample will be responsible for the sp<sup>3</sup> signal, leading to heterostructures formed from sp<sup>3</sup>/sp<sup>2</sup> mixtures. Both FTIR and Raman results show a clear modification occurs to the graphene lattice with H-termination treatments of the

NDs. Charge transfer between graphene and NDs leads to disorder and high doping; hence tuning the graphene electronic properties.

**Table 6.1. Intensities for different peaks**

Sample	D peak	G peak	2D peak
<b>Gr-ND</b>			
Peak position		1586.2	2698.2
Intensity		2308.98	2466
<b>Gr-HND</b>			
Peak position	1347.1	1585.7	2690.2
Intensity	3958.3	6328.6	7430.9

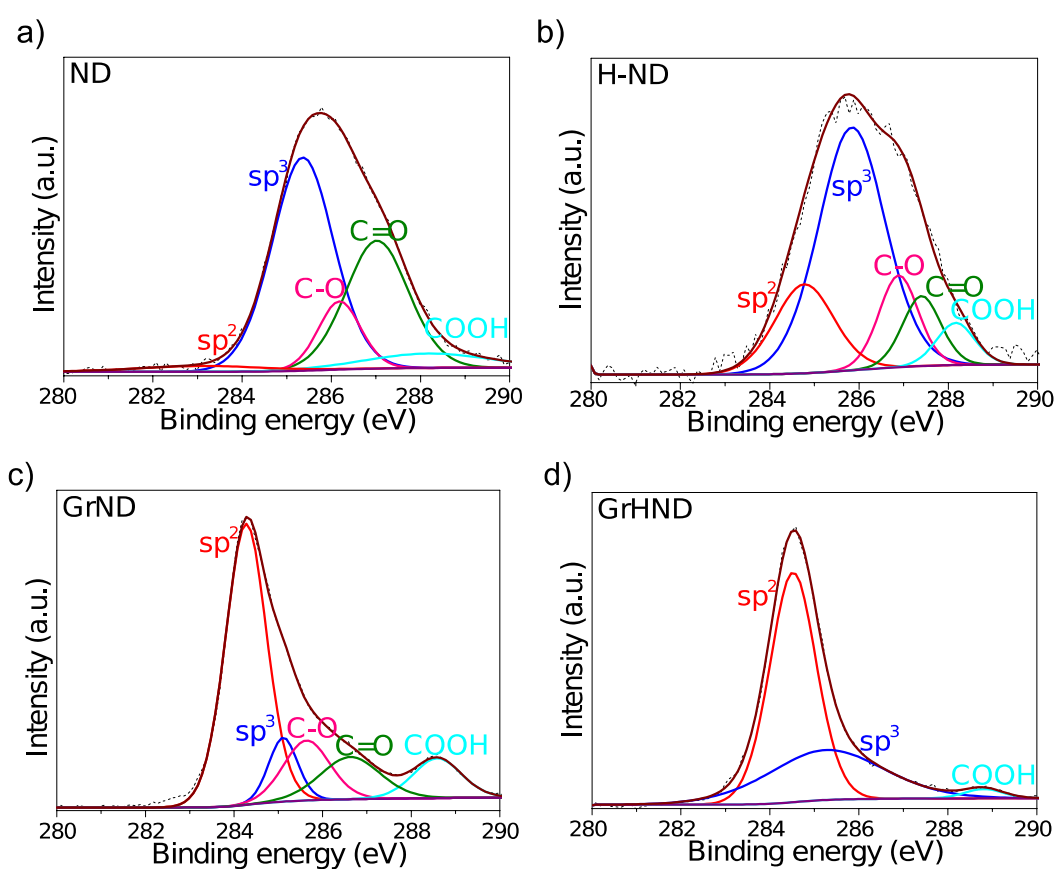


**Figure 6. 2 High resolution C1s XPS spectra of ND (a), H-terminated ND (b), graphene on ND (c), and graphene on H-terminated ND (d).  $sp^2$  peak red line,  $sp^3$  peak blue line, C-O peak pink line, C=O peak green peak, COOH peak cyan line.**

XPS was used to estimate the fraction of  $sp^2$  and  $sp^3$  atoms present<sup>28</sup>. Fig. 6.2 shows the C 1s spectral region for ND, H-ND surfaces and for each with graphene overlayers. The C 1s

core-level spectra of samples were fitted by CasaXPS software with the following reference peaks: 284.5eV binding energy (BE) assigned to  $sp^2$  hybridized C atoms in ND (graphite structure) and graphene<sup>28,29</sup>; 285.4eV BE assigned to  $sp^3$  hybridized C atoms due to the formation of C-H and the C-C bonds in the ND film<sup>28,30</sup>; other components including C-O, C=O, and COOH with much higher BEs ( 286eV, 287.6eV, 288.6eV) which originated from interface states and ambient oxygen and moisture<sup>30-32</sup>. The XPS spectrum of ND films, shown in Fig 6.2(a), indicates an oxygenated surface with different functional groups due to air oxidation. At the same time, there is also a small  $sp^2$  contribution since NDs are partially covered by a thin layer of graphite<sup>4</sup>. Hydrogen termination of NDs (Fig. 6.2(b)) reveals the  $sp^3$  hybridization of the deposited carbon by saturation with hydrogen atoms, whilst thermal annealing (under 500°C for 5 hours for H-termination detailed in experimental section) leads to graphitization and an increase of the  $sp^2$  phase<sup>30,33</sup>. As shown in the previous FTIR results, most oxygen functional groups were reduced by Hydrogen termination. In agreement with this, the XPS results show that after transferring graphene, oxygen functional groups are more significant on GrND heterostructures (Fig. 6.2(c)) rather than GrHND heterostructures (Fig. 6.2(d)). When accounting for the D peak assignment in Raman analysis, these XPS results indicate disorder and the absence of an  $sp^3$  phase contributing to the D peak<sup>2,3</sup>. The C-H stretching  $sp^3$  bonds are likely to affect the translational symmetry of C=C  $sp^2$  bonds in graphene, which is similar to the effect of hydrogenating graphene<sup>3</sup>. To analyse the hydrogen coverage first the  $sp^3$  coverage was determined as  $\theta/(1+\theta)$  where  $\theta$  is defined as the intensity area of  $sp^3$  and  $sp^2$  peaks<sup>2</sup>. For pristine CVD graphene transferred onto untreated ND films the  $sp^3$  coverage was found to be ~19%, while for graphene transferred on H-ND films the  $sp^3$  coverage increases to ~38% (the intensity area of  $sp^2$  and  $sp^3$  from Table 6.2). Hence, by hydrogen terminating the ND substrates, the graphene layer is indirectly hydrogenated with an H coverage of  $38\% - 19\% = 19\%$ .

**Table 6.2. Intensity area for  $sp^2$  and  $sp^3$  peaks**

Sample	$sp^2$	$sp^3$	$\theta(I_{sp3}/I_{sp2})$	$\theta/(1+\theta)$
Gr-ND	64137.23	14852.65	0.23	19%
Gr-HND	28043.05	17246.72	0.62	38%

### 6.2.2 Electronic transport in graphene-nanodiamond heterostructures

The electrical characteristics of the heterostructures were examined using AC electrochemical impedance spectroscopy (EIS) measurements. Two Au/Ti (300nm/10nm) contacts were deposited on the top-side corners of square samples. EIS was carried out in vacuum at temperatures ranging from room temperature to 500C as shown in Fig. 6.3 (more details for different temperature in Fig. 6.4). The frequency scale is from 0.1 Hz to 10MHz. At room temperature the Cole-Cole plot consists of two semicircles<sup>34</sup>, which suggests two conduction paths in the heterostructure. One conduction path can be associated with the path the charge carriers take at the surface of graphene in contact with the exterior. The other path can be associated with the graphene-nanodiamond interface, where the two carbon surfaces are weakly linked by hydrogen bonds. By increasing the temperature up to 125C, the results show that the radius for the low frequency semicircle increases while the high frequency semicircle shows little change in shape (Fig. 6.4(a)). If we assign the low frequency semicircle to the graphene surface conduction path, we would expect the conductivity to decrease owing to the evaporation of the water layer on the surface. At this temperature we would expect negligible modifications in the graphene-ND interface, so the high frequency semicircle may be associated to this conduction path. At higher temperatures from 150C to 250C both semicircles start to decrease. For the low frequency semicircle this might be due to the elimination of residues or remaining PMMA on the graphene surface, which would explain its increasing conductivity. Whereas for the high frequency semicircle, this can be explained in terms of a possible activation of the hydrogen bonds in the graphene-ND interface. Further increasing the temperature the high frequency semicircle decreases at a

higher rate than the other, and results show that after 275C we have only one semicircle that further decreases up to 500C (Fig. 6.4(c)). The low frequency semicircle after 400C is too small to show. At these temperatures we would expect breaking of C-H bonds between the graphene-ND interface, which would ultimately eliminate its associated conduction path

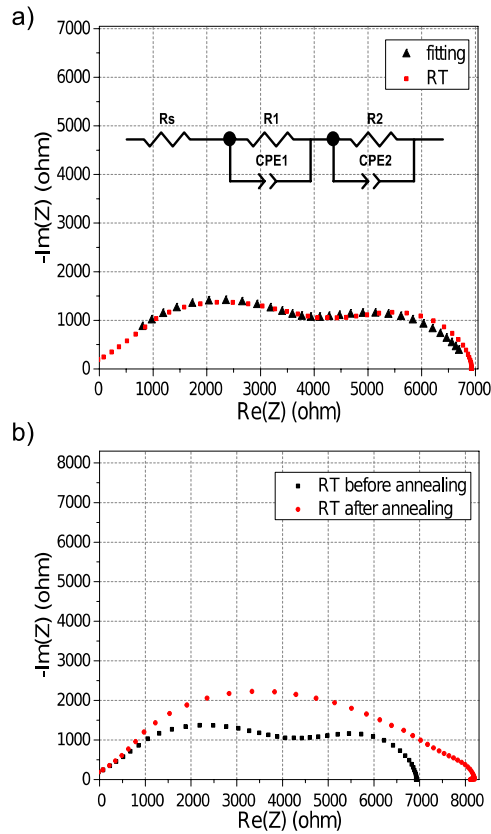


**Figure 6.3 (a) Impedance spectra of Gr-HND heterostructure (red line). The inset is the equivalent circuit model and the fitting line in black. (b) Comparison of room temperature Impedance spectra before and after annealing (500C).**

leaving only the graphene surface conduction path. This suggests the low-frequency semicircle is assigned to the graphene surface conduction path, while the high-frequency semicircle is explained in terms of a possible activation of the hydrogen bonds in the graphene-ND interface<sup>35,36</sup>. The equivalent circuit model of this heterostructure is also shown in Fig. 6.3(a) as an inset, representing the internal resistance for the conductive path according to literature<sup>34,37,38</sup>. The equivalent circuit model shows two RC in series and the

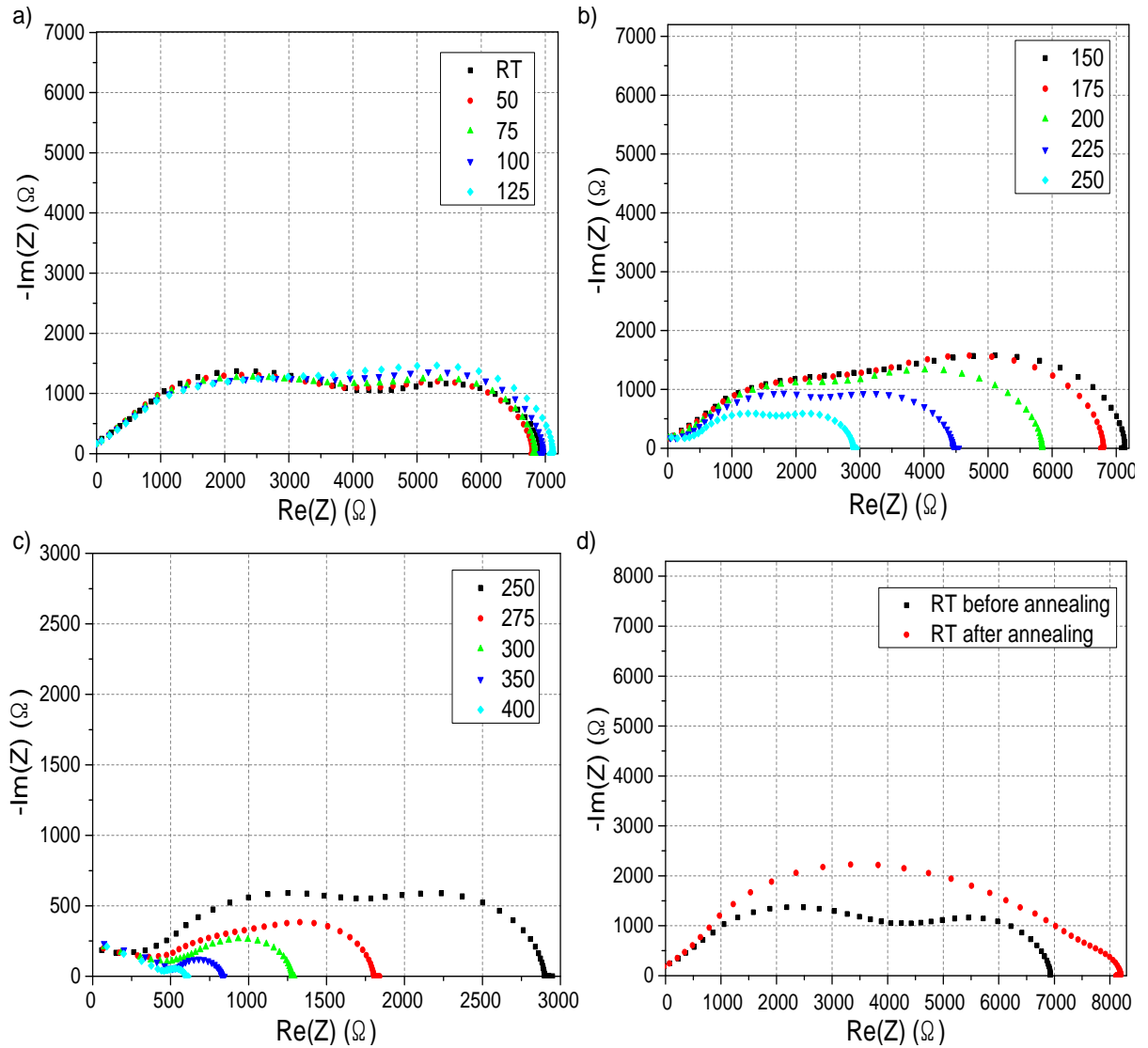


**Figure 6.4 Impedance spectra of graphene on H-terminated ND heterostructure for different temperature. (a) room temperature to 125C; (b) 150C to 250C; (c) 250C to 400C; (d) room temperature results before and after annealing.**

black line in Fig. 6.3(a) is the fitting result following this model. In the equivalent electrical circuit,  $R_s$  ( $209.5\Omega$ ) represents the total resistance of the electrolyte and electrodes;  $R_1$  ( $3632\Omega$ ) is assigned from the interface linked by H-bonds;  $R_2$  ( $3054\Omega$ ) is from the graphene surface. After high temperature annealing (during measurement) and cooling to room temperature again, two clear semicircles were not seen again because of the breaking of C-H bonds between the GrHND interface at the highest temperatures. As shown in the following

Hall effect section, the effect of high temperature annealing of GrHND by leads to properties similar to those for GrND (Table 6.3).

Hall effect measurements can be used to determine sheet resistivity, carrier density and Hall mobility values for a semiconductor<sup>39</sup>. The carrier transport properties of GrHND samples were investigated using the Van der Pauw method shown in the inset of Fig. 5(a). The sample was placed on an insulating platform where four Hall probes were put on four corner Au/Ti (300nm/10nm) ohmic contacts in a vacuum chamber. Here we compare the two different heterostructures: GrHND (Nanodiamonds) and GrHSCD (single crystal diamond). It can be seen from Fig. 6.5(a), the Hall mobilities for both samples are comparable at 300K, the difference being within 10 cm<sup>2</sup>/Vs. As the temperature increases, the Hall mobility of GrHND exceeds that of GrHSCD. The Hall mobility of GrHSCD is proportional to T<sup>-1.1</sup> and drops sharply from 220 cm<sup>2</sup>/Vs to 140 cm<sup>2</sup>/Vs, whilst in the case of GrHND the mobility only decreases by 15 cm<sup>2</sup>/Vs as the temperature increases. At high temperatures, 450K, GrHND outperforms GrHSCD in terms of mobility by 33%. This phenomenon can be attributed to phonon scattering, which is the dominant factor in the SCD case, and phonon scattering increases with temperature. However, for ND the factors for scattering are more complex, including lattice impurities and phonon scattering<sup>40,41</sup>. Hence, it can be anticipated the devices based on GrHND can be operated on wide temperature range without losing performance. For the reference sample, the mobility for graphene transferred directly onto SiO<sub>2</sub>/Si is 132 cm<sup>2</sup>/Vs (Table 6.3). The sheet resistance and carrier densities for both heterostructures have been plotted against temperature in Fig. 6.4(b). The sheet resistance of GrHND is stable around 2600 Ω/sq from 300K to 450K whilst the sheet resistance of GrHSCD shows a small increase from 4392 to 5112 Ω/sq over the same temperature range. Meanwhile, the carrier density for GrHND is nearly four times that of GrHSCD; increasing from 1.09×10<sup>13</sup>cm<sup>-2</sup> to a highest point of 1.3×10<sup>13</sup>cm<sup>-2</sup> at 400K, then dropping slightly to

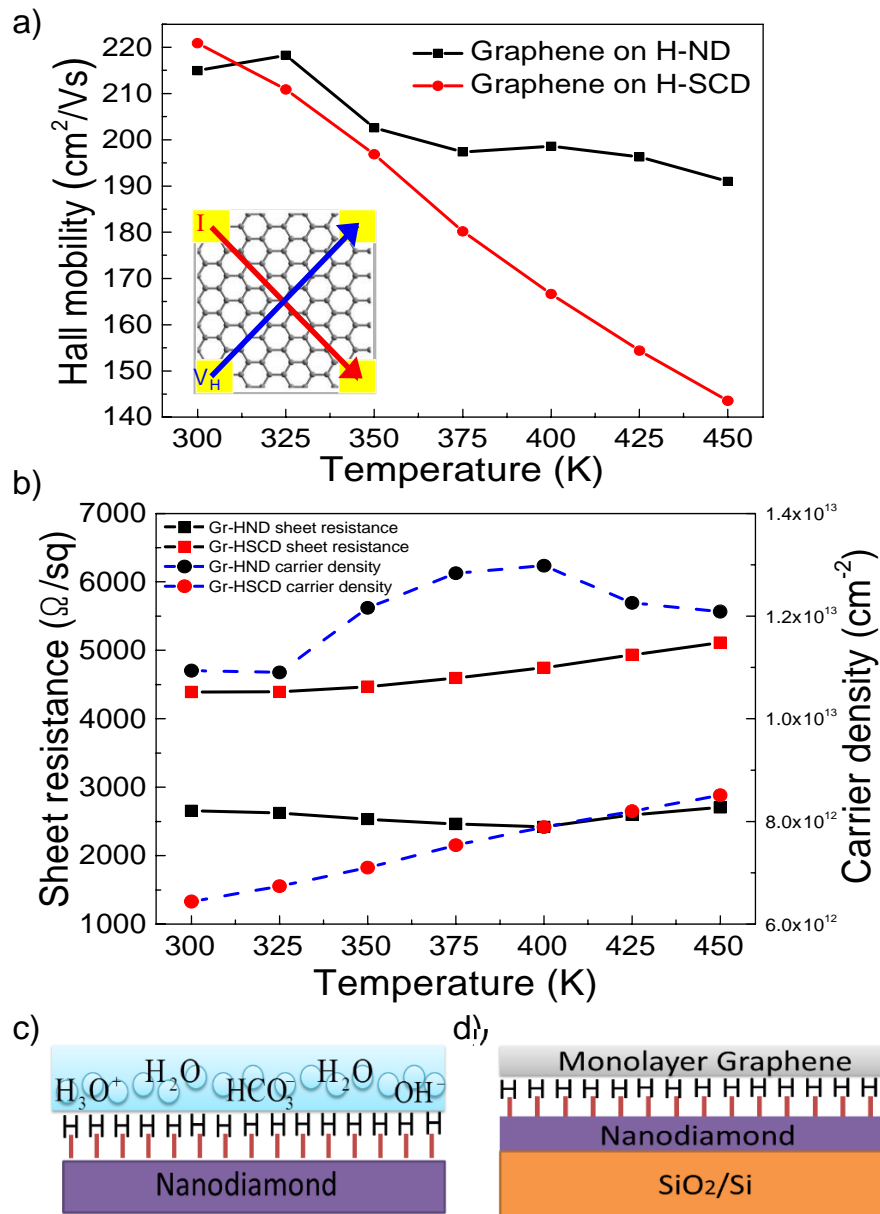


**Figure 6.5 (a) Hall mobility for GrHND and GrHSCD. The inset is Van der Pauw method for measurement. (b) Comparison of sheet resistance and carrier density of GrHND and GrHSCD. (c) Schematic picture of the hydrogenated ND surface in contact with a water layer as it forms in air. (d) Schematic for GrHND heterostructure.**

$1.2 \times 10^{13} \text{cm}^{-2}$  at 450K. The carrier density of GrHSCD shows a linear increase with temperature from  $6.44 \times 10^{12}$  to  $8.51 \times 10^{12} \text{cm}^{-2}$  for room temperature to 450K. Although GrHSCD has lower carrier density which enables an increase in the mobility<sup>42</sup>, GrHND gives a lower sheet resistance which offers superiority in terms of a low resistance channel

for a transistor<sup>4</sup>. This suggests the low cost monolayer ND is a good alternative compared with SCD. From the supporting information (Table 6.3), the electronic properties of annealed GrHND are similar with those for GrND (no H treatment for the ND). All of the heterostructures are p-type systems. As shown in Fig. 6.5(c, d), by hydrogenating any diamond surface conductivity can be improved owing to the reaction between of C-H bands and the water layer<sup>43</sup>. This process is explained by transfer of the –H/-OH lowest unoccupied molecule orbital (LUMO) into the diamond highest occupied molecule orbital (HOMO) by energy preference. This ultimately leaves a hole accumulation layer on the diamond surface. After graphene transfer to hydrogen the terminated diamond surface (Fig. 6.5(b)), the  $\pi$  electrons from the graphene will inject into the diamond surface through the hydrogen bonds. This explains the associated p-type conduction at the graphene H-terminated diamond structures.

**Table 6.3. Hall effect measurement results for different samples**

Sample	Doping	Resistance (k $\Omega$ /sq)	Carrier density (cm <sup>-2</sup> )	Mobility (cm <sup>2</sup> /Vs)
<b>Gr-SiO<sub>2</sub>- Si(reference)</b>	P type	1.05	4.48 $\times$ 10 <sup>13</sup>	132.65
<b>Gr-H-SCD</b>	P type	4.39	6.44 $\times$ 10 <sup>12</sup>	220.86
<b>Gr-O-SCD</b>	P type	1.34	2.79 $\times$ 10 <sup>13</sup>	195.5
<b>Gr-H-ND</b>	P type	2.65	1.09 $\times$ 10 <sup>13</sup>	214.9
<b>Gr-O-ND</b>	P type	2.51	5 $\times$ 10 <sup>13</sup>	50
<b>Gr-ND</b>	P type	4.43	4 $\times$ 10 <sup>13</sup>	33.86
<b>Gr-H-ND (after annealing)</b>	P type	2.78	3.96 $\times$ 10 <sup>13</sup>	56.56

The measured values for the carrier density, mobility, sheet resistivity and doping type, done in room temperature conditions, are recorded in Table 6.3. These measurements were done for CVD graphene transferred on both SCD and ND thin films, where the diamond substrates have been patterned with both hydrogen and oxygen surface terminations. In terms of carrier mobility measurements two main results can be distinguished. Firstly, the maximum

mobility is associated to the H terminations on the diamond surface, corresponding to the lower carrier density. However, a decrease in mobility for the case of O terminations can be associated to the increase in carrier density compared to the case of H terminations. The second important result to be mentioned is the fact that mobility values for both graphene on hydrogenated SCD and ND films are close, of the same order of magnitude. Yet the SCD platform is a very expensive approach for commercial applications, and a low cost diamond substrate is desirable. Effectively these results show that our prepared ND films are a less expensive platform for graphene, with the prospect of low cost carbon  $sp^2$  -on-  $sp^3$  technology.

### **6.3.3 Graphene Field Effect Transistor on Hydrogen terminated nanodiamond**

Top gate FET devices were fabricated on GrHND heterostructures with different gate channel sizes. A Focussed-Ion-beam (FIB) tool, giving a feature size as small as 10nm, was used to define the source, drain contacts, gate electrodes, and also for local material depositions for contact formation using tungsten carbide (WC). A top-gate  $Al_2O_3$  dielectric was grown by atomic layer deposition (ALD). Detailed fabrication information is given in the experimental section. Fig. 6.6(a) shows schematics of the fabricated devices and Fig. 6.6(b,c) show SEM images of the FET design. From Fig. 6.6(c) it can be seen that graphene was removed by FIB milling around the FET channel and the gate length is sub-micron. Fig. 6.6(d, e) show the output characteristics of two graphene devices, one with a gate length of 500nm and another with a gate length of 200nm. The linear output behaviour indicates the presence of good ohmic contacts. The drain voltage sweeps from 0 V to 1 V and the gate voltage changes from -4 V to 4 V. As shown in the insets, the Dirac point voltage obtained from the long gate device is around -1 V, which suggests n-doping<sup>32</sup>. However, from our

Raman and Hall effect results, the structure is considered p-type. Previously, Li has reported that a graphene FET displayed p-type behaviour due to the Ti layer being used serving as the

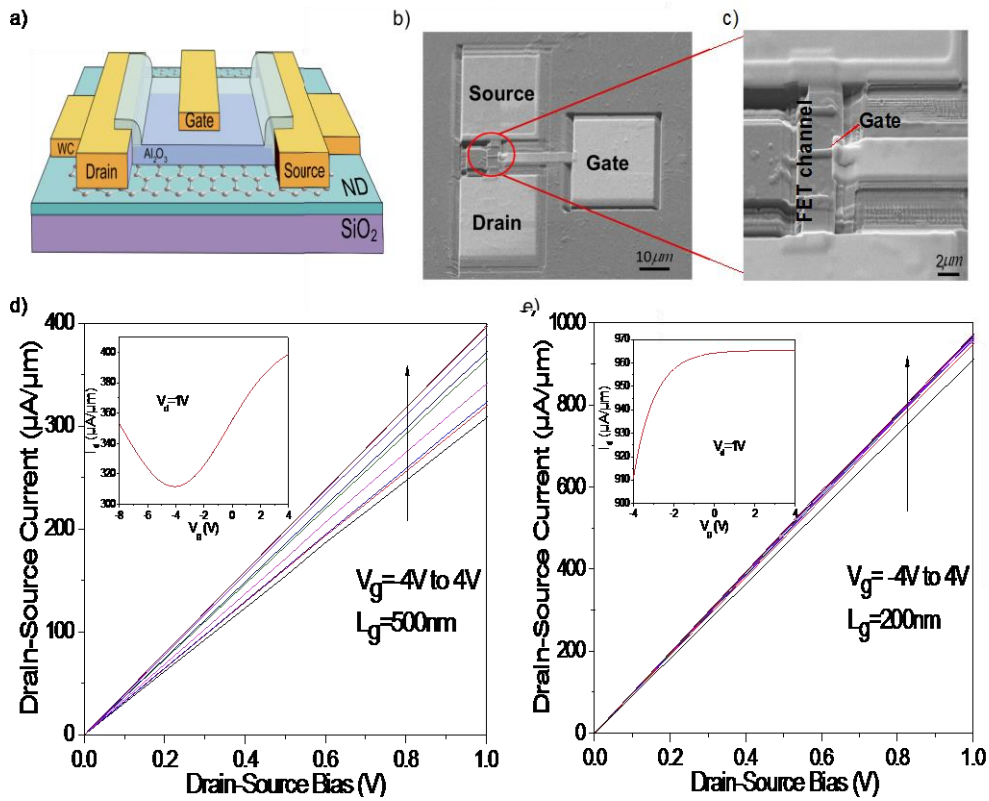


**Figure 6.6** Fabrication and output characteristics for graphene FET on H-terminated ND. (a) Schematic view of a top-gate FET; (b) SEM image of a top-gated devices, Scale bar, 10  $\mu\text{m}$ . (c) FIB image of the 500 nm device. Scale bar, 2  $\mu\text{m}$ . d) and e) Output characteristics of a 500nm device (d) and a 200 nm device (e). Insets, transfer characteristics at drain-source voltage  $V_{ds}=-1\text{V}$ .

hole dopant, as well as adsorption of oxygen and water molecules<sup>44</sup>. In the present case, Ti contacts were used in the material studies but WC contacts have been used for the devices. WC contacts may be acting as an electron dopant, through energy being transferred from metal into diamond's phonon bands<sup>6</sup>. The inset for short gate device shows the output characteristics without an inflection point, which suggests that graphene provides efficient

contacts to the conduction band of ND for electron injection<sup>45</sup>. The gate modulation of the short gate device is much weaker than that of the long gate device due to the more dominant role of the contact resistance in short gate devices and the short-channel effect<sup>2</sup>. Device mobility was estimated to be

$$\mu = \left( \frac{dI_{ds}}{dV_g} \right) \times \left[ \frac{L}{WC_i V_{ds}} \right] \quad (6.1)$$

where L is the channel length (5  $\mu\text{m}$ ), W is the channel width (500 nm) and  $C_i$  is the area capacitance per unit area between the channel and gate ( $8 \times 10^{-7} \text{ F/cm}^2$ )<sup>46</sup>. The mobility for long gate device is  $\sim 149 \text{ cm}^2/\text{Vs}$ .

#### 6.4. Conclusion

In summary, a systematic study of the properties of graphene-ND heterostructures has been carried out and the operation of an FET on GrHND structures demonstrated. Due to low cost, easy deposition and high thermal conductivity, monolayer ND is a good alternative support for graphene when compared SCD or UNCD for current-carrying capacitive graphene devices. The properties of graphene on NDs with and without H-termination were investigated using FTIR, Raman spectroscopy, and XPS. The C-H bond present on H-terminated NDs, strongly influences the heterostructure that results from depositing graphene on the NDs. The presence of the H-termination leads to the appearance of a so-called D peak, the shifts of the G and 2D peaks, and the ratio of  $\text{sp}^3/\text{sp}^2$  carbon present. From EIS measurements performed at elevated temperatures, the hydrogen links both ND and graphene to create the charge transfer which induces a conductive interface layer between graphene and ND. The mobility of GrHND increases 60% compared with graphene on  $\text{SiO}_2/\text{Si}$  and is comparable with GrHSCD (single crystal diamond). As temperature is increased, the Hall mobility of GrHND exceeds that of GrHSCD, which strongly decays.

This means that the GrHND layers are more suitable for stable device operation over a wide temperature range. In addition, GrHND heterostructures offer higher carrier densities and lower sheet resistances than those of GrHSCD, offering higher current handling capacity. FETs fabricated on this novel type of herterostructure GrHND gave comparable output characteristics to FETs on graphene-SCD, whilst offering the prospect of low cost large area production of graphene electronics.

## References

1. Wu, Y. et al. High-frequency, scaled graphene transistors on diamond-like carbon. *Nature* 2011, 472, 74–8.
2. Freitag, M., Chiu, H.-Y., Steiner, M., Perebeinos, V. & Avouris, P. Thermal infrared emission from biased graphene. *Nat. Nanotechnol.* 2010, 5, 497–501.
3. Yu, J., Liu, G., Sumant, A. V, Goyal, V. & Balandin, A. a. Graphene-on-diamond devices with increased current-carrying capacity: carbon sp<sup>2</sup>-on-sp<sup>3</sup> technology. *Nano Lett.* 2012, 12, 1603–8.
4. Mochalin, V. N., Shenderova, O., Ho, D. & Gogotsi, Y. The properties and applications of nanodiamonds. *Nat. Nanotechnol.* 2012, 7, 11–23.
5. Graphene, D. & Al, W. E. T. *Electronic Properties of Nanodiamond.* 2012, 1018–1025.
6. Kidalov, S. V. & Shakhov, F. M. Thermal Conductivity of Diamond Composites. *Materials (Basel).* 2009, 2, 2467–2495.
7. Fokin, A. a. & Schreiner, P. R. Band gap tuning in nanodiamonds: first principle computational studies. *Mol. Phys.* 2009, 107, 823–830.
8. Vlasov, I. I. et al. Molecular-sized fluorescent nanodiamonds. *Nat. Nanotechnol.* 2014, 9, 54–8.
9. Taha-Tijerina, J. J. et al. Nanodiamond-based thermal fluids. *ACS Appl. Mater. Interfaces* 2014, 6, 4778–85.
10. Kidalov, S. V., Shakhov, F. M. & Vul, A. Y. Thermal conductivity of sintered nanodiamonds and microdiamonds. *Diam. Relat. Mater.* 2008, 17, 844–847.
11. Shamsa, M. et al. Thermal conductivity of nitrogenated ultrananocrystalline diamond films on silicon. *J. Appl. Phys.* 2008, 103, 083538.
12. Shamsa, M. et al. Thermal conductivity of diamond-like carbon films. *Appl. Phys. Lett.* 2006, 89, 161921.
13. Chaudhary, A., Welch, J. O. & Jackman, R. B. Electrical properties of monodispersed detonation nanodiamonds. *Appl. Phys. Lett.* 2010, 96, 242903.
14. Chung, P.-H., Perevedentseva, E., Tu, J.-S., Chang, C. C. & Cheng, C.-L. Spectroscopic study of bio-functionalized nanodiamonds. *Diam. Relat. Mater.* 2006, 15, 622–625.
15. Chu, C.-D. et al. Temperature-dependent surface CO stretching frequency investigations of functionalized nanodiamond particles. *Diam. Relat. Mater.* 2009, 18, 76–81.
16. Cheng, C.-L., Chen, C.-F., Shaio, W.-C., Tsai, D.-S. & Chen, K.-H. The CH stretching features on diamonds of different origins. *Diam. Relat. Mater.* 2005, 14, 1455–1462.
17. Ferrari, A. C. & Robertson, J. Raman spectroscopy of amorphous, nanostructured, diamond-like carbon, and nanodiamond. *Philos. Trans. A. Math. Phys. Eng. Sci.* 2004, 362, 2477–512.
18. Casiraghi, C., Pisana, S., Novoselov, K. S., Geim, a. K. & Ferrari, a. C. Raman fingerprint of charged impurities in graphene. *Appl. Phys. Lett.* 2007, 91, 233108 .

19. Ferrari, a. C. et al. Raman Spectrum of Graphene and Graphene Layers. *Phys. Rev. Lett.* 2006, 97, 187401.
20. Casiraghi, C. et al. Raman spectroscopy of graphene edges. *Nano Lett.* 2009, 9, 1433–41.
21. Ferrari, A. C. Raman spectroscopy of graphene and graphite: Disorder, electron–phonon coupling, doping and nonadiabatic effects. *Solid State Commun.* 2007, 143, 47–57.
22. Yushin, G. N., Osswald, S., Padalko, V. I., Bogatyreva, G. P. & Gogotsi, Y. Effect of sintering on structure of nanodiamond. *Diam. Relat. Mater.* 2005, 14, 1721–1729.
23. Lim, C. H. Y. X. et al. A hydrothermal anvil made of graphene nanobubbles on diamond. *Nat. Commun.* 2013, 4, 1556.
24. Graf, D. et al. Spatially resolved Raman spectroscopy of single- and few-layer graphene. *Nano Lett.* 2007, 7, 238–42.
25. Pisana, S. et al. Breakdown of the adiabatic Born-Oppenheimer approximation in graphene. *Nat. Mater.* 2007, 6, 198–201.
26. Yan, J., Zhang, Y., Kim, P. & Pinczuk, A. Electric Field Effect Tuning of Electron-Phonon Coupling in Graphene. *Phys. Rev. Lett.* 2007, 98, 166802.
27. Das, a et al. Monitoring dopants by Raman scattering in an electrochemically top-gated graphene transistor. *Nat. Nanotechnol.* 2008, 3, 210–5.
28. Vander Wal, R. L., Bryg, V. M. & Hays, M. D. XPS analysis of combustion aerosols for chemical composition, surface chemistry, and carbon chemical state. *Anal. Chem.* 2011, 83, 1924–30.
29. Ech-chamikh, E., Essafti, a., Ijdiyaou, Y. & Azizan, M. XPS study of amorphous carbon nitride (a-C:N) thin films deposited by reactive RF sputtering. *Sol. Energy Mater. Sol. Cells* 2006, 90, 1420–1423.
30. Xie, F. Y. et al. Surface characterization on graphitization of nanodiamond powder annealed in nitrogen ambient. *Surf. Interface Anal.* 2010, 42, 1514–1518.
31. Wu, Y. et al. Efficient and large-scale synthesis of few-layered graphene using an arc-discharge method and conductivity studies of the resulting films. *Nano Res.* 2010, 3, 661–669.
32. Liu, Z. et al. In-plane heterostructures of graphene and hexagonal boron nitride with controlled domain sizes. *Nat. Nanotechnol.* 2013, 8, 119–24.
33. Krueger, A. & Lang, D. Functionality is Key: Recent Progress in the Surface Modification of Nanodiamond. *Adv. Funct. Mater.* 2012, 22, 890–906.
34. *Impedance Spectroscopy: Theory, Experiment, and Applications.* (John Wiley & Sons). 2005.
35. Vinayan, B. P. et al. Synthesis of graphene-multiwalled carbon nanotubes hybrid nanostructure by strengthened electrostatic interaction and its lithium ion battery application. *J. Mater. Chem.* 2012, 22, 9949.
36. Shao, Y., Wang, H., Zhang, Q. & Li, Y. High-performance flexible asymmetric supercapacitors based on 3D porous graphene/MnO<sub>2</sub> nanorod and graphene/Ag hybrid thin-film electrodes. *J. Mater. Chem. C* 2013, 1, 1245.

37. Zhao, J., Wang, L., He, X., Wan, C. & Jiang, C. Kinetic Investigation of LiCoO<sub>2</sub> by Electrochemical Impedance Spectroscopy ( EIS ). 2010, 5, 478–488.
38. Wang, X. et al. TiO<sub>2</sub> modified FeS nanostructures with enhanced electrochemical performance for lithium-ion batteries. *Sci. Rep.* 2013, 3, 2007.
39. Williams, J. R., Dicarlo, L. & Marcus, C. M. Quantum Hall effect in a gate-controlled p-n junction of graphene. *Science* 2007, 317, 638–41.
40. Efimov, V. . & Mezhov-Deglin, L. . Phonon scattering in diamond films. *Phys. B Condens. Matter* 1999, 263-264, 745–748.
41. Wang, S. G. et al. Electron field emission enhancement effects of nano-diamond films. *Surf. Coatings Technol.* 2003, 167, 143–147.
42. Hwang, E., Adam, S. & Sarma, S. Carrier Transport in Two-Dimensional Graphene Layers. *Phys. Rev. Lett.* 2007, 98, 186806.
43. Nebel, C. E. et al. Hydrogen-induced transport properties of holes in diamond surface layers. *Appl. Phys. Lett.* 2001, 79, 4541.
44. Field-e, G. et al. Ambipolar to Unipolar Conversion in. 2011, 3198–3203.
45. Roy, T. et al. Terms of Use Field-Effect Transistors Built from All Two-Dimensional Material Components. 2014, 6259–6264.
46. Wang, X. et al. Room-Temperature All -Semiconducting Sub-10-nm Graphene Nanoribbon Field-Effect Transistor. *Phys. Rev. Lett.* 2008, 100, 206803.

# Chapter 7

## Graphene-Single Crystal Diamond (100)/(111)

### Hybrid Structure

#### 7.1 Introduction

Owing to the lack of a finite band gap, graphene devices can never be turned off completely, which is an obstacle on the way of the use graphene in logic and high-speed switching devices<sup>1</sup>. Creating a finite gap without degrading the graphene's properties remains challenging even that different approaches have reported to open up the band gap, such as graphene nanoribbons<sup>2</sup>, graphene hydrogenation<sup>3</sup>, graphene doping<sup>4</sup>, and application of strain<sup>5</sup>. Here in this chapter we systematically investigate experimental and simulative study of graphene on different orientation single crystal diamond (100) and (111) (G@SCD) to induce a band gap.

#### 7.2 Experiment section

Single crystal diamond 100 and 111 (Element Six Ltd) were cleaned in strong oxidising solutions to remove any residual surface conductivity due to organic contaminants. The strong acid bath used a mixture of sulphuric acid and ammonium persulphate as the etch solution and a mixture of hydrogen peroxide and ammonium hydroxide as the rinse solution. After cleaning, hydrogen termination for SCD was created using Seki AsteX AX6550 reactor and keeping following parameters for 5 hours: microwave power, 600W; H<sub>2</sub> 200 sccm; pressure 10 Torr; temperature 500C. The CVD grown monolayer graphene on a copper foil was coated with PMMA. The PMMA-coated graphene was treated with Iron

nitrate solution to etch away Cu foil. The floating PMMA coated graphene was scooped out the bath and cleaned in DI water to transfer onto H-terminated NDs samples. PMMA was removed by acetone. The surface morphology of the various films was measured over  $10\mu\text{m}\times 10\mu\text{m}$  and  $1\mu\text{m}\times 1\mu\text{m}$  regions by scanning atomic force microscopy (AFM, Veeco Dimension) in tapping mode for H-terminated NDs. The chemical composition and bonding states of the films were characterized using X-ray photoelectron spectroscopy (XPS, Thermo Scientific) with the Al K  $\alpha$  line as the exciting source. A micro Raman spectroscopy (Renishaw Invia system) operating at 514.5 nm was used to study the film microstructure, where the laser output power used was 1mW. Low temperature resistance measurements were done in National Physical Laboratory (NPL). Four corner ohmic contacts Ti/Au (10nm/200nm) on the top side of both heterostructures which are made using interconnections with the low temperature measurement PCB by wire bonding. The samples were put in a pulse tube cooler which allowed cooling from room temperature to 2K and done van der Pauw sheet resistance measurements were made with four different connection configurations (the current flowing between four different contacts 1&2 or 2&3 or 3&4 or 4&1). A chopped D.C. measurement method was applied which is to measure the D.C. voltage under a D.C. current, then switch off the current and remeasure the voltage. Then by subtracting the second voltage from the first effective resistance, compensated for any thermoelectric voltage in the leads, can be calculated. UV-visible absorption spectra for transparent SCD and G@SCD were collected with a Shimadzu UV 1800 spectrophotometer. Firstly, H-terminated SCD100/111 was measured, then after graphene transferred heterostructures were measured again.

The density functional simulations are carried out using Vienna *ab-initio* Package (VASP)<sup>6,7</sup>. The electron-core interaction is treated using projected augmented wave (PAW)

potentials<sup>8,9</sup>. The exchange and correlation is used PBE functional, which is proven good for diamond and graphene simulation<sup>10</sup>. Because the van der Waals interaction play the essential role in the hybrid structures, this interaction is treated using optB88-vdW<sup>11</sup>. Kohn-Sham orbitals are expanded in a plane wave basis set with a cut-off energy of 500eV. The systems are relaxed until all forces are less than 0.01eV/Å. A Monkhorst-Pack mesh of 7×7×1 was used for the heterostructures. The dipole correction is also considered. The lattice mismatch is under 2%. The electronic properties would not be affected under this strain in our tests.

### 7.3 Results and Discussion

The surface roughness  $R_a$  of SCD100 and SCD111 (single crystal diamond with different orientations) were identified by atomic force microscopy (AFM) and have small difference of 0.48nm and 0.72nm, respectively. The uniformity of the SCD film is important as the electronic properties of graphene can be modified by surface morphology of supporting materials<sup>12</sup>.

Raman spectroscopy was used to characterise the G@SCD heterostructure as Raman spectra provides common features for all carbon materials<sup>13–15</sup>. It enables to identificate

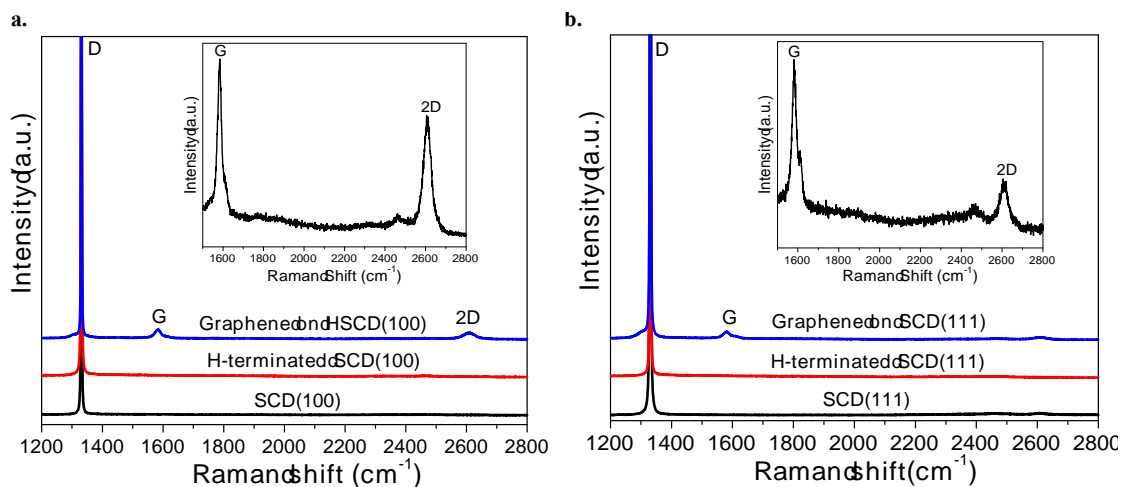


**Figure 7.1 Raman spectra of G@SCD. (a) comparison of SCD(100), H-terminated SCD(100) and G@SCD100. The inset is the smaller range for G@SCD100. (b) comparison of SCD(111), H-terminated SCD(111) and G@SCD111. The inset is the smaller range for G@SCD111.**

functional groups, structure defect and chemical modifications introduced during the preparation and processing of graphene<sup>16</sup>. Electronic properties of graphene due to defects doping or edges effect, will reflect in the widths and intensities of the Raman peaks<sup>13,14</sup>. Fig 7.1 shows the Raman spectra for SCD, H-terminated SCD and G@SCD. The measurements are performed as room temperature with a Renishaw spectrometer at 514 nm with <1mW incident power to avoid monolayer graphene damage. Visible Raman excitation always resonated with the  $\pi$  states and the Raman spectra are dominated by  $sp^2$  sites<sup>14</sup>. The three main intense features are the D peak at  $\sim 1332\text{ cm}^{-1}$ , the G peak at  $\sim 1580\text{ cm}^{-1}$ , and the 2D peak at  $\sim 2608\text{ cm}^{-1}$ , as labelled in Fig 7.1. The D peak is due to the breathing modes of  $sp^2$  atoms in rings, while the G peak is from the bond stretching modes of all pairs of  $sp^2$  atoms in both rings and chains<sup>17</sup>. The 2D peak is second order of D peak whose shape distinguishes single and multilayer graphene<sup>16</sup>. The G and 2D peaks provide information about the level of doping and layer number, and the D peak is activated by lattice defects and the formation of  $sp^3$  hybridization<sup>13,14,16</sup>. The D peak for G@ SCD samples is the first-order Raman line for SCD, which corresponds to the vibrations of the two interpenetrating cubic sublattices<sup>18</sup>. Moreover, a D peak assigned from the disorder of graphene surface is unable to be observed owing to the dominant of the D peak contribution from SCD<sup>14</sup>. In the insets of Fig 7.1, the G peaks' positions for G@SCD heterosturcture have upshifts from  $1580\text{ cm}^{-1}$  of G@SiO<sub>2</sub> to  $1583.76\text{ cm}^{-1}$  and  $1583.23\text{ cm}^{-1}$  for G@SCD100 and G@SCD111 respectively<sup>13</sup>. These G peak shifts result in the shift of Fermi level and induce the doping for graphene<sup>19</sup>. The G peak full width at half maximum [FWHM(G)] for G@SCD100 and G@SCD111 are large,  $51\text{ cm}^{-1}$  and  $40\text{ cm}^{-1}$  respectively, indicating structural disorders<sup>13</sup>. Compared to monolayer

G@SiO<sub>2</sub> where the 2D peak is located at 2700 cm<sup>-1</sup>, the 2D peak positions have big downshift for G@SCD100 (2608 cm<sup>-1</sup>) and G@SCD111 (2609 cm<sup>-1</sup>), owing to hole doping<sup>20,21</sup>. The impurity charges and electron transfer induce an increase of scattering while a decrease of the ratio of I<sub>2D</sub>/I<sub>G</sub><sup>13</sup>. The ratios of I<sub>2D</sub>/I<sub>G</sub> for both heterostructures are 0.2 and 0.7 for G@SCD100 and G@SCD111 respectively, proving electron and hole separation between the interface and highly doping. For low doping, the 2D peak is expected to 3-5 times stronger than the G peak<sup>14</sup>.

XPS was applied to estimate the fraction of sp<sup>2</sup> and sp<sup>3</sup> atoms present<sup>22</sup>. Fig 7.2 shows the C 1s spectral region for SCD100/111, HSCD100/111, G@SCD100 and G@SCD111. The C 1s core-level spectra of samples were fitted by CasaXPS software with the following reference peaks: 284.3-284.6eV binding energy (BE)

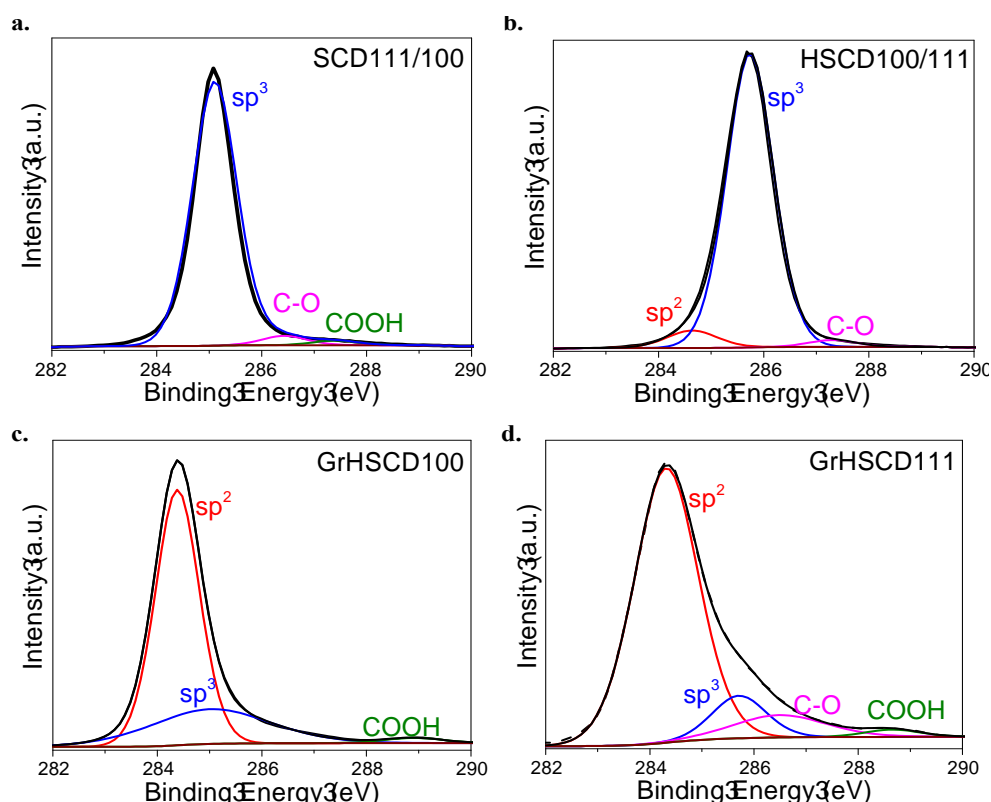


**Figure 7.2 High resolution C1s XPS spectra of SCD and G@SCD. (a) SCD100/111. (b) HSCD100/111. (c) G@SCD100. (d) G@SCD111.**

assigned to  $sp^2$  hybridized C atoms in graphene and C-H bonds due to hydrogen termination; 285-285.5eV BE assigned to  $sp^3$  hybridized C atoms from SCD; C-O with higher BE about 286.4-287eV, and COOH with BE around 288.6eV from interface states, ambient oxygen and moisture<sup>22-25</sup>. The XPS spectrums of SCD100/111 are same, shown in Fig 7.2a, which indicates an oxygenated surface with C-O and COOH groups due to air oxidation. After H-termination, one  $sp^2$  peak appears due to C-H bonds and C-C dimers on the surface. Compared with Fig 7.2(a), the COOH group is removed and replaced by H-termination<sup>26</sup>. After transferring graphene, the reduction of the  $sp^3$  phase for both heterostructures attributes to the interaction  $\pi/\pi^*$  between C-H from diamond surface and graphene which induce the disorder. Similar with hydrogenating graphene, the hydrogen coverage enables to be determined as  $\theta/(1+\theta)$  where  $\theta$  is defined as the intensity area of  $sp^3$  and  $sp^2$  peaks<sup>27</sup>. For G@SCD100, the H coverage is found to be ~27%, while for G@SCD111 the coverage is 12%, which indicates hydrogen bond would play more remarkable effect by C-H bond from SCD100 surface.

In simulation, for SCD (111),  $1 \times 1$  unit cell is used for matching graphene and for SCD(100),  $\begin{pmatrix} 7 & 1 \\ 4 & 1 \end{pmatrix}$  supercell is employed for matching  $\begin{pmatrix} 6 & 1 \\ 4 & 1 \end{pmatrix}$  graphene, shown in Fig 7.3. The binding energy ( $E_b$ ) per atom of graphene with the substrate is defined as following:

$$E_b = \frac{1}{N_G} [E_{Gr@D} - (E_{Gr} + E_D)] \quad (7.1)$$

Where  $E_{Gr@D}$  is the graphene on diamond heterostructure,  $E_{Gr}$  and  $E_D$  is the energy of isolated graphene and diamond substrate, respectively. And  $N_G$  is the number of atoms in the supercell.

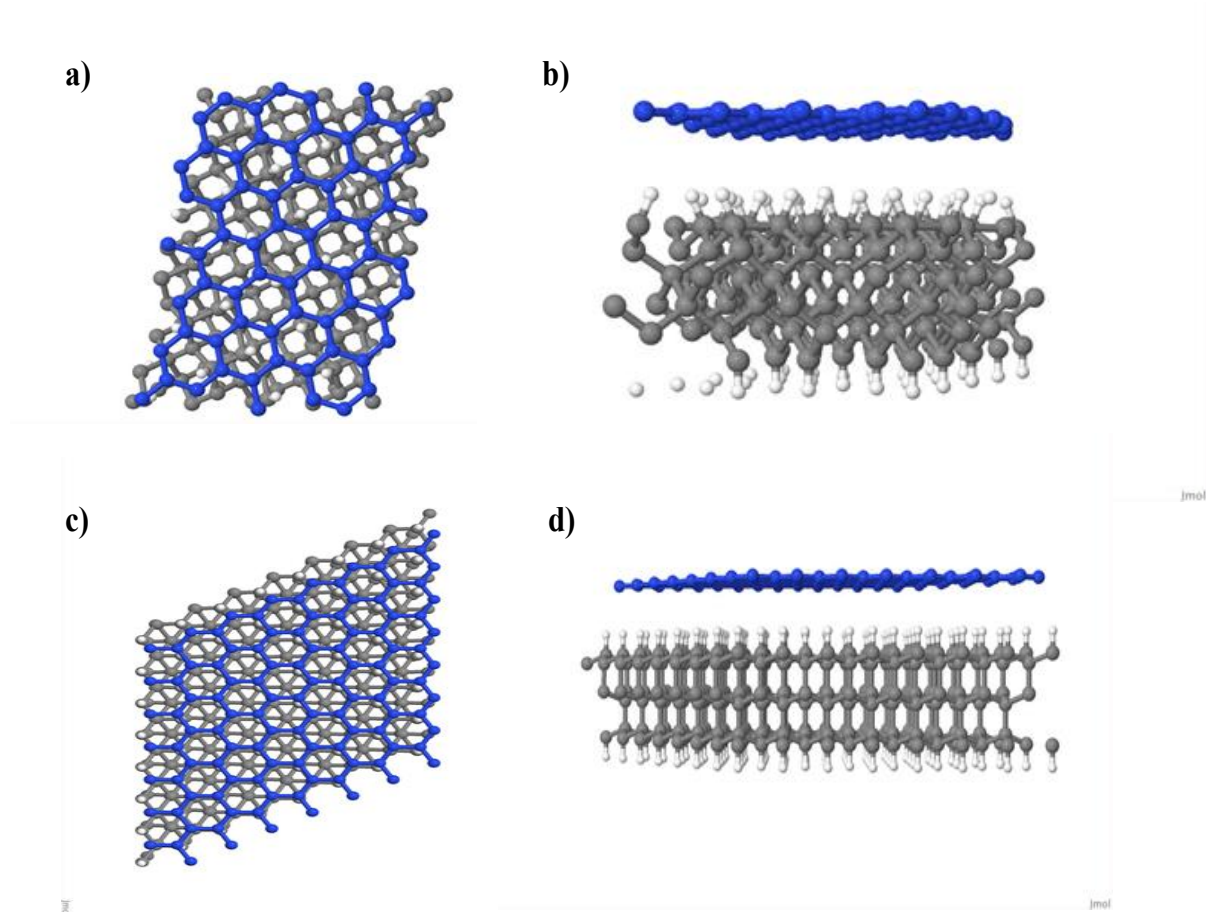


**Figure 7.3** The supercell of the heterostructure. Topview and sideview of Gr@HSCD(100) are on top-left and top-right, respectively. And those of Gr@HSCD(111) are on the bottom-left and bottom-right, respectively.

**Table 7.1** The binding energy per graphene atoms  $E_b$  (meV) and the distance between the graphene and substrates (Å) at equilibrium states

Samples	$E_b$ (meV)	distance (Å)
Gr@HSCD(100)	-57	2.68
Gr@HSCD(111)	-35	2.77
Gr@SCD(100)	-56	3.83
Gr@SCD(111)	-20	3.13

Compared with HSCD(111) substrate, the interaction of graphene with HSCD(100) substrate is stronger with -57 meV/atom. This conclusion is also in line with the distance between the graphene and substrates, where the distance between the graphene and HSCD(100).

Furthermore, the influence of the hydrogen termination have also been investigated. For SCD(111) surface, where the top layer C atoms are non-terminated, is highly reactive, whereas the SCD(100) surface undergoes a surface reconstruction and reformed to SCD(100)-2×1 reconstructed surface. The results are also tested in PBE only functional, which all the binding energies and distances are predicted to be lower and longer. More detailed results in experimental section.

The detailed electronic properties are also investigated by charge density difference and band structure. The charge density difference is defined as

$$\rho = \rho_{Gr@D} - (\rho_{Gr} + \rho_D) \quad (7.2)$$

where  $\rho_{Gr@D}$ ,  $\rho_{Gr} + \rho_D$  are the charge density of after and before graphene put on diamond.

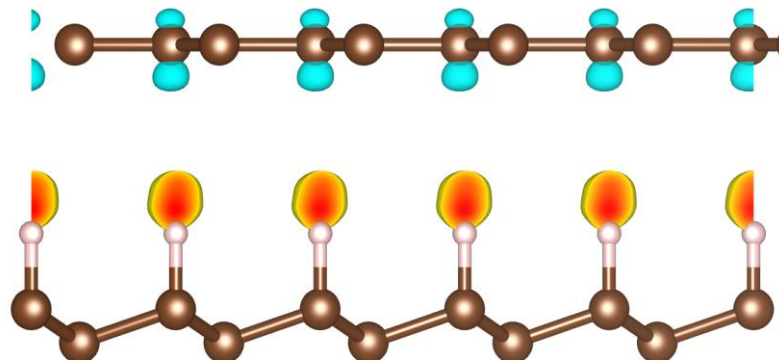


**Figure 7.4** The charge density difference between graphene and SCD(111), blue part means the decrease of density, red part means the increase of density.

From Fig 7.4, the  $p_z$  orbital, which is mainly constituted the  $\pi$  bond above the graphene, decreased, while the hydrogen bonds from the terminated surfaces gain the electron from the graphene. This charge transfer tuned the band structure at K point, shown in Fig 7.5. The band-gaps of the Gr@HSCD(100) and the Gr@HSCD(111) are 35 meV and 20 meV, respectively.

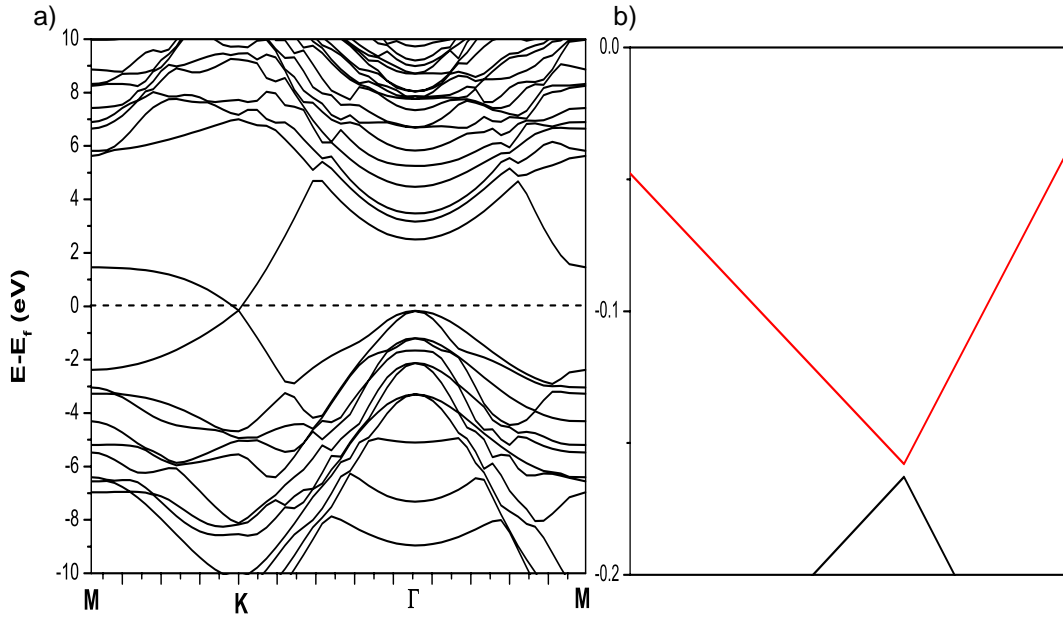


**Figure 7.5 a) Band structure for G@HSCD heterostructure. b) The band gap is opened at K point.**

From theory study, hydrogen terminated SCD tuned a band gap  $E_g$  in the initially zero band gap material. Low temperature sheet resistance measurement was applied in a pulse tube cooler allowing cooling from room temperature to 2K by chopped D.C. resistance technique<sup>28,29</sup>. It shows the resistance increase with decreasing temperature  $dp/dT < 0$ , which prove a transition for graphene from a semi-metallic behaviour to semiconducting behaviour. An estimate for  $E_g$  can be deduced from the temperature dependence of the conductivity  $\sigma = 1/\rho$ , which for a semiconducting material varies according to the Boltzmann transport model:

$$\sigma = \sigma_0 \cdot \exp\left(-\frac{E_g}{2kT}\right) \quad (7.3)$$

The  $\rho(T)$  results were plotted in Fig 7.5 by  $\ln(1/\rho)$  vs  $1/T$  to demonstrate a straight line with slope of  $-E_g/2k$ <sup>30</sup>. For G@SCD100, the resistance increases steadily with decreasing temperature between 290K to 230K (region 1), and from the 230K to 50K (region 2) a

continuing increase in resistance with falling temperature but with a slower rate than at higher temperatures. From Fig 7.5a, the bandgap for region 1 is 0.466eV, and the bandgap for region 2 is 0.0286eV. However, G@SCD111 obtained a steady increase in resistance with falling temperature. The bandgap for G@SCD111 is 0.0164eV from Fig 7.5b.

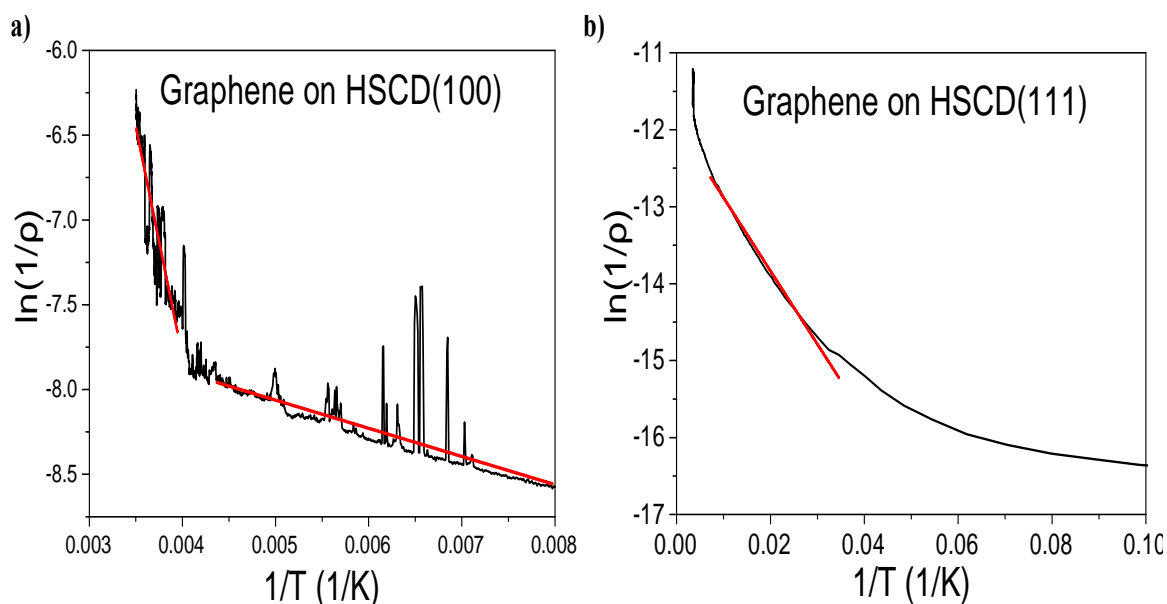


**Figure 7.6** Graphic depiction of  $\ln(1/\rho)$  vs  $1/T$ . (a) G@SCD100. (b) G@SCD111.

UV-visible absorption spectra for HSCD100/111 and G@SCD100/111 were plotted as shown in Fig 7.7. The bandgap estimated from the cut-off wavelength with  $E_g = h \cdot C / \lambda$ , where  $h$  is planks constant,  $C$  is the speed of light<sup>31</sup>. The observed absorption near 210nm for all the samples suggests a  $\pi \rightarrow \pi^*$  transition of C=C<sup>32</sup>. However, a small shoulder for HSCD100 and G@SCD100 gives a second bandgap. The difference bandgaps for HSCD100 and G@SCD100 are 0.026eV for 210nm and 0.17eV for the small shoulder. While for HSCD111 and G@SCD111 only 210nm absorption attends and the difference bandgap of HSCD111 and G@SCD111 is 0.02eV.

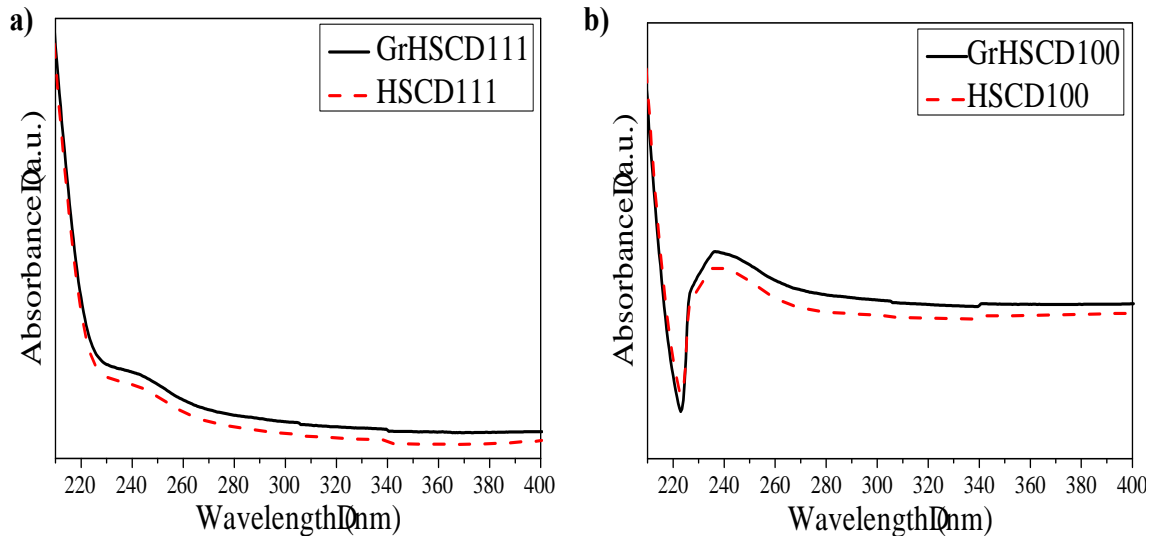


**Figure 7.7 UV-Vis absorption spectra. (a) HSCD111 and Gr@SCD111. (b) HSCD100 and Gr@SCD111.**

#### 7.4 Conclusion

In summary, we have investigated the electronic properties of G@SCD(100)/(111) based on experiments and density functional theory. Hydrogen bonds between diamond and graphene play a remarkable role for the properties of these heterostructure. G and 2D peaks of the heterostructures are shift due to the disorders and doping. From low temperature and UV-vis experimental methods, a small band gap is opened on G@SCD heterostructure, while the band gap for G@HSCD(100) is bigger than its of G@HSCD(111), which is proved by simulation study. In simulation, the band-gaps of the Gr@HSCD(100) and the Gr@HSCD(111) are 35 meV and 20 meV, respectively. The hybrid structures induce a finite gap which is larger than  $k_B T$  for G@SCD(100), indicating the achievable current on/off ratio is larger than that of the freestanding graphene.

## Reference

1. Ma, Y., Dai, Y., Guo, M. & Huang, B. Graphene-diamond interface: Gap opening and electronic spin injection. *Phys. Rev. B* **85**, 235448 (2012).
2. Hollander, M. J. *et al.* Short-channel graphene nanoribbon transistors with enhanced symmetry between p- and n-branches. *Appl. Phys. Express* **7**, 055103 (2014).
3. Zheng, P. *et al.* Hydrogenation of Graphene Nanoribbon Edges : Improvement in Carrier Transport. **34**, 707–709 (2013).
4. Lherbier, A., Botello-Méndez, A. R. & Charlier, J.-C. Electronic and transport properties of unbalanced sublattice N-doping in graphene. *Nano Lett.* **13**, 1446–50 (2013).
5. Kliros, G. S. Analytical modeling of uniaxial strain effects on the performance of double-gate graphene nanoribbon field-effect transistors. *Nanoscale Res. Lett.* **9**, 65 (2014).
6. Physik, T., Wien, T. U. & Hauptstrasse, W. *initio J.* **47**, (1993).
7. Wien, T. U. & Hauptstrage, W. liquid-metal — amorphous-semiconductor. **49**, (1994).
8. augmented+rave. **50**, (1994).
9. Kresse, G. & Joubert, D. From ultrasoft pseudopotentials to the projector augmented-wave method. **59**, 11–19 (1999).
10. Generalized Gradient Approximation Made Simple. **8730**, 46920 (1997).
11. Klimeš, J., Bowler, D. R. & Michaelides, A. Van der Waals density functionals applied to solids. *Phys. Rev. B* **83**, 195131 (2011).
12. Yu, J., Liu, G., Sumant, A. V, Goyal, V. & Balandin, A. a. Graphene-on-diamond devices with increased current-carrying capacity: carbon sp<sup>2</sup>-on-sp<sup>3</sup> technology. *Nano Lett.* **12**, 1603–8 (2012).
13. Casiraghi, C., Pisana, S., Novoselov, K. S., Geim, a. K. & Ferrari, a. C. Raman fingerprint of charged impurities in graphene. *Appl. Phys. Lett.* **91**, 233108 (2007).
14. Ferrari, A. C. Raman spectroscopy of graphene and graphite: Disorder, electron–phonon coupling, doping and nonadiabatic effects. *Solid State Commun.* **143**, 47–57 (2007).
15. Ferrari, A. C. & Robertson, J. Raman spectroscopy of amorphous, nanostructured, diamond-like carbon, and nanodiamond. *Philos. Trans. A. Math. Phys. Eng. Sci.* **362**, 2477–512 (2004).
16. Ferrari, A. C. & Basko, D. M. Raman spectroscopy as a versatile tool for studying the properties of graphene. *Nat. Nanotechnol.* **8**, 235–46 (2013).
17. Casiraghi, C. *et al.* Raman spectroscopy of graphene edges. *Nano Lett.* **9**, 1433–41 (2009).
18. Praver, S. & Nemanich, R. J. Raman spectroscopy of diamond and doped diamond. *Philos. Trans. A. Math. Phys. Eng. Sci.* **362**, 2537–2565 (2004).
19. Pisana, S. *et al.* Breakdown of the adiabatic Born-Oppenheimer approximation in graphene. *Nat. Mater.* **6**, 198–201 (2007).

20. Yan, J., Zhang, Y., Kim, P. & Pinczuk, A. Electric Field Effect Tuning of Electron-Phonon Coupling in Graphene. *Phys. Rev. Lett.* **98**, 166802 (2007).
21. Das, a *et al.* Monitoring dopants by Raman scattering in an electrochemically top-gated graphene transistor. *Nat. Nanotechnol.* **3**, 210–5 (2008).
22. Vander Wal, R. L., Bryg, V. M. & Hays, M. D. XPS analysis of combustion aerosols for chemical composition, surface chemistry, and carbon chemical state. *Anal. Chem.* **83**, 1924–30 (2011).
23. Ech-chamikh, E., Essafti, a., Ijdiyaou, Y. & Azizan, M. XPS study of amorphous carbon nitride (a-C:N) thin films deposited by reactive RF sputtering. *Sol. Energy Mater. Sol. Cells* **90**, 1420–1423 (2006).
24. Xie, F. Y. *et al.* Surface characterization on graphitization of nanodiamond powder annealed in nitrogen ambient. *Surf. Interface Anal.* **42**, 1514–1518 (2010).
25. Zhao, F. *et al.* Electronic properties of graphene-single crystal diamond heterostructures. *J. Appl. Phys.* **114**, 053709 (2013).
26. Cheng, C.-L., Chen, C.-F., Shaio, W.-C., Tsai, D.-S. & Chen, K.-H. The CH stretching features on diamonds of different origins. *Diam. Relat. Mater.* **14**, 1455–1462 (2005).
27. Luo, Z. *et al.* Thickness-dependent reversible hydrogenation of graphene layers. *ACS Nano* **3**, 1781–8 (2009).
28. Hao, L., Gallop, J. C. & Cox, D. Excitation, detection, and passive cooling of a micromechanical cantilever using near-field of a microwave resonator. *Appl. Phys. Lett.* **95**, 113501 (2009).
29. Wang, G., Jia, Q. & Cao, G. A measurement method of high DC voltage. *2012 IEEE Symp. Electr. Electron. Eng.* 19–21 (2012). doi:10.1109/EEESym.2012.6258576
30. Das Sarma, S., Hwang, E. H., Kechedzhi, K. & Tracy, L. a. Signatures of localization in the effective metallic regime of high-mobility Si MOSFETs. *Phys. Rev. B* **90**, 125410 (2014).
31. Zhang, W. *et al.* Facile synthesis of organic-inorganic layered nanojunctions of g-C<sub>3</sub>N<sub>4</sub>/(BiO)<sub>2</sub>CO<sub>3</sub> as efficient visible light photocatalyst. *Dalton Trans.* **43**, 12026–36 (2014).
32. Hsu, H.-C. *et al.* Graphene oxide as a promising photocatalyst for CO<sub>2</sub> to methanol conversion. *Nanoscale* **5**, 262–8 (2013).

# Chapter 8

## Conclusion

Since graphene was first mechanically exfoliated one decade ago<sup>1</sup>, 2D materials have harvested tremendous achievement<sup>2,3</sup>. Not only graphene, transition metal dichalcogenides (TMDs)<sup>4</sup>, hexagonal boron nitride (h-BN)<sup>5</sup> and recently exfoliated phosphorene<sup>3</sup> enrich the 2D family. However, none of them exhibit the distinguished properties as graphene, such as high thermal conductivity, high mechanical strength, high carrier mobility and ability to integrate with most substrates<sup>6</sup>. Supporting material plays a key role for graphene properties. This thesis has investigated electronic properties of graphene on SCD, ND and DLC.

### *Chapter 4*

Single crystal diamond has been used as a substrate to support monolayer CVD graphene. It is possible to chemically functionalise the diamond surface, and in the present case H-, F-, O-, and N-groups have been purposefully added prior to graphene deposition. These have been achieved that the electron properties of the resultant heterostructures vary strongly, and a p-type layer with good mobility and a band gap of 0.07eV is created when H-terminated diamond layers are used, whilst a layer with more metallic-like character (high carrier density and low carrier mobility) arises when N(O)-terminations are introduced. Since it is relatively easy to pattern these functional groups on the diamond surface, this suggests that this approach may offer an exciting route to 2D device structures on single layer graphene sheets.

## *Chapter 5*

Owing to the high-frequency graphene transistors on diamond-like (DLC) carbon application, DLC attracts attention to support graphene compared to SiO<sub>2</sub> substrates. Different terminated DLC has been found to change electronic properties: nitrogen terminations enable to lead to optical band gap shrink; fluorine banding groups have been presented to reduce DLC's surface energy and friction coefficients. CVD monolayer graphene was transferred to DLC, N terminated DLC, and F terminated DLC. AFM, Raman and XPS analysis shows that different support addition groups affect graphene heterostructures' electronic properties. GFDLC sample revealed higher mobility (twice than mobility of GDLC); whilst GNDLC sample gave lower mobility but higher carrier density. This is possible to offer better 2D device applications.

## *Chapter 6*

Here we propose a cost-effective substrate, H-terminated Nanodiamond, for tuning the electronic properties of graphene for the application in Field-Effect Transistor (FET). A systematic analysis and comparisons reveal that H-treatment of the surfaces plays an essential role in tuning the graphene properties. Hall effect measurements show that graphene on H-terminated nanodiamond has improved the mobility by 60% compared with traditional SiO<sub>2</sub> substrate and even has comparable results with single crystal diamond (SCD) at room temperature. Moreover, this prominent mobility can be sustained by increasing the temperature, due to monolayer nanodiamond's higher carrier density and lower sheet resistance, which phenomenon dismisses in SCD. The optimized heterstructure has been designed into Field-Effect Transistor (FET), and its performance is consistent with our analysis. The study provides a new economical and effective way to commercialize carbon-based technology.

## *Chapter 7*

We have investigated the electronic properties of G@SCD(100)/(111) based on experiments and density functional theory. Hydrogen bonds between diamond and graphene play a remarkable role for the properties of these heterostructure. G and 2D peaks of the heterostructures are shift due to the disorders and doping. From low temperature and UV-vis experimental methods, a small band gap is opened on G@SCD heterostructure, while the band gap for G@HSCD(100) is bigger than its of G@HSCD(111), which is proved by simulation study. In simulation, the band-gaps of the Gr@HSCD(100) and the Gr@HSCD(111) are 35 meV and 20 meV, respectively. The hybrid structures induce a finite gap which is larger than  $k_B T$  for G@SCD(100), indicating the achievable current on/off ratio is larger than that of the freestanding graphene.

By supporting graphene on diamond and DLC, we have shown that the mobility of graphene can be improved compared with graphene on the SiO<sub>2</sub>/Si substrate. Different terminated SCD, NDs and DLC substrates are scientifically investigated for the first time. To sum up, NDs is the best supporting substrates for graphene compared with SCD and DLC, which gives the best graphene mobility and offers a low cost sp<sup>2</sup> on sp<sup>3</sup> technology. A novel graphene FET was fabricated on H-terminated monolayer nanodiamond substrates. Future work on this heterstructure project will involve the structure simulation analysis to understand the interaction between hybrid layers for graphene with NDs and DLC. Owing to the induced band gap for graphene on SCD, a graphene switching FET could be fabricated for high frequency digital applications.

## Reference

1. Novoselov, K. S. *et al.* Electric field effect in atomically thin carbon films. *Science* **306**, 666–9 (2004).
2. Liu, Z. *et al.* In-plane heterostructures of graphene and hexagonal boron nitride with controlled domain sizes. *Nat. Nanotechnol.* **8**, 119–24 (2013).
3. Castellanos-Gomez, A. *et al.* Isolation and characterization of few-layer black phosphorus. *2D Mater.* **1**, 025001 (2014).
4. Wang, Q. H., Kalantar-Zadeh, K., Kis, A., Coleman, J. N. & Strano, M. S. Electronics and optoelectronics of two-dimensional transition metal dichalcogenides. *Nat. Nanotechnol.* **7**, 699–712 (2012).
5. Pacilé, D., Meyer, J. C., Girit, C. O. & Zettl, a. The two-dimensional phase of boron nitride: Few-atomic-layer sheets and suspended membranes. *Appl. Phys. Lett.* **92**, 133107 (2008).
6. Balandin, A. a *et al.* Superior thermal conductivity of single-layer graphene. *Nano Lett.* **8**, 902–7 (2008).
7. Kim, K. S. *et al.* Large-scale pattern growth of graphene films for stretchable transparent electrodes. *Nature* **457**, 706–10 (2009).
8. Novoselov, K. S. *et al.* Two-dimensional gas of massless Dirac fermions in graphene. *Nature* **438**, 197–200 (2005).
9. Palacios, T. Graphene electronics: thinking outside the silicon box. *Nat. Nanotechnol.* **6**, 464–5 (2011).

# List of Figures and Tables

<b>Figure 2.1 (a) Diagram of atomic orbitals and <math>sp^3</math>-hybridization. (b) Hybrid orbitals of carbon.</b>	<b>11</b>
<b>Figure 2.2 (a) hexagonal graphite. (b) rhombohedral graphite. (c) diamond elementary cell.</b>	<b>12</b>
<b>Figure 2.3 (a) Graphene structure with <math>\sigma</math>- and <math>\pi</math>- bonds; (b) orbital energy diagram displaying the <math>\sigma</math> and <math>\pi</math> owing to hybridisation.</b>	<b>13</b>
<b>Figure 2.4 Graphene direct lattice showing the lattice and translation vectors.</b>	<b>15</b>
<b>Figure 2.5 First Brillouin zone of graphene in reciprocal space.</b>	<b>16</b>
<b>Figure 2.6 (a) Energy dispersion for graphene band structure; (b) bandstructure along the points of interest in the First Brillouin zone.</b>	<b>17</b>
<b>Figure 2.7 Graphene linear energy dispersion at Dirac point.</b>	<b>18</b>
<b>Figure 2.8 (a) cubic diamond. (b) hexagonal diamond.</b>	<b>21</b>
<b>Table 2.1 Classification of natural diamond types.</b>	<b>22</b>
<b>Figure 2.9 A modern MWPCVD reactor.</b>	<b>23</b>
<b>Figure 2.10 Ternary phase diagram of C:H system.</b>	<b>27</b>
<b>Figure 3.1 (a) H-terminated nanodiamond 10<math>\mu</math>m AFM scan image. (b) O-terminated nanodiamond 10<math>\mu</math>m AFM scan image. (c) 3D AFM scan image H-terminated nanodiamond shows the thickness which proves nanodiamond is monolayer.</b>	<b>39</b>
<b>Figure 3.2: Elastic Rayleigh and inelastic Raman scattering.</b>	<b>40</b>
<b>Figure 3.3 (a) Raman spectra (514 nm) for bulk graphite and single layer graphene, (b) Evolution of graphene Raman spectra, 514 nm (left) and 633 nm (right), with the number of layers.</b>	<b>42</b>
<b>Figure 3.3: XPS basic phenomenon.</b>	<b>43</b>
<b>Figure 3.5 Basic dielectric circuit model with semicircle Cole-Cole plot.</b>	<b>45</b>
<b>Figure 3.6 Basic set up to measure carrier concentration using the Hall effect.</b>	<b>46</b>
<b>Figure 3.7 Van der Pauw resistivity measurements.</b>	<b>47</b>
<b>Figure 3.7 Van der Pauw resistivity measurements.</b>	<b>48</b>

<b>Figure 3.9</b> Reactive-ion etcher scheme.	<b>49</b>
<b>Table 3.1</b> DLC deposition recipe.	<b>49</b>
<b>Figure 3.10</b> Focused ion beam Microscopy.	<b>50</b>
<b>Figure 3.11</b> Seki technotron PECVD setup.	<b>52</b>
<b>Figure 3.12</b> High temperature nanodiamond hydrogen termination setup.	<b>53</b>
<b>Figure 3.13</b> Process for transfer of graphene films.	<b>55</b>
<b>Figure 4.1</b> XPS C1s spectra for different substrates (a) Survey scan of different terminated SCD; (b) Graphene on different terminated SCD;(c) Hydrogen terminated SCD; (d) Oxygen terminated SCD; (e) Nitrogen terminated SCD; (f) Fluorine terminated SCD. (black line is fitted curve).	<b>60</b>
<b>Table 4.1</b> Elemental compositions calculated from XPS spectra for the single crystal (100) diamond substrates, following exposure to different surface termination treatments.	<b>61</b>
<b>Table 4.2</b> Contact wetting angles for each of the sample types.	<b>62</b>
<b>Figure 4.2</b> (a)Raman spectra of graphene on diamond (100) subjected to the various treatments; inset (a) Raman spectra of graphene on diamond (100) subjected to the various treatments, revealing the G peak region; (c) Raman spectrum of similar graphene on SiO <sub>2</sub> -Si.	<b>63</b>
<b>Figure 4.3</b> (a) Mobility values for each sample type plotted against the corresponding sheet carrier concentration; (b) Mobility of H-terminated SCD for large temperature range from 35K to 500K.	<b>64</b>
<b>Table 4.3</b> Sheet resistivity, sheet carrier concentration and carrier mobility for the p-type conduction measured at 298K for each sample type, as judged by Hall effect measurements.	<b>65</b>
<b>Figure 5.1.</b> AFM images of different termination DLC film. Ra is the average surface roughness in nm. (a) DLC. (b) NDLC. (c) FDLC.	<b>71</b>
<b>Figure 5.2</b> Raman Spectrum of DLC films and graphene-DLC heterostructure films. (a) DLC. (b) NDLC. (c) FDLC. (d) graphene on different terminated DLC.	<b>73</b>
<b>Figure 5.3</b> XPS spectrum of DLC films and graphene-different termination DLC heterostructures' films. Blue line for sp <sup>2</sup> and red line for sp <sup>3</sup> . (a) DLC. (b) NDLC. (c) FDLC. (d) graphene on DLC. (e) graphene on NDLC. (f) graphene on FDLC.	<b>75</b>
<b>Table 5.1</b> Hall Effect results for different graphene-DLC heterostructure.	<b>76</b>
<b>Figure 6.1</b> (a) Schematic view of a graphene-HND heterostructure, Nanodiamond with hydrogen termination. (b) AFM images of top-view and 3D-view of hydrogen terminated ND surface. (c) Comparson of FTIR spectra of untreated ND and hydrogen-terminated ND	

surfaces. (d) Raman spectra of untreated ND, H-ND, graphene-ND, and graphene-HND.	85
Table 6.1. Intensities for different peaks.	87
Figure 6. 2 High resolution C1s XPS spectra of ND (a), H-terminated ND (b), graphene on ND (c), and graphene on H-terminated ND (d). $sp^2$ peak red line, $sp^3$ peak blue line, C-O peak pink line, C=O peak green peak, COOH peak cyan line.	87
Table 6.2.Intensity area for $sp^2$ and $sp^3$ peaks.	89
Figure 6.3 (a) Impedance spectra of Gr-HND heterostructure (red line). The inset is the equivalent circuit model and the fitting line in black. (b) Comparison of room temperature Impedance spectra before and after annealing.	90
Figure 6.4 Impedance spectra of graphene on H-terminated ND heterostructure for different temperature. (a) room temperature to 125C; (b) 150C to 250C; (c) 250C to 400C; (d) room temperature results before and after annealing.	91
Figure 6.5 (a) Hall mobility for GrHND and GrHSCD. The inset is Van der Pauw method for measurement. (b) Comparison of sheet resistance and carrier density of GrHND and GrHSCD. (c) Schematic picture of the hydrogenated ND surface in contact with a water layer as it forms in air. (d) Schematic for GrHND heterostructure.	93
Table 6.3. Hall effect measurement results for different samples.	94
Figure 6.6 Fabrication and output characteristics for graphene FET on H-termianted ND. (a) Schematic view of a top-gate FET; (b) SEM image of a top-gatedevices, Scale bar, 10 $\mu$ m.( c) FIB image of the 500 nm device. Scale bar, 2 $\mu$ m. d) and e) Output characteristics of a 500nm device (d) and a 200 nm device (e). Insets, transfer characteristics at drain-souce voltage $V_{ds}=-1V$ .	96
Figure 7.1 Raman spectra of G@SCD. (a) comparison of SCD(100), H-terminated SCD(100) and G@SCD100. The inset is the smaller range for G@SCD100. (b) comparison of SCD(111), H-terminated SCD(111) and G@SCD111. The inset is the smaller range for G@SCD111.	104
Figure 7.2 High resolution C1s XPS spectra of SCD and G@SCD. (a) SCD100/111. (b) HSCD100/111. (c) G@SCD100. (d) G@SCD111.	106
Figure 7.3 The supercell of the heterostructure. Topview and sideview of Gr@HSCD(100) are on top-left and top-right, respectively. And those of Gr@HSCD(111) are on the bottom-left and bottom-right, respectively.	108
Table 7.1 The binding energy per graphene atoms $E_b$ (meV) and the distance between the graphene and substrates (A) at equilibrium states.	108

**Figure 7.4** The charge density difference between graphene and SCD(111), blue part means the decrease of density, red part means the increase of density. **109**

**Figure 7.5** a) Band structure for G@HSCD heterostructure. b) The band gap is opened at K point. **110**

**Figure 7.6** Graphic depiction of  $\ln(1/\rho)$  vs  $1/T$ . (a) G@SCD100. (b) G@SCD111. **111**

**Figure 7.7** UV-Vis absorption spectra. (a) HSCD111 and Gr@SCD111. (b) HSCD100 and Gr@SCD111. **112**

# Appendix: List of Abbreviations

SCD: Single crystal diamond

ND: Nanodiamond

UNCD: Ultrananocrystalline diamond

DLC: Diamond-like carbon

CVD: Chemical Vapour Deposition

FET: Field-effect Transistor

AFM: Atomic force microscopy

RIE: Reactive Ion Etching

FIB: Focused-ion Beam

UV: Ultraviolet

GHND: Graphene on hydrogen terminated nanodiamond

GHSCD: Graphene on hydrogen terminated singly crystal diamond

GND: Graphene on nanodiamond

GSCD: Graphene on single crystal diamond